



**Max-Planck-Institut für Metallforschung**  
Stuttgart

---

# **Mechanical Properties of Small-Scale BCC Metal Structures**

Andreas Simon Schneider

Dissertation  
an der  
**Universität Stuttgart**

---

Bericht Nr. 224  
Februar 2010



# **Mechanical Properties of Small-Scale BCC Metal Structures**

Von der Fakultät Chemie der Universität Stuttgart  
zur Erlangung der Würde eines Doktors der  
Naturwissenschaften (Dr. rer. nat.) genehmigte Abhandlung

Vorgelegt von  
**Dipl. Ing. Andreas Simon Schneider**  
aus Tübingen

Hauptberichter:	Prof. Dr. E. Arzt
Mitberichter:	Prof. Dr. J. Bill
Tag der mündlichen Prüfung:	01.02.2010

INSTITUT FÜR MATERIALWISSENSCHAFT  
DER UNIVERSITÄT STUTTGART  
und  
MAX-PLANCK-INSTITUT FÜR METALLFORSCHUNG STUTTGART

Stuttgart, August 2009



*Meinen Eltern*



Andreas Simon Schneider

## Mechanical Properties of Small-Scale BCC Metal Structures

Institut für Materialwissenschaft, Universität Stuttgart und  
Max-Planck-Institut für Metallforschung Stuttgart, 2009

**Kurzzusammenfassung:** Metalle zeigen im Bereich von einigen Mikrometern und darunter einen extremen Anstieg der Fließspannung mit abnehmender Probengröße, was auch als „Größeneffekt“ bezeichnet wird. Das Verständnis und die Quantifizierung des mechanischen Verhaltens ist ein essentieller Bestandteil für die Entwicklung von mikro- und nanoskaligen Systemen mit herausragenden Eigenschaften. Dies ist nur mit hochentwickelten Testmethoden möglich. Ein Beispiel dafür sind Mikrodruckversuche an metallischen Mikro- und Nanosäulen, die mit einem fokussierten Ionenstrahl (Focused Ion Beam (FIB)) hergestellt werden können. Obwohl die fundamentalen Mechanismen, die den Größeneffekt bestimmen, noch nicht vollständig aufgeklärt sind, wurde für die meisten Metalle ein übereinstimmendes Skalierungsverhalten der Fließspannung ( $\sigma_y$ ) mit dem Säulendurchmesser ( $d$ ) von  $\sigma_y \propto d^{-0.6}$  beobachtet. Die meisten Studien wurden bisher an kubisch-flächenzentrierten (kfz) Metallen durchgeführt, wenngleich die Untersuchung anderer Kristallstrukturen neue Einblicke in die Versetzungsprozesse nanoskaliger Metallstrukturen liefern kann. Die vorliegende Arbeit beschäftigt sich mit der mechanischen Charakterisierung kubisch-raumzentrierter (krz) Metalle mittels Mikrodruckversuchen. [001] und [235] orientierte Wolfram (W), Molybdän (Mo) und Niob (Nb) Proben wurden mittels Funkenerosion aus hochreinen Einkristallen hergestellt. Nach einer sorgfältigen mechanischen und elektrochemischen Politur wurden mit dem FIB Säulen auf den entsprechenden Oberflächen herausgearbeitet. Säulen mit Durchmessern im Bereich von 200 nm bis 6  $\mu$ m wurden getestet, um den Einfluss des Säulendurchmessers auf die Festigkeit krz Metalle zu untersuchen. Dabei wurde beobachtet, dass der Größeneffekt bei krz Metallen mit  $\sigma_y \propto d^{-0.16} - d^{-0.45}$  schwächer ausgeprägt ist als bei kfz Metallen. Weiterhin wurde festgestellt, dass die Festigkeit und die Größenabhängigkeit krz Metalle stark vom Verhältnis der Testtemperatur und der kritischen Temperatur des Metalls ( $T_{\text{test}}/T_c$ ) abhängig sind. Bei krz Metallen mit einer hohen kritischen Temperatur wurden große Festigkeiten und eine geringe Größenabhängigkeit beobachtet, während die Metalle mit einer niedrigen kritischen Temperatur niedrige Festigkeiten und eine ausgeprägte Größenabhängigkeit zeigten. Da  $T_{\text{test}}/T_c$  ein Maß für die Mobilität der Schraubenversetzungen ist, wird angenommen, dass die Größenabhängigkeit krz Säulen durch die temperaturabhängige Mobilität der Schraubenversetzungen bestimmt wird. Die thermisch aktivierte Bewegung von Schraubenversetzungen im Mikro- und Nanometerbereich wurde durch weitere Tests untersucht, bei denen die Belastungsrate über einen großen Bereich geändert wurde. Die Dehnratenabhängigkeit der Säulen war ähnlich wie für die entsprechenden Massivmaterialien und die berechneten Aktivierungsvolumen lagen im Bereich von  $2b^3 - 10b^3$ . Dies entspricht in etwa den erwarteten Werten für eine thermisch aktivierte Bildung von Kinkpaaren an den Schraubenversetzungen. Zusätzlich wurden Druckversuche an vorverformten Mo Säulen durchgeführt. Dabei hat sich gezeigt, dass die Vorverformung keinen Einfluss auf die mechanischen Eigenschaften hat, wenn die vorverformten Säulen vor dem Test mit dem FIB nachgeschnitten wurden. Dies suggeriert, dass die Defekte, die durch das FIB in das Material eingebracht werden, als Versetzungsquellen fungieren, welche die mechanischen Eigenschaften der vorverformten Säulen bestimmen.





**Andreas Simon Schneider**

## **Mechanical Properties of Small-Scale BCC Metal Structures**

Institute for Materials Science, University of Stuttgart and  
Max Planck Institute for Metals Research, Stuttgart, 2009

**Abstract:** Metals with a critical dimension in the micro- and nanometer regime have demonstrated a dramatic increase in strength with decreasing sample size termed the ‘size effect’. Understanding and quantifying mechanical behavior is an essential part of creating small-scale systems with advanced properties, and is possible using highly developed experimental testing techniques such as compression of small-scale metal pillars formed using focused ion beam (FIB) machining. Although the fundamental mechanisms which govern the size effect are not totally clear, a consistent scaling relationship for the flow stress ( $\sigma_y$ ) with pillar diameter ( $d$ ) on the order of  $\sigma_y \propto d^{-0.6}$  has been found for several metals. The majority of these studies have focused on metals with face-centered cubic (fcc) crystal structure, however, it is expected that studying nanoscale metals with different crystal structures could give insight into the dislocation processes involved in nanoplasticity. The work presented in this dissertation deals with the mechanical characterization of body-centered cubic (bcc) nanostructures by means of small-scale compression tests. Tungsten (W), molybdenum (Mo) and niobium (Nb) [001] and [235] oriented samples were obtained by electron discharge machining from high purity single crystals. After careful mechanical and electro-polishing, compression pillars were machined with a FIB on the surfaces. Pillars with diameters ranging from 200 nm to 6  $\mu$ m were tested in compression to study the influence of pillar diameter on the strength of bcc metals. In general, it was found that with a relationship of  $\sigma_y \propto d^{-0.16} - d^{-0.45}$  bcc metals have a weaker size dependence than fcc metals. Further, the strength and the size scaling of bcc metals were observed to be strongly related to their respective critical temperature to test temperature ratio ( $T_{\text{test}}/T_c$ ). For bcc metals with a high critical temperature high strengths and weak size dependence were measured, whereas those with a low critical temperature showed low strengths and strong size dependence. Because  $T_{\text{test}}/T_c$  is a measure for the mobility of screw dislocations in bcc metals, it was concluded that the size dependent deformation of bcc pillars is likely explained by considering the temperature dependent mobility of screw dislocations. The thermally activated motion of screw dislocations at micron- and submicron scale was further investigated by testing over a wide range of loading rates. The strain rate sensitivities were close to bulk values and the calculated activation volumes were in the range of  $2b^3$  to  $9b^3$  corresponding to expected values for thermally activated kink-pair nucleation on screw dislocations. Additionally, compression tests were performed on pre-strained Mo pillars. It was shown that the pre-straining has no influence on the mechanical properties if the pre-strained pillars are re-shaped with the FIB prior to testing. This suggests that the defects introduced into the material by the FIB serve as dislocation sources, which control the mechanical behavior of the pre-strained pillars.



## **Danksagung**

Diese Doktorarbeit wurde in der Zeit von Juni 2006 bis August 2009 am Max-Planck-Institut für Metallforschung in Stuttgart und am Institut für Materialwissenschaft der Universität Stuttgart angefertigt.

Mein besonderer Dank gilt Herrn Prof. Dr. Eduard Arzt für die freundliche Aufnahme an seinem Institut und für die Möglichkeit an einer so interessanten Themenstellung zu arbeiten. Seine ständige Unterstützung durch wertvolle Anregungen und Diskussionen, sowie die ausgezeichnete „Fernbetreuung“ zwischen Saarbrücken und Stuttgart haben maßgeblich zum Gelingen der Arbeit beigetragen.

Herrn Prof. Dr. J. Bill danke ich für die Übernahme des Mitberichts.

Meinen beiden Betreuern, Dr. C. Frick und Dr. P. Gruber danke ich für ihr Engagement bei der Betreuung der Arbeit, sowie für ihre stetige Bereitschaft zu Diskussionen und ihre Mühe bei der Korrektur der Arbeit.

Bei Frau Dr. B. G. Clark und Dr. G. Richter bedanke ich mich herzlich für die fachliche und freundschaftliche Unterstützung. Die Zusammenarbeit mit ihnen gab dieser Arbeit viele gute Impulse.

Für die Bereitstellung der Tantal-Daten und für die erfolgreiche Zusammenarbeit bedanke ich mich ganz herzlich bei D. Kaufmann, Dr. R. Mönig und Prof. Dr. O. Kraft vom Institut für Materialforschung II des Forschungszentrums Karlsruhe.

Mein Dank gilt auch Dr. T. Wübben für die anfängliche Betreuung, vor seinem Weggang nach Österreich.

Frau U. Eigenthaler danke ich für ihre Einführung in den Umgang mit dem Rasterionenmikroskop, Herrn A. Weible für seine außerordentlich Mühe bei der Herstellung der Einkristalle.

Dr. D. Brunner und Dr. W. Wasserbäch danke ich für viele hilfreiche Diskussionen über kubisch-raumzentrierte Metalle.

Frau S. Kurz und Herr C. Schwenk haben mich stets mit großer Sorgfalt bei meinen experimentellen Arbeiten unterstützt, dafür danke ich ihnen herzlich.

Meinen Kommilitonen Florian Rödl, Wolfgang Baumann und Alexander Kabakchiev möchte ich für die freundschaftliche Unterstützung während der ganzen Zeit danken.

## Danksagung

---

Mein Dank gilt weiterhin denen, die mich bei alltäglichen Problemen in vielfältiger Weise unterstützt haben: Reinhart Völker, Birgit Heiland, Ilse Lakemeyer sowie Frank Thiele.

Auch allen nicht namentlich genannten Mitarbeitern des Instituts sage ich zum Abschied ein Dankeschön für das freundschaftliche Arbeitsklima in den vergangenen drei Jahren.

Zum Schluss möchte ich mich bei meinen Eltern für ihre Unterstützung während dieser Arbeit bedanken, sie waren immer mit Rat und Tat für mich da.

<b>KURZZUSAMMENFASSUNG .....</b>	<b>III</b>
<b>ABSTRACT.....</b>	<b>V</b>
<b>DANKSAGUNG .....</b>	<b>VII</b>
<b>INDEX.....</b>	<b>IX</b>
<b>1 INTRODUCTION .....</b>	<b>- 1 -</b>
<b>2 FUNDAMENTALS AND LITERATURE REVIEW .....</b>	<b>- 5 -</b>
2.1 MECHANICAL PROPERTIES OF METALS .....	- 5 -
2.1.1 <i>The Critical Resolved Shear Stress</i> .....	- 5 -
2.1.2 <i>Temperature Dependent Flow Stress of BCC Metals</i> .....	- 9 -
2.1.3 <i>Strain Hardening Behavior of Single Crystals</i> .....	- 13 -
2.2 LITERATURE REVIEW .....	- 15 -
2.2.1 <i>Mechanical Properties of Small-Scale Metal Structures</i> .....	- 15 -
2.2.2 <i>Microcompression Tests on BCC Metals</i> .....	- 21 -
2.2.3 <i>Summary and Motivation</i> .....	- 25 -
<b>3 EXPERIMENTAL.....</b>	<b>- 27 -</b>
3.1 SAMPLE PREPARATION.....	- 27 -
3.2 MICROCOMPRESSION TESTING.....	- 28 -
3.3 EXPERIMENTAL LIMITATIONS .....	- 30 -
<b>4 EFFECT OF ORIENTATION AND LOADING RATE ON COMPRESSION BEHAVIOR OF SMALL-SCALE MO PILLARS.....</b>	<b>- 33 -</b>
4.1 ABSTRACT.....	- 33 -
4.2 INTRODUCTION .....	- 34 -
4.3 EXPERIMENTAL PROCEDURE.....	- 36 -
4.4 RESULTS .....	- 37 -
4.5 DISCUSSION .....	- 42 -
4.6 CONCLUSIONS .....	- 45 -
4.7 ACKNOWLEDGEMENTS.....	- 46 -
<b>5 CORRELATION BETWEEN CRITICAL TEMPERATURE AND STRENGTH OF SMALL-SCALE BCC PILLARS.....</b>	<b>- 47 -</b>
5.1 ABSTRACT.....	- 47 -
5.2 INTRODUCTION .....	- 48 -
5.3 EXPERIMENTAL PROCEDURE.....	- 49 -
5.4 RESULTS .....	- 49 -
5.5 DISCUSSION .....	- 53 -
5.6 CONCLUSIONS .....	- 55 -
5.7 ACKNOWLEDGEMENTS.....	- 56 -
<b>6 EFFECT OF PRE-STRAINING ON THE SIZE EFFECT IN MOLYBDENUM PILLARS.....</b>	<b>- 57 -</b>
6.1 ABSTRACT.....	- 57 -
6.2 INTRODUCTION .....	- 58 -
6.3 MOTIVATION AND EXPERIMENTAL PROCEDURE .....	- 59 -
6.4 RESULTS .....	- 60 -
6.5 DISCUSSION .....	- 64 -
6.6 CONCLUSIONS .....	- 66 -
<b>7 INFLUENCE OF ORIENTATION ON THE SIZE EFFECT IN BCC PILLARS WITH DIFFERENT CRITICAL TEMPERATURE .....</b>	<b>- 67 -</b>
7.1 ABSTRACT.....	- 67 -
7.2 INTRODUCTION .....	- 68 -
7.3 EXPERIMENTAL PROCEDURE.....	- 70 -
7.4 RESULTS .....	- 70 -
7.5 DISCUSSION .....	- 77 -
7.6 CONCLUSIONS .....	- 81 -

<b>8</b>	<b>CORRELATION BETWEEN ACTIVATION VOLUME AND PILLAR DIAMETER FOR BCC PILLARS.....</b>	<b>- 83 -</b>
8.1	ABSTRACT.....	- 83 -
8.2	INTRODUCTION.....	- 84 -
8.3	EXPERIMENTAL PROCEDURE.....	- 84 -
8.4	RESULTS.....	- 85 -
8.5	DISCUSSION.....	- 87 -
8.6	CONCLUSIONS.....	- 89 -
<b>9</b>	<b>SUMMARY.....</b>	<b>- 91 -</b>
<b>10</b>	<b>ZUSAMMENFASSUNG IN DEUTSCHER SPRACHE.....</b>	<b>- 97 -</b>
10.1	STAND DER FORSCHUNG UND MOTIVATION.....	- 97 -
10.2	SPANNUNGS-DEHNUNGSVERHALTEN VON KRZ MIKRO- UND NANOSÄULEN.....	- 98 -
10.3	VERFORMUNGSMORPHOLOGIE.....	- 99 -
10.4	GRÖßEN- UND TEMPERATURABHÄNGIGKEIT DER FLIEßSPANNUNG.....	- 100 -
10.5	EINFLUSS DER PROBENORIENTIERUNG.....	- 101 -
10.6	DEHNRATENABHÄNGIGKEIT UND AKTIVIERUNGSVOLUMEN.....	- 103 -
10.7	EINFLUSS DER VORVERFORMUNG.....	- 104 -
10.8	ZUSAMMENFASSUNG.....	- 105 -
<b>11</b>	<b>REFERENCES.....</b>	<b>- 107 -</b>

# 1 Introduction

Small-scale metal structures play a crucial role in a broad range of technological applications. They serve as building blocks in microelectronic and microoptical devices where they frequently determine essential device functions. Additionally, they are used as thin coatings to improve wear and corrosion resistance. In recent decades, small-scale metal structures have become relevant components of micro-electro-mechanical systems (MEMS) which combine mechanical sensors, actuators and electronic circuits at the micro scale. Contemporary MEMS have numerous commercial applications such as digital mirror devices for projection displays, integrated accelerometers for airbag deployment, portable electronic devices, and video game controllers.

Despite the commercial success of a variety of micro-scale metal structure applications, the vast potential of the field remains underdeveloped. Furthermore, the ongoing trend of miniaturization is leading to smaller and smaller structures and a serious effort to switch to nano-systems. Future materials may be designed at multiple length scales and built from quantum and nanometer sized components in order to exploit their unique functionality. Although necessary to incorporate these materials into proposed devices and systems, knowledge of the fundamental mechanical properties at this size scale is lacking.

Besides the technological driving force, there is a strong scientific motivation to study the mechanical behavior of small-scale metal structures. It has been recognized that mechanical properties at the micro/nano scale deviate from bulk properties. In particular, the strength of metals has been shown to increase with decreasing sample size, a phenomenon generally referred to as size effect [1]. For example, thin film experiments, including wafer curvature [2, 3], micro tensile tests [4, 5], bulge tests [6, 7] and MEMS based tests [8], have consistently shown an inverse scaling of yield strength and film thickness. This scaling behavior has been rationalized by the constraints on dislocations imposed by interfaces [9, 10] or the fine microstructure [11, 12] present in thin films. Size effects also appear if single crystalline metals are deformed in small and unconstrained volumes. This was demonstrated in numerous nanoindentation studies [13-15], where the tested volume is defined through the indentation depth and the arising stress field beneath the indenter. The measured hardness showed an inverse scaling with the indentation depth which was explained in terms of size dependent strain gradients and the hardening associated with the formation of geometrical necessary dislocations (GND) [16]. Another type of size effect is observed in the earliest stage of nanoindentation where the indentation depth is only a few nanometers. At this size scale the

tested volume is considered to be dislocation free. Consequently, the onset of plastic deformation at stress levels close to the theoretical strength of the tested material can be related to the nucleation of new dislocations [15, 17, 18].

Recently, microcompression tests on focused ion beam (FIB) machined nano- and micropillars have shown that single crystalline metals containing dislocations exhibit size dependent yield stresses even for unconstrained geometries and in the absence of strain gradients [19-28]. For example the study by Frick et al. [26] reported that [111] Ni pillars with diameters of about 200 nm can support stresses of more than 2 GPa, which is much higher than the bulk yield stress of single crystalline Ni but significantly lower than the theoretical limit. Further, for Ni and other face-centered cubic (fcc) metals these studies have demonstrated a universal relationship between yield strength  $\sigma_y$  and pillar diameter  $d$  of  $\sigma_y \propto d^{0.6}$  [29].

Until now, only limited data have been acquired for metals with non-fcc crystal structures. However, studying other crystal structures may give new insights into dislocation processes at the nano-scale. Metals with a body-centered cubic (bcc) crystal structure are of great interest, because their dislocation processes fundamentally differ from those of fcc metals [30-33]. In bcc metals the Peierls barrier of screw dislocations is exceptionally high due to their non-planar core structure. Thus, screw dislocations have to overcome the Peierls barrier by means of thermal activation which leads to a characteristic temperature and strain rate sensitivity of the flow stress of bcc metals.

The aim of this work is to study the mechanical properties of bcc metals at the micron and submicron scale and to extend our understanding of the deformation mechanisms that control the mechanical properties in small dimensions. For this purpose, pillars of tungsten (W), molybdenum (Mo) and niobium (Nb) with diameters ranging from 200 nm to 6  $\mu\text{m}$  were prepared via FIB and tested with the microcompression technique. The stress-strain behavior as well as the deformation morphology were analyzed. Experimental results are compared to existing models, such as starvation and nucleation theory, and to the results of recent fcc & bcc pillar studies. The influences of dislocation interactions and dislocation density are systematically studied by testing pillars of single slip and multiple slip orientations with different amounts of pre-straining. For the first time, the temperature and strain rate dependences of the yield strength of bcc metals are investigated in dimensions within a size range of 200 nm to 6  $\mu\text{m}$ . The temperature and strain rate sensitivity of these small scale bcc metals is proposed to be directly related to thermally activated dislocation processes.



This thesis is outlined as follows: Chapter 2 presents the basics of the mechanical behavior of metals and briefly reviews the current state of research on the mechanical behavior of small-scale metal structures.

Chapter 3 discusses the experimental procedures utilized for sample preparation and the microcompression technique.

In Chapter 4, the mechanical properties of single slip and multiple slip Mo pillars are investigated. The influence of the pillar diameter, pillar orientation, and loading rate on the mechanical properties is evaluated quantitatively. This work has been published by A. S. Schneider, B. G. Clark, C. P. Frick, P. A. Gruber and E. Arzt in *Material Science and Engineering (A)*, Volume 508, Issues 1-2, 20 May 2009, Pages 241-246.

Chapter 5 focuses on the effect of the critical temperature on the deformation morphologies and strengths of [001] oriented W, Mo and Nb pillars. Also shown are data for Ta, which were provided by the group of Prof. Dr. O. Kraft from the Institute for Materials Research II of the Forschungszentrum Karlsruhe. The experimental results are discussed in terms of the temperature dependent screw dislocation mobility and size dependent dislocation processes recently proposed for fcc pillars. Chapter 5 has been published by A. S. Schneider, D. Kaufmann, B. G. Clark, C. P. Frick, P. A. Gruber, R. Mönig, O. Kraft and E. Arzt in *Physical Review Letters*, Volume 103, Issue 10, 31 August 2009, Pages 105501-4.

Chapter 6 presents an experimental technique that allows testing of pillars with different amounts of pre-straining in order to distinguish between dislocation starvation and dislocation accumulation effects. The effect of pre-straining on pillar morphology, size dependence, and strain hardening rate is quantified and compared to recent results on fcc and bcc pillars. Chapter 6 is submitted to *Scripta Materialia* and is co-authored by B. G. Clark, C. P. Frick, P. A. Gruber and E. Arzt

In Chapter 7, we investigate the effect of single slip and multiple slip deformation on pillar morphology, size dependence and strain hardening rate for W, Mo and Nb pillars.

Chapter 8 compares the loading rate dependence and calculated activation volumes for W, Mo and Nb pillars. The effect of pillar diameter on the activation volume is analyzed and related to size dependent properties.



## 2 Fundamentals and Literature Review

### 2.1 Mechanical Properties of Metals

#### 2.1.1 *The Critical Resolved Shear Stress*

The stress required to initiate permanent deformation is an important concept in the discussion of mechanical properties. At low and moderate temperatures, the permanent deformation of crystalline metals is directly related – besides the possibility of twinning - to the presence of dislocations and their response to an applied stress. Two special forms of dislocations can be distinguished [34, 35]. For edge dislocations the Burgers vector is normal to the line of the dislocation whereas for screw dislocations the Burgers vector is parallel to the line vector. A dislocation is of mixed character if the angle between the Burgers vector and line vector is different from  $0^\circ$  or  $90^\circ$ . Motion of dislocations can occur only on those crystallographic planes which contain the Burgers vector  $b$  and the line vector  $l$ . These planes are called glide planes and the direction of the Burgers vector defines the slip direction. The combination of glide plane and related slip direction are designated as slip system. Screw dislocations with  $b$  parallel to  $l$  can change their glide plane, which is referred to as cross-slip.

Generally, the glide planes are the crystallographic planes with the closest packing of atoms, while the glide direction is the crystallographic direction with the highest packing density (e.g. [36], p. 435 ). In each crystal structure, there are a certain number of crystallographically equivalent slip systems. Table 2.1 lists the crystallographic slip systems for fcc and bcc metals. Each slip plane can contain more than one slip direction and thus the number of slip systems is the number of possible combinations of slip directions and slip planes.

**Table 2.1:** Slip systems in fcc and bcc metals

Crystal Structure	Slip Planes	Slip Directions	Number of Slip Systems
fcc	{111}	$\langle 110 \rangle$	$4 \times 3 = 12$
bcc	{110}	$\langle 111 \rangle$	$6 \times 2 = 12$
	{112}	$\langle 111 \rangle$	$12 \times 1 = 12$
	{123}	$\langle 111 \rangle$	$24 \times 1 = 24$

In bcc metals, slip always occurs in the closed-packed direction; however, it may take place on crystallographic different planes. For example, in early studies [37, 38] slip traces indicative for slip on  $\{110\}$ ,  $\{112\}$  and  $\{123\}$  planes were observed. Subsequent studies on ultra pure bcc metals [39, 40] have demonstrated that slip on  $\{123\}$  planes is caused by impurity effects. Further, it was shown that dislocations glide on  $\{110\}$  planes at low temperatures, whereas at higher temperatures slip on  $\{112\}$  planes is activated [41, 42].

If a crystalline material is subjected to a tensile or compressive stress  $\sigma$ , plastic deformation can occur on one or several slip systems. Which of the specific slip systems is activated depends on the resolved shear stress that occurs along each slip system. The resolved shear stress on a specific slip system for a certain sample orientation can be calculated according to Schmid's law [43]. If a sample with a transverse cross-sectional area  $A_0$  is subjected to a tensile force  $F$ , the applied stress is given as  $\sigma = F / A_0$ . As shown in Fig. 2.1, the angle between the normal of the glide plane with respect to the stress direction is  $\chi$ , and  $\lambda$  is the angle between the slip direction and the stress axis. The force resolved in the slip direction is  $F \cdot \cos \lambda$  and the area of the glide plane is given by  $A = A_0 / \cos \chi$ . Consequently, the resolved shear stress which acts on the glide plane in the direction of slip is

$$\tau_{\text{RSS}} = \frac{F \cdot \cos \lambda}{A} = \frac{F}{A_0} \cos \chi \cos \lambda = \sigma \cdot s \quad (2.1)$$

where  $s$  is the Schmid factor.

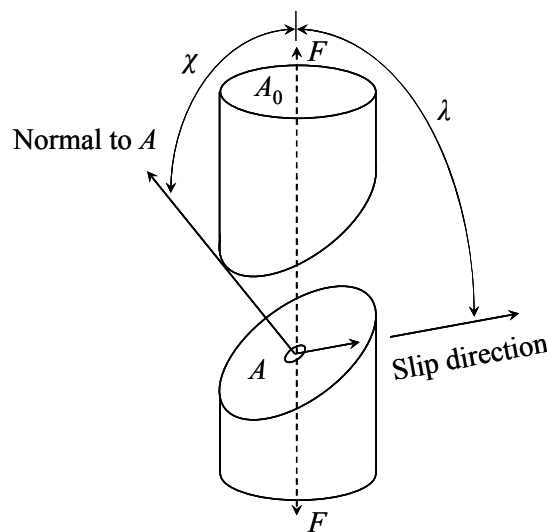


**Figure 2.1:** Geometry used for calculating the resolved shear stress on a slip system in a single crystal for the case of uniaxial loading.

When an applied stress causes this resolved shear stress to reach a critical value, then dislocation motion occurs ( e.g. [44], p.142). This critical resolved shear stress  $\tau_{\text{CRSS}}$  is material dependent and related to microstructural features such as defect concentration and grain size. On the other hand, the value of  $\tau_{\text{CRSS}}$  depends on external test conditions such as temperature and strain rate. Increasing microstructural constraints will increase the value of  $\tau_{\text{CRSS}}$  while both increasing temperature and decreasing strain rate will decrease  $\tau_{\text{CRSS}}$ . The effects of temperature and strain rate on the critical resolved shear stress are illustrated in Fig. 2.2 for a temperature range where diffusion and creep are not relevant.

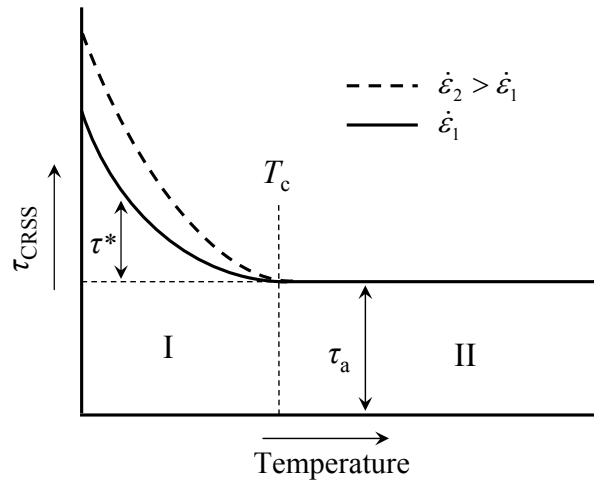


**Figure 2.2:** Schematic temperature and strain rate variation of the critical resolved shear stress (adapted from [44], p. 143). Below a transition temperatures  $T_c$  the  $\tau_{\text{CRSS}}$  increases with decreasing temperature and increasing strain rate (region I). At intermediate temperatures the  $\tau_{\text{CRSS}}$  is independent of temperature and strain rate (region II).

Below a transition temperature  $T_c$ , the  $\tau_{\text{CRSS}}$  consists of a temperature dependent part  $\tau^*$  as well as an athermal (e.g. [45], p. 196) part  $\tau_a$  and can be represented as

$$\tau_{\text{CRSS}} = \tau_a + \tau^* . \quad (2.2)$$

The temperature at which the thermal part becomes zero indicates the transition from region I to region II in Fig. 2.2. In region II, the  $\tau_{\text{CRSS}}$  is almost independent of temperature except for the temperature dependence of the shear modulus. The thermal and athermal part in equation (2.2) are correlated with the interaction of dislocations with short-range and long-range obstacles. If the energy barrier associated with these obstacles is too large for thermal activation, the obstacles are responsible for the athermal part of the  $\tau_{\text{CRSS}}$ . This is the case for long-range obstacles such as the stress-field due to forest dislocations, grain boundaries or other structural defects. On the other hand, short-range barriers can be overcome by sufficient thermal activation and can therefore be related to the thermal part in equation (2.2). Examples

for short-range barriers include the resistance due to point defects such as solute atoms, vacancies and interstitials, other dislocations which intersect the glide plane or the Peierls potential, which is the intrinsic lattice resistance experienced by the dislocations. The latter is a significant contribution to  $\tau_{\text{CRSS}}$  of bcc metals, and will be discussed in detail in the next section. With increasing temperature,  $\tau^*$  becomes smaller, because thermal activation becomes more dominant. Thus, for temperatures above the transition temperature, short range barriers are no longer relevant and  $\tau_{\text{CRSS}}$  is controlled by the athermal contribution  $\tau_a$ .

In regime I, where dislocations overcome potential barriers by thermal activation, the shear rate  $\dot{\gamma}$  can be expressed by an Arrhenius type equation

$$\dot{\gamma} = \dot{\gamma}_0 \exp\left(\frac{-\Delta G}{kT}\right). \quad (2.3)$$

Here,  $T$  is the absolute temperature,  $k$  is Boltzmann's constant, and  $\dot{\gamma}_0$  is a parameter that depends on the vibrational frequency, the density of mobile dislocations, the strain per successful activation and the entropy [46].  $\Delta G$  is the Gibbs free energy of activation, which is strongly dependent on the effective stress  $\tau^*$ . If an external stress assists the dislocations to overcome the obstacles,  $\Delta G$  is given by

$$\Delta G = \Delta F - \nu \tau^* \quad (2.4)$$

where  $\Delta F$  is the free energy to overcome the obstacles without external stress and  $\nu$  is the activation volume. The latter depends on the size and separation of the obstacles and can be expressed as

$$\nu = b \cdot \xi \cdot l \quad (2.5)$$

where  $l$  is the length of the dislocation segment and  $\xi$  is the displacement of the dislocation segment during one activation event ([47], p. 51; [48], p. 219). Consequently, the determination of the activation volume can give characteristic information about the barriers experienced by the dislocations and is therefore a useful parameter for identifying the rate controlling deformation mechanism [49-51]. If the strain rate dependence of the flow stress is measured experimentally, the activation volume can be calculated based on

$$\nu = -m \left( \frac{\partial \Delta G}{\partial \sigma^*} \right) = mkT \left( \frac{\partial \ln \dot{\epsilon}}{\partial \sigma^*} \right). \quad (2.6)$$

Here,  $\dot{\epsilon}$  is the strain rate,  $m$  is the reciprocal Schmid factor for single crystals and the Taylor factor for polycrystals.  $\sigma^*$  is related to  $\tau^*$  through the relationship  $\sigma^* = m\tau^*$ .

### 2.1.2 Temperature Dependent Flow Stress of BCC Metals

Below the critical temperature  $T_c$  (also called the athermal temperature or knee temperature), the flow stress of bcc metals increases with decreasing temperature and is strain rate dependent [30-32, 52, 53]. Experiments on ultrapure bcc metals have demonstrated that these effects are inherent to the bcc crystal structure and are not related to their sensitivity against impurities [54-67]. The special role of the screw dislocations for the temperature and strain rate dependence of the flow stress was revealed by transmission electron microscopy (TEM) [68-74] and computer simulations [75-78]. It was shown that screw dislocations are less mobile than edge dislocations and that they have a non-planar core structure. The particularities of the screw dislocations are directly related to the crystallography of the bcc structure. Screw dislocations lie along the  $\langle 111 \rangle$  crystallographic axis which has a three-fold symmetry [30-32, 52]. As a consequence of an elastic energy reduction the core of screw dislocations spreads over three crystallographic planes of the  $\langle 111 \rangle$  zone axis [79]. The core structure leads to a particular high Peierls potential which the screw dislocations have to overcome by a thermally activated, stress assisted kink-pair formation [30-32, 52]. In this process the dislocation overcomes the Peierls potential only locally by the formation of a kink-pair which connects the dislocation segments in the adjacent Peierls valleys. Under the action of an applied stress, the two kinks move in opposite directions and finally bring the dislocation into the adjacent Peierls valley, as illustrated in Fig. 2.3.

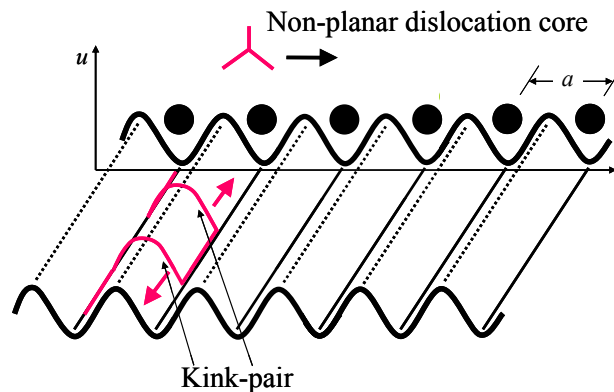


**Figure 2.3:** Schematic of the thermally activated kink-pair mechanism with a Peierls potential  $u$  and a period  $a$ . The screw dislocation surmounts the Peierls potential locally by the formation of a kink-pair. Under the action of an applied stress, the two kinks move in opposite directions and bring the screw dislocation into the adjacent Peierls valley.

The temperature dependent kink-pair formation controls the mobility of the screw dislocations and is therefore responsible for the temperature and strain rate dependent flow stress of bcc metals [41, 42]. Edge dislocations have much higher mobility than screw dislocations at temperatures below  $T_c$ , because of their planar dislocation core leading to a much lower Peierls potential [75]. Above  $T_c$ , the mobilities of edge and screw dislocations are very similar due to thermal activation of screw dislocations and the flow stress approaches the strain rate independent value  $\tau_a$  which is determined by long-range stress fields as discussed in chapter 2.1.1.

In 1981, Seeger [41] extended the kink-pair theory to explain the low-temperature flow stress of bcc metals. Extensive studies on Nb [56, 67], Ta [57], Fe [58-62], Mo [63, 66], and W [64, 65, 80] have shown that there are three distinct regimes below  $T_c$ . In the notation proposed by Brunner and Diehl [81] they are called regimes I to III, as illustrated in Fig. 2.4. The upper bend, indicating the transition between regime I and II occurs at a fixed stress level  $\hat{\sigma}$  that is independent of the strain rate, but the corresponding temperature  $\hat{T}$  decreases with decreasing strain rate. The transition from regime II to III occurs at a fixed temperature  $\tilde{T}$  and is called lower bend. It is characterized by the fact the extrapolation of the flow stress data, from the regime well below  $\tilde{T}$  to higher temperatures, gives flow stress values that lie significantly below those measured at temperatures above  $\tilde{T}$ .

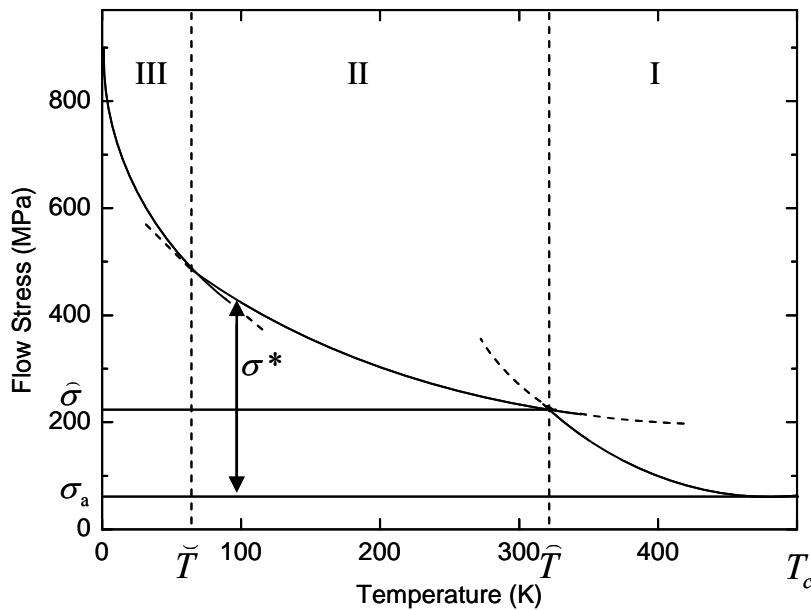


**Figure 2.4:** Typical curve of flow stress versus temperature of bcc metals (adapted from [82]).



According to the theory by Seeger [41] two different models have to be used to calculate the effective flow stress (i.e. the thermal component  $\tau^*$ ) in the temperature interval  $T_c > T > \tilde{T}$ . For small  $\sigma^*$ , i.e. in regime I, the separation between the two kinks of a kink-pair is large and the kink-kink interaction is assumed to be controlled by elastic long-range interactions. The effective flow stress in regime I is given by

$$\sigma^{*1/2} = \ln\left(\frac{\dot{\epsilon}_0}{\dot{\epsilon}_{pl}}\right) k \frac{(T_c - T)}{2\alpha}, \quad \alpha^2 = \frac{a^3 b \zeta_0}{2} \quad (2.7)$$

where  $\dot{\epsilon}_{pl}$  is the plastic strain rate and  $\dot{\epsilon}_0$  is the pre-exponential factor in the Arrhenius equation for the strain rate.  $\zeta_0$  is a pre-logarithmic factor of the dislocation line tension  $\zeta_d$  and  $a$  is the kink height. Equation (2.7) is only valid up to an effective stress  $\tilde{\sigma}$  which indicates the transition from regime I to II. For stress larger than  $\tilde{\sigma}$  the kinks are so close together that their strain fields can no longer be estimated by linear theory of elasticity, and therefore the effective flow stress in regime II has to be calculated based on the line-tension approximation. In contrast to regime I, the effective flow stress of regime II depends on the shape of the Peierls potential  $U$  and is determined by the relationship

$$\frac{T}{T_c} = 1 - \sigma^* \left[ 1 + \ln\left(\frac{\tilde{\sigma}}{\sigma^*}\right) \right] \left[ \frac{\zeta_d}{U''_{(a)}} \right]^{1/2} \frac{ab}{2H_k} \quad (2.8)$$

where  $2H_k$  is the formation enthalpy of two isolated kinks. If the Peierls potential is known,  $U''_{(a)}$  can be expressed in terms of the Peierls stress  $\sigma_p$  as

$$U''_{(a)} = \frac{2b\sigma_p 3^{3/2}}{a} \quad (2.9)$$

and

$$\tilde{\sigma} = 12\sigma_p^{3/2}. \quad (2.10)$$

Fitting of the equations (2.7) and (2.8) to experimental data gives the product  $ab$ , from which the kink height can be obtained. The kink height and hence the distance between adjacent Peierls valleys is a unique signature of the slip planes. Thus, with the quantity  $a$  it is possible to determine the elementary slip plane without further assumptions. For all materials investigated so far, it was found that in the temperature interval  $T_c > T > \tilde{T}$  the elementary

slip occurs on  $\{112\}$  planes [56, 57, 63, 66, 67]. The glide steps in this temperature interval are wavy and approximately follow the traces of slip planes with the maximal resolved shear stress [42]. However, below  $\tilde{T}$  the slip lines are straight indicating that the lower bend in the stress-temperature behavior (Fig. 2.4) is related to a drastic change in the deformation mechanism. In the temperature interval  $\tilde{T} > T > 0$ , slip line analysis [30, 42] and computer simulations [75-78] demonstrated that slip occurs on the  $\{110\}$  plane with the largest Schmid factor, i.e. on the primary slip plane. According to Seeger's theory, this change of the elementary slip plane, from  $\{110\}$  in regime III to  $\{112\}$  in regime II at the transition temperature  $\tilde{T}$ , is due to a first-order phase transition of the dislocation core. The different dislocation core configurations are considered as 'ground state' and 'excited state', the phase transformation from the low-temperature  $\{110\}$  configuration to the high-temperature  $\{112\}$  configuration occurs when the free enthalpy of the two states are equal. The dislocation core in the ground state is three-fold and is able to slip on any of the three  $\{110\}$  planes intersecting the  $\langle 111 \rangle$  crystallographic axis of the dislocation core. Under the action of a finite stress  $\sigma^*$ , the three-fold symmetry is broken and the one of the three  $\{110\}$  planes with the highest Schmid factor acts as glide plane. In contrast, the core in the excited state is three-fold degenerated and each of the core configurations can slip on a different  $\{112\}$  plane. In the equilibrium between the excited state and the ground state, dislocation segments can fall back into the ground state and can subsequently occupy a different high-temperature configuration in the excited state. This change of the elementary glide plane appears mesoscopically as cross-slip and is directly related to the waviness of the slip steps in the temperature interval  $T_c > T > \tilde{T}$  [53].

Based on Seeger's kink-pair theory, Brunner and Diehl [81] presented a slightly different interpretation of the three regimes in Fig. 2.4. In agreement with Seeger, their theory predicts that kink-pair nucleation occurs on  $\{112\}$  planes in regime I governed by the elastic-interaction approximation and on  $\{110\}$  planes in regime III corresponding to the line-tension approximation. However, according to Brunner and Diehl [81], the kinks propagate on the same plane in regime II as in regime III with the difference that in regime II the formation of pairs of constriction is more important than kink formation.

Even if there is some uncertainty about the elementary slip plane in regime II, the analysis of the stress-temperature dependence of the flow stress in terms of Seeger's kink-pair theory has provided insights into the elementary slip planes of bcc metals. It was shown that there is a

transition from low temperature slip on  $\{110\}$  planes to high temperature slip on  $\{112\}$  planes.

### 2.1.3 Strain Hardening Behavior of Single Crystals

Usually, the strain hardening behavior of a material is measured in a tensile or compression test in which the sample is deformed at a constant rate. Plastic deformation occurs if the critical resolved shear stress is reached on a specific glide plane (chapter 2.1.1). During subsequent deformation the stress to maintain plastic deformation increases due to the multiplication and interaction of dislocations. The tendency for a crystalline material to become stronger with increasing strain is referred to as strain hardening or work hardening [44, 45, 83, 84]. Experiments have shown that the strain hardening behavior of fcc and hexagonal close-packed (hcp) metals deformed at room temperature is strongly related to the sample orientation [85-88]. Fig. 2.5 shows representative stress-strain curves for fcc single crystals oriented for single (curve 1) and multiple slip (curve 2).

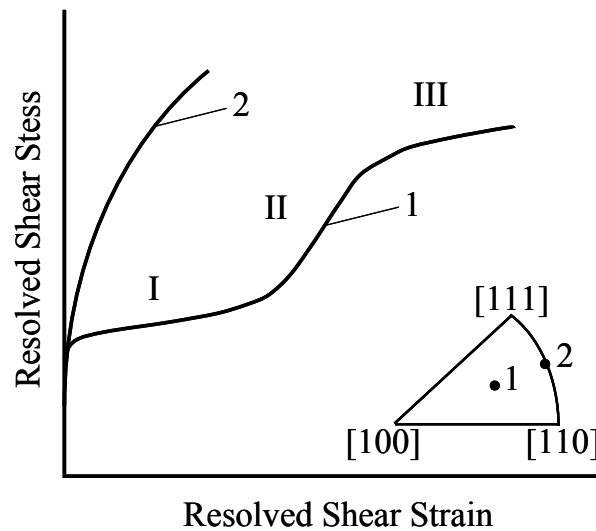


**Figure 2.5:** Typical shear stress-shear strain curve for single crystals with single slip (1) and multiple slip orientation (2).

In the case of the single slip orientation plastic deformation occurs initially at an almost constant stress (stage I) up to a certain amount of plastic strain where strain hardening becomes significant. The increasing strain hardening rate is characteristic for the transition from stage I to stage II. In stage II, the strain hardening rate is almost independent of the crystallographic orientation and is on the order of  $\mu/300$  (e.g. [83], p. 127), where  $\mu$  is the shear modulus of the material. Finally, in stage III the strength continues to increase, but the strain hardening rate progressively decreases. For a single crystal oriented such that multiple slip is favored, stage I does not occur and significant strain hardening is observed over the

entire range of plastic flow. A theory for the three-stage hardening of fcc metals was proposed by Seeger [89], p. 243. Accordingly, dislocation motion in stage I occurs only on the most favorable slip system, which is called the primary slip system, and the low work hardening rate in stage I is related to the elastic interaction of individual dislocations with the same Burgers vector. As the deformation progresses, dislocations start to multiply and pile up at obstacles. This results in the accumulation of internal stress and consequently in the activation of less favorable slip systems (secondary slip systems). Dislocations on the primary and secondary slip systems can react with each other, which results in the formation of sessile dislocation configurations such as Lomer-Cottrell locks. These are strong barriers to the glide of other dislocations and thus the stress for further deformation rises explaining the high strain hardening rate in stage II. The beginning of stage III is related to the onset of thermally activated cross-slip of screw dislocations. By this mechanism the dislocations can overcome obstacles and screw dislocations with opposite signs can annihilate. Consequently, the dislocation density and the internal stress are reduced, resulting in a decreasing strain hardening rate for stage III.

The plastic deformation of bcc metals was found to be more complex than for fcc and hcp metals [31, 32, 84, 90]. Experiments on several bcc metals have demonstrated that yield stress, slip planes and dislocation arrangements in the crystal depend on temperature, orientation and rate of deformation [31, 32]. These observations are linked to the complicated core structure of screw dislocations in bcc metals (chapter 2.1.2). It has been recognized that beyond the yield stress the deformation of bcc metals is controlled by the thermally activated motion of screw dislocations. This results in a temperature dependent strain hardening behavior of bcc metals: At elevated temperatures bcc crystals oriented for single slip exhibit fcc-like three-stage hardening. However, as screw dislocations have the ability to cross slip once the critical resolved shear stress is reached, the extent of stage II is reduced to an inflection point. The work hardening rate determined from the maximum slope of the shear stress-shear strain curves are of the order  $\mu/600$  to  $\mu/500$  [90]. In the low temperature range, stage I work hardening is absent and the stress-strain curve is parabolic in shape. The high initial work hardening at low temperatures, sometimes referred to as stage 0 hardening, is related to the motion of grown-in edge dislocations. These are much more mobile than screw dislocations and can therefore move at a lower stress. However, the strain generated by the edge dislocations is limited, because dislocation multiplication cannot occur without screw dislocation motion. After the sample is depleted of mobile edge dislocations, the stress has to rise to initiate screw dislocation motion, which is responsible for the initial hardening

observed in stage 0. Beyond this micro-strain regime the deformation is entirely accommodated by the thermally activated screw dislocation motion. As a result, the flow stress is mostly determined by the effective stress associated with the screw dislocation motion and the hardening caused by dislocation-dislocation interactions is a minor contribution. In addition, it was demonstrated that for bcc metals deformed at low temperatures the screw dislocation density reaches a saturation value during the deformation [32]. Thus, bcc metals deformed beyond stage 0 exhibit very little strain hardening. At temperatures where sufficient thermal activation of the screw dislocations suppresses the difference between the mobilities of edge and screw dislocations, the strain hardening behavior of bcc metals resembles that of fcc metals [90]. This indicates that at elevated temperatures the mechanism responsible for the strain hardening is similar for fcc and bcc metals. Essentially, Sestak and Seeger [90] have shown that beyond the inflection point in the strain hardening curve, the dislocation arrangement and the slip line pattern of bcc metals are similar to those in stage III of fcc metals. Thus, the strain hardening of bcc metals is likely caused by the dislocation processes characteristic of stage III hardening in fcc metals, which is a reasonable assumption as in both cases the deformation is controlled by the cross-slip of screw dislocations.

## 2.2 Literature Review

### 2.2.1 *Mechanical Properties of Small-Scale Metal Structures*

In pure bulk metals the athermal part of equation (2.2) is determined by the interaction of dislocations with microstructural features such as grain boundaries and other dislocations [44, 45]. As microstructural length scales are typically much smaller than the sample size, the flow stress of bulk metals is independent of the sample size. However, if the sample size is of the order of tens of microns and smaller, i.e. comparable to microstructural length scales, so called size effects and local fluctuations in the microstructure begin to have a significant influence on the flow stress of metals [1]. Size effects in bending [91], torsion [92], or indentation [10, 13, 93, 94] have been attributed to plastic strain gradients. It is assumed that the sample flow stress increases due to an additional density of dislocations, i.e. geometrically necessary dislocations, associated with the accommodation of size dependent strain gradients [92, 95, 96]. However, size effects can arise even if the applied deformation is uniform. Typically, this occurs when the dislocation motion is constrained, as e.g. in thin films on hard

substrates [1, 10, 97]. The film/substrate interface and the surface of the film are impenetrable obstacles for the dislocations if they are passivated by a natural oxide or additional barrier layer [2, 3, 98, 99]. Consequently, the dislocations have to bow out between these obstacles, as shown in Fig. 2.6 for a passivated and an unpassivated film on a substrate. The thinner the film, the higher the curvature of the dislocation and consequently higher stresses are required for their propagation.

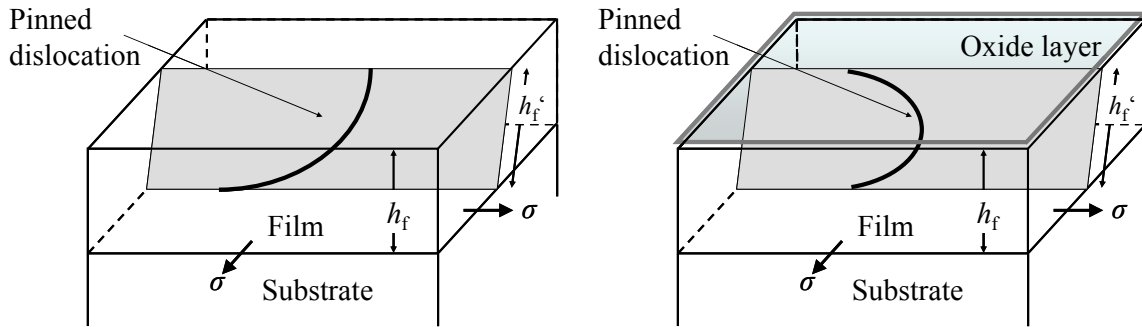


**Figure 2.6:** Schematic representation of a moving dislocation in a single crystalline film with a free (left) and a passivated (right) surface. The film thickness is  $h_f$  and the effective distance between the pinning points is  $h_f^c$ .

Various theoretical models have been proposed to explain the size effect of thin films [10-13]. The most prominent is the Nix-Freund model where it is assumed that the confined motion of threading dislocations results in the deposition of misfit dislocations at the interface [9, 10]. This model succeeds in describing the film thickness dependence of the flow stress of epitaxial Al and Cu films on sapphire [2, 3]. However, it significantly underestimates the flow stress of polycrystalline films [2, 3, 98-100]. This discrepancy has been attributed to the interaction of dislocations with grain boundaries. In early approaches [1, 100, 101] the grain size effect was considered by a superposition of the classical Hall-Petch model [102, 103] and the Nix-Freund model [9, 10]. Another mechanism for the grain size effect was proposed independently by Chaudhari [11] and Thompson [12]. They assumed that misfit dislocations also have to be deposited at grain boundaries. However, the experimental verification of the suggested mechanisms is currently not available and the models still underestimate the measured flow stresses of polycrystalline films [98, 99, 104]. To bridge the gap between theory and experiment the contribution of dislocation interactions was analyzed theoretically [105] and in discrete dislocation dynamics simulations [106-109]. Beside the models based on constraints on dislocation glide, v. Blanckenhagen et al. [110-112] developed a model where the size effect of thin films is rationalized in terms of constrained dislocation nucleation. Using dislocation dynamics simulations, they showed that the activation of Frank Read type dislocation sources might control the flow stress of thin films. The stress to activate a

dislocation source was correlated to the smallest geometrical or microstructural dimension explaining the high flow stresses of thin and fine grained films [2, 3, 98, 99]. So far, the dislocation processes assumed in the v. Blanckenhagen model have not been observed experimentally [98, 113]. However, the nucleation of dislocations in a perfect crystal is proposed to be the reason for the elevated yield stress measured in the initial stage of nanoindentation, where the tested volume is extremely small and likely free of dislocations [15, 18, 114, 115]. Similar deformation processes are assumed to account for the high yield stresses of initially dislocation-free metallic whiskers [116-118] and micropillars produced via directional solidification of an eutectic Ni-Al-Mo alloy and subsequent etching [119, 120].

Interestingly, many recent experiments on FIB machined single crystalline micro- and nanopillars have shown that the yield strength in metals is size dependent even for an unconstrained geometry, with non-zero initial dislocation density in the absence of strain gradients [20-29]. In these experiments, pillars with diameters ranging from 200 nm to 40  $\mu\text{m}$  were machined from bulk single crystals or in individual grains of a polycrystal using a FIB and subsequently compressed with a nanoindenter equipped with a flat tip. Fig. 2.7 shows a  $\langle 269 \rangle$  Ni pillar in contact with the flat indenter tip (image taken from [23]).

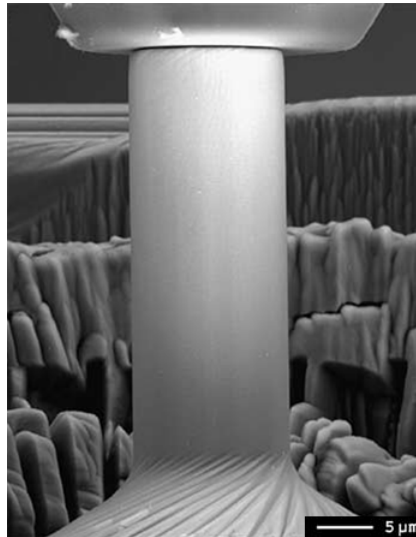


**Figure 2.7:** FIB machined  $\langle 269 \rangle$  Ni micropillar in contact with the flat indenter tip (taken from [23]).

These experiments have consistently demonstrated an inverse scaling of yield strength with sample size for various fcc metals such as Ni [22, 26], Au [21, 24], Cu [28] and Al [27]. In general, the relationship between yield strength  $\sigma_y$  and pillar diameter  $d$  can be described by a power law

$$\sigma_y \propto d^{-n} \quad (2.11)$$

where  $n$  is the power law exponent. For fcc metals the power law exponent was found to be in the range of 0.6 to 1.0 [20-29]. In contrast, the classical Hall-Petch model predicts a power law exponent of 0.5 [102, 103], while source controlled deformation should lead to an exponent of 1.0 [110-112]. The wide scatter of the power law exponent is likely caused by specific testing conditions such as the initial dislocation density, the pillar shape and the strain value at which the yield strength is determined [29]. Nevertheless, if the data of the different studies are compared after the strength values have been normalized with the material specific shear modulus and Burgers vector, the data merge into a single band over a size range from a couple of hundred nanometers up to tens of micrometers [29, 121-124]. This is illustrated in Fig. 2.8 for multiple fcc metals, including Ni [22, 26, 125], Au [21, 24, 126], Cu [28], and Al [27]. The power law exponent that best fits the consolidated data over the entire size range is approximately 0.6.

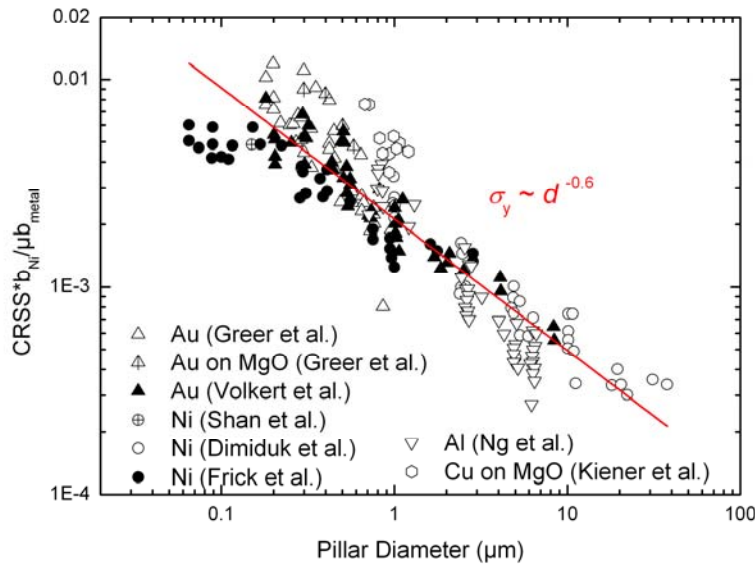


**Figure 2.8:** Comparison plot of CRSS versus diameter showing data for Ni [22, 26, 125], Au [21, 24, 126], Cu [28], and Al [27]. CRSS values have been normalized with respect to resolved shear modulus and Burgers vector to facilitate direct comparison. The solid line shows the best fit to the data with a slope of -0.6.

One of the first explanations for the size effect of FIB machined micropillars was the starvation theory [21, 127, 128]. The model assumes that the sample will starve of mobile dislocations if the rate of dislocation ejection at the sample surface is larger than the rate of dislocation multiplication via double cross-slip or similar processes. Consequently, new dislocations have to be nucleated from dislocation sources. The size effect is then rationalized by the correlation of source size with sample size leading to higher yield stresses for smaller pillars. This model was supported by simulations [129-131] and recent *post mortem* TEM



investigations [27, 127] as well as *in situ* TEM experiments [125]. The *in situ* TEM experiments have shown that preexisting dislocations, likely caused by the FIB-cutting procedure, leave the pillars with diameters between 200 and 300 nm during initial loading. For larger pillars it was observed that dislocations remained in the pillars even after loading to 2.6 GPa. This is consistent with *post mortem* TEM experiments which exhibited an increase in the dislocation density for submicrometer  $\langle 111 \rangle$  Ni pillars [26] and for  $\langle 269 \rangle$  Ni micropillars [132]. As a dislocation starved state was experimentally verified only for pillar diameters smaller than approximately 300 nm, other theoretical models were developed to explain the size effect over the whole size range investigated with the microcompression technique.

Based on large-scale three-dimensional dislocation simulations, Rao et al. [133] proposed a strengthening mechanism caused by the formation of single arm dislocations sources. Accordingly, the operation of a Frank Read source in the vicinity of the free surface results in the formation of two single arm dislocation sources after the emitted dislocation encounters the surface. The arm length of the single arm source can be small compared to the length of the original Frank Read source and thus higher stresses are required for their operation. The critical configuration for the single arm sources is given by the shortest distance between the pinning point and the surface. As for double ended sources the weakest single ended source, i.e. the one with the longest critical arm length, determines the flow stress. Further, this process limits the distance that a dislocation can move to the width of the pillar, because the dislocation can only spiral around the pinning point. This reduces the possibility for cross-slip multiplication and thus may lead to a pillar starved of mobile dislocations. The operation of single ended dislocation sources was recently observed in simulations [134-136]. By considering the statistical variation of the source length, Parthasarathy et al. have demonstrated that the model can account for the experimental yield stresses of Ni and Au micropillars [137].

Apart from the size effect in yield strength, the intermittency of plastic flow is another feature of micropillar deformation [29, 123, 138, 139]. For a load controlled experiment the strain response of a single crystalline micropillar is composed of discrete strain bursts with almost no strain hardening separated by regimes of nearly elastic loading. This is shown in Fig. 2.9 for submicrometer sized  $\langle 111 \rangle$  Ni pillars [26].

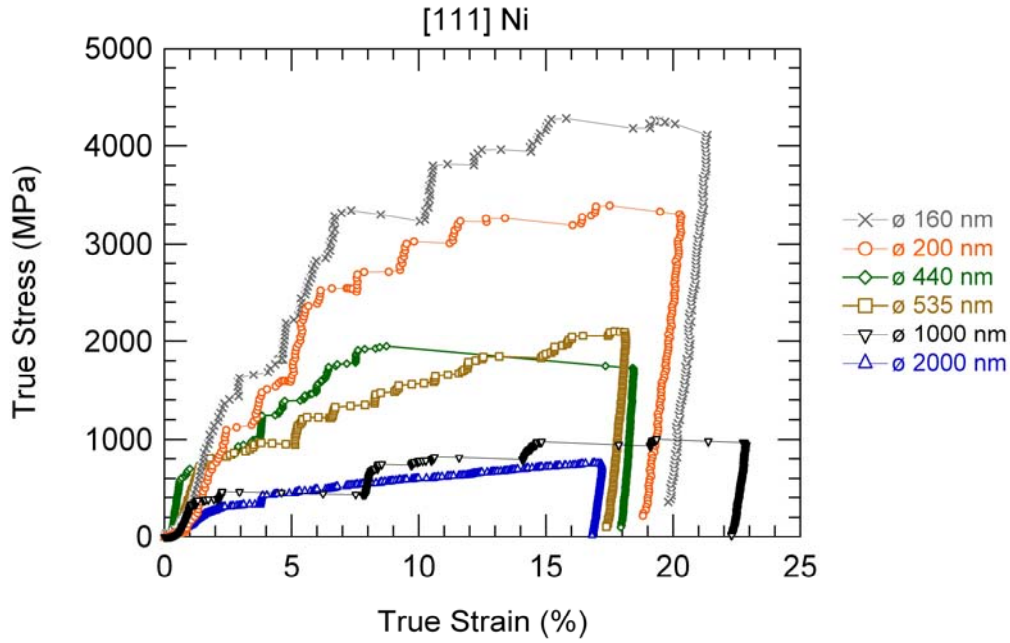


**Figure 2.9:** Stress-strain curves for  $\langle 111 \rangle$  Ni pillars with diameters ranging from 160 to 2000 nm, from [26]. The stress-strain response is composed of strain bursts separated by nearly elastic loading.

The intermittency of the plastic flow for micropillars is in contrast to the continuous stress-strain response of bulk metals. Typically, the strain bursts are related to dislocation avalanches propagating through the sample [29]. In small dimensions these events may lead to a considerable amount of strain, while for a macroscopic sample the same events may lead to very small strains. If the time span of such a dislocation event is small compared to the imposed loading rate, deformation occurs at a constant stress level resulting in a strain burst for a load controlled experiment. In contrast, for a displacement controlled experiment the dislocation event leads to a load drop, because the pillar loses contact with the indenter tip and the contact force is reduced until the indenter tip catches up with the deformed sample [124].

The magnitude and the frequency of the strain bursts are random and they occur stochastically at stresses higher than the elastic limit of the sample. Statistical analyses [22, 126, 138-140] of the strain burst behavior have shown that the number and magnitude of the dislocation events exhibit a power law scaling. For the data published and analyzed so far a power law exponent of approximately -1.6 was found [29, 123]. According to the starvation theory [21, 127] the first strain burst in the stress-strain curve is related to the activation of the weakest source. Once the source is activated, the stress is sufficient for the emitted dislocations to propagate through the pillar and to be ejected at the free surface. Consequently, the strain generated by the emitted dislocations is responsible for the strain burst. Further, the theory states that if the rate of dislocation nucleation is small compared to the dislocation escape rate, the sample will be depleted of mobile dislocations for a period of time after the dislocations have encountered

the surface. Thus, the subsequent loading of the sample has to be accommodated by an elastic deformation of the pillar until the next dislocations are emitted. In this way, the successive operation of a single dislocation source can account for plastic strain bursts separated by regimes of elastic loading. However, the constant activation stress of the operative source should lead to a low strain hardening rate, which is in contrast to most of the experimental results [29].

Another mechanism for the intermittency of plastic flow was proposed by three independent studies of Rao et al. [141], Senger et al. [142] and Tang et al. [136], which are based on the limited number of available dislocation sources in small dimensions. It is assumed that due to the limited number of potential sources, the material is very sensitive to the termination of individual sources. If the weakest dislocation source is exhausted by dislocation reactions, the stress has to increase to activate the next source. Due to the limited number of sources, the stress increment to activate the next source may be large compared to a bulk material with a much larger number of potential sources [29]. Consequently, sequential activation and exhaustion of dislocation sources may explain the experimentally observed stress-strain response of micropillars even in a size range where TEM investigations [26, 132] are in conflict with the starvation concept. Moreover, and in contrast to the starvation theory, source exhaustion hardening may also account for the exceptional high strain hardening rates of the micropillars [24, 26].

### 2.2.2 *Microcompression Tests on BCC Metals*

The majority of research investigating the size effect of metals by means of the microcompression technique has focused on fcc metals (chapter 2.2.1). Only limited data exists for metals with non-fcc crystal structure. Very recently Greer et al. [126] and Brinckmann et al. [143] have published first results about the compression behavior of [001] Mo nanopillars. They showed that the behavior of the Mo pillars fundamentally deviates from those of fcc pillars. It was observed that, in contrast to fcc pillars, bcc pillars exhibited continuous stress-strain curves with significant strain hardening and that the strength of the smallest pillars reached only 7% of the theoretical strength, compared to 44% for fcc Au. Further, it was demonstrated that the size dependence of bcc Mo is less pronounced than recently observed on fcc metals. This is shown in Fig. 2.10, where the critical resolved shear stresses of the Mo pillars are compared with data from recent fcc pillar studies [22, 24, 26].

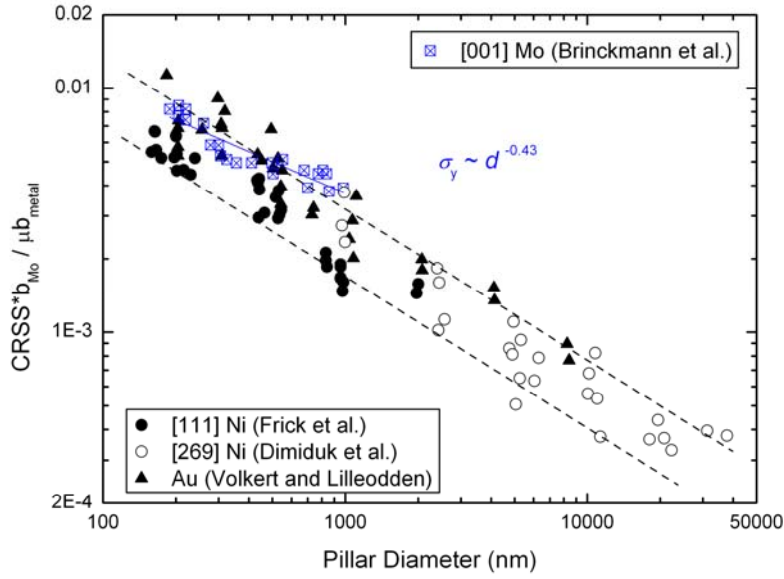


**Figure 2.10:** Comparison plot of CRSS versus diameter showing [001] Mo pillar data from [143], along with compression data for [111] Ni, [269] Ni, and low symmetry Au pillars [22, 24, 26]. CRSS values have been normalized with respect to resolved shear modulus and Burgers vector to facilitate direct comparison.

Based on their experimental observations and supported by DD simulations they argued that the difference between fcc and bcc pillars is caused by different deformation mechanisms. For fcc pillars it was proposed that dislocation starvation causes intermittent plastic flow at very high stresses, while for bcc pillars the long residence time of screw dislocations associated with their low mobility enhances dislocation reactions and junction formation. Consequently, they concluded that for bcc pillars the stress-strain response as well as the size dependence is dominated by conventional forest hardening.

In the DD simulations by Greer et al. [126] the glide loops were placed on (111) planes for the fcc structure and on (110) planes for the bcc structure, as shown in Fig. 2.11 and 2.12. In the case of fcc the dislocations were restricted to the assumed glide planes due to the dissociation into partial dislocations. For the bcc structure screw dislocations were allowed to cross-slip between any of the glide planes which intersect the  $\langle 111 \rangle$  zone axis. In addition, similar dislocation mobilities were used for edge and screw dislocations in fcc while for bcc the edge dislocations were 10 times faster than edge dislocations. The simulations showed that in fcc pillars the dislocation moves across the glide plane and annihilates at the surface, as proposed by the starvation theory (Fig. 2.11). In the bcc structure, the edge component of the dislocation exits the pillar relatively fast, however, leaving behind a long and slowly moving screw dislocation (Fig. 2.12). Interestingly, they observed that as the screw dislocation encounters the opposite side of the pillar a cusp is formed on the screw dislocation. The cusp evolved into a dislocation loop and after the edge components of the loop left the pillar, two

screw dislocations remained on the glide plane. Under the action of the applied load the screw dislocations moved in opposite directions were they repeated this self replication process. Thus, the simulations by Greer et al. [126] suggested that in bcc pillars the residence time of dislocations is longer than in fcc pillars and that there exists an effective mechanism for dislocation multiplication. Accordingly, the probabilities for dislocation reactions and junction formation are elevated for bcc pillars.

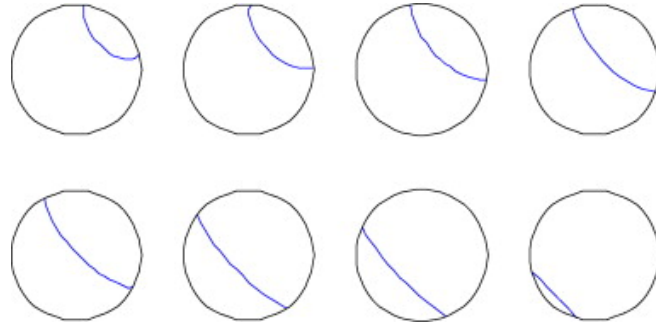


**Figure 2.11:** Snapshots of DD simulation, taken from [126]. Dislocation gliding along (111) plane in a fcc pillar (viewing along the cylinder axis). The dislocations quickly escape to the surface leaving a dislocation starved cylinder.

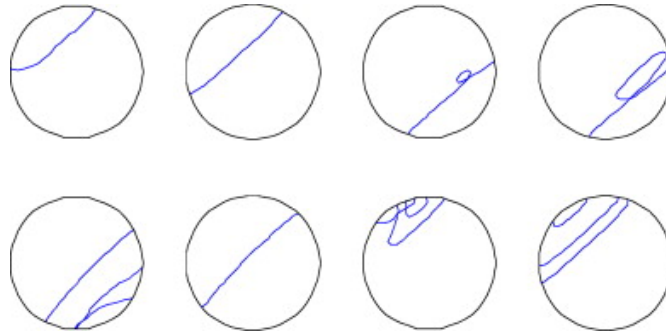


**Figure 2.12:** Snapshots of DD simulation, taken from [126]. Dislocations gliding along (110) plane in a bcc pillar. The dislocation orients as a screw and emits additional dislocations promoting strain hardening.

Similar results were obtained by molecular dynamics (MD) and DD simulations in a comprehensive study by Weinberger and Cai [144]. They pointed out that there are three important steps for the formation of a dislocation cusp, which are responsible for the self replication of the screw dislocation: (1) The formation of a long and straight screw dislocation ranging across the width of the pillar. (2) The motion of screw dislocations controlled by single-kink formation at the surface, in contrast to a kink-pair formation in the bulk material. (3) The two surface nodes, where the screw dislocation intersects the pillar surface, moving on different glide planes. Thus, the formation of surfaces-kinks occurs on different glide planes and if the kinks approach each other in the interior of the pillar they likely form a cusp.

By statistically analyzing the burst behavior of [235] and [001] micrometer and nanometer sized Mo pillars Zaiser et al. [145] showed that the scale-free size distribution of the

intermittent bursts is remarkably similar for fcc and bcc pillars. Independent of pillar size and orientation a power law distribution was found for the burst size, with a power law exponent of -1.55, which is consistent with experimental findings on fcc pillars [138, 139]. Therefore, it was assumed that the high Peierls potential of the screw dislocations in the bcc crystal structure has no influence on the burst statistics. Several explanations for this conclusion were proposed: (1) The burst behavior is not related to a specific deformation process; it is a universal feature of dislocation plasticity. (2) In small dimensions, the motion of screw dislocations is controlled by single-kink nucleation at the surface. (3) The strain generated by the fast moving edge dislocations may be significant in small dimensions and thus the imposed deformation is accommodated by the motion of edge dislocations. However, the different size dependence for fcc and bcc pillars indicates that the deformation processes are somehow affected by the crystal structure.

Finally, in a very recent study Kim and Greer [146] investigated the effect of the initial dislocation density as well as the effect of surface area to volume ratio on the mechanical behavior of [001] Mo pillars. The initial dislocation density was increased by cutting pillars in the proximity of nanoindents and the surface area for a constant cross-sectional area was increased by cutting tube-shaped pillars. Both were found to have almost no influence on the yield strength of the pillars. The higher initial dislocation density only slightly increased the strain hardening rate. Based on these observations, they concluded that there is no hardened surface related to the FIB-cutting and that the dislocation activity occurs in the bulk of the pillar as well as at the free surface. Further, the insensitivity to an increase in the dislocation density was explained in terms of dislocation starvation, which is in contrast to earlier studies by Greer and Nix [127]. The effect on the strain hardening rate was related to increased dislocation density impeding the motion of the gliding dislocations. It has to be mentioned that this insensitivity of the yield stresses to the initial dislocation density differs from the results of Bei et al. [120]. They demonstrated that bcc Mo alloy pillars, which were produced via directional solidification of an eutectic Ni-Al-Mo alloy and subsequent etching, are significantly weaker after pre-deformation. This discrepancy, however, is probably a result of a different starting microstructure. Pillars produced with etching techniques are initially free of defects and thus behave in a whisker-like manner. To deform these pillars, dislocations have to be nucleated in a perfect crystal, which requires stresses close to the theoretical limit. However, once deformed, residual defects act as dislocation sources effectively lowering the yield strength. In contrast, FIB machining does not yield a dislocation free sample, which is

likely the reason for the insensitivity to a variation in the dislocation density for FIB machined bcc pillars.

### 2.2.3 *Summary and Motivation*

In summary, only a few studies have focused on the mechanical behavior of FIB machined bcc pillars. The studies by Greer et al. [126], Brinckmann et al. [143], Zaiser et al. [145] and Kim and Greer [146] have investigated Mo micro- and nanopillars; however, no data exist for other bcc metals. In the studies by Greer et al. [126] and Brinckmann et al. [143] it was proposed that the deformation of the Mo pillars is dominated by conventional forest hardening associated with the low mobility of screw dislocations in bcc Mo. In contrast, Zaiser et al. [145] have concluded that the Peierls potential has a negligible effect on the stress-strain response of [001] and [235] Mo pillars. Further, the studies by Kim and Greer [146] and Bei et al. [120] have demonstrated different effects of the initial dislocation density. While the yield stress was not affected by an increase in the dislocation density in [146], a significant decrease of the yield stress was observed for the Mo alloy pillars in [120].

Thus, currently the experimental findings are inconclusive and there is much uncertainty with respect to the deformation mechanism, the contribution of the Peierls potential and the effect of the initial dislocation density in small-scale bcc metals pillars. Other aspects like the temperature and strain rate dependence of the yield strength have not been investigated so far, even if these are characteristic deformation features inherent to the bcc crystal structure. Besides this, the effect of pillar orientation has been analyzed only in one study by Zaiser et al. [145].

The aim of this study is therefore to shed more light on the deformation behavior of FIB machined bcc metal pillars. The size dependence of the mechanical properties will be studied for several bcc metals over a size range from some hundreds of nanometers to a few micrometers. Temperature and strain rate dependence will be measured at the micro- and nanoscale to examine the role of the Peierls potential at this size. Further, the study will investigate the interplay between size dependent dislocation processes and the temperature dependent contribution related to the screw dislocation motion. Finally, the effect of pillar orientation and initial dislocation density will be addressed to analyze the contribution of dislocation reactions and junction formation.

For this purpose, pillars with diameters ranging from 200 nm to 6  $\mu\text{m}$  were FIB machined from tungsten (W), molybdenum (Mo) and niobium (Nb) single crystals and subsequently

compressed in a nanoindenter. The influence of the sample size on the mechanical properties is the main topic of chapters 4 and 5. For each material, pillars of similar size were tested with varying loading rates to determine strain rate sensitivities and activation volumes and to identify the temperature dependent deformation processes. The results of these tests are reported in chapter 4 and 8. Furthermore, pillars were pre-strained up to 40% and after further FIB-machining compressed again to study the effect of the initial dislocation density and to separate between starvation effects and strain hardening effects (chapter 6). All experiments were performed using single slip and multiple slip orientations in order to distinguish between effects caused by the number of activated glide systems and effects inherent to the sample size (chapter 7). In all cases, the effect of the applied parameters on the stress-strain behavior as well as on the deformation morphology was analyzed systematically and interpreted in terms of recently proposed small-scale plasticity models and the classical kink-pair theory for bcc metals.



## 3 Experimental

### 3.1 Sample Preparation

High purity single crystals were grown via the Czochralski method by the sample preparation facility of the Max Planck Institute for Metals Research in Stuttgart. Disk-shaped samples of approximately 3 mm in height and 10 mm in diameter with the disk normals parallel to the [001] or [235] crystallographic direction were cut by electron discharge machining after the orientations of the single crystals were determined by Laue diffraction. These orientations were chosen to obtain samples with multiple slip and single slip orientation. Both orientations of a given material were cut from the same bulk single crystal to ensure identical initial dislocation densities in the samples. The surfaces were mechanically ground and polished. For grinding silicon carbide papers with grits of 1200, 2400 and 4000 were used while the polishing was performed using 6  $\mu\text{m}$ , 3  $\mu\text{m}$  and 1  $\mu\text{m}$  diamond suspensions. To remove the mechanical damage layer imposed by the mechanical grinding the samples were subsequently electropolished. The Mo samples were electropolished for 60 seconds in a mixture of 610 ml Methanol and 85 ml  $\text{H}_2\text{SO}_4$  (96%) at a current of 1-2 amperes, whereas the Nb samples were electropolished for 10 seconds in a mixture of 600 ml Methanol and 150 ml  $\text{H}_2\text{SO}_4$  (96%) at the same current. For the W samples, the etching time was 20 seconds at a current of 1-2 amperes with an electrolyte consisting of deionized water, 0.9 mol/l KOH and 0.15 mol/l  $\text{K}_3\text{Fe}(\text{CN})_6$ . Afterwards, the samples were glued onto FIB sample studs, where they remained for further processing and testing. The studs were designed to fit in the FIB and the nanoindenter with small tolerance to ensure that the FIB machined pillars were perfectly aligned with the indenter. This is illustrated in Fig. 3.1.

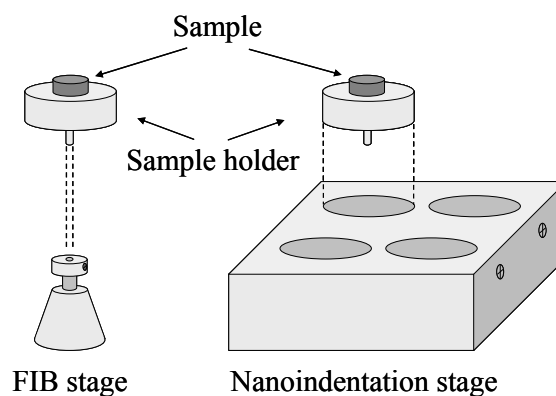


**Figure 3.1:** Schematic showing the designed sample holder, which fits into the FIB stage as well as into the nanoindentation stage.

An FEI Nova 600 Nano Lab Dualbeam<sup>TM</sup> microscope was used to machine the pillars in the as-prepared single crystals. The Dualbeam microscope combines a FIB with a scanning electron microscope (SEM) within one system. To minimize the Ga<sup>+</sup> ion exposure of the samples, the FIB was only used for milling the material, while the imaging was conducted with the SEM. The milling process was performed in two steps, similar to the procedures proposed by Frick et al. [26] and Volkert and Lilleodden [24]. Essentially, the first step led to the rough shape of the pillars at centers of circular craters of 30  $\mu\text{m}$  diameter. The latter was necessary to assure that the indenter only comes into contact with the pillar and not with the surrounding material. For the first step, a beam voltage of 30 kV, a beam current of 7 nA and a beam spot overlap of 80% were used. The milling time was adjusted to obtain pillars with a final length to diameter ratio of approximately 3:1. In the second step, the pillars were fine milled to the final diameters which ranged from 200 nm to 6  $\mu\text{m}$ . The fine milling was performed in multiple steps using currents between 10 pA to 100 pA to minimize the Ga<sup>+</sup> ion damage of the fabricated pillars. It has to be mentioned that this milling technique with normal incidence of the ion beam to the sample surface has its limitations in producing pillars of uniform diameter and well defined gauge length. Better results can be obtained if the pillar is tilted relative to the ion beam, which is realized in the ‘ion-lathe’ method [19, 20]. However, with the latter it is extremely difficult to prepare pillars with diameters less than 1  $\mu\text{m}$ . Thus, all pillars produced in this study had a tapered pillar geometry with taper angles between 2° and 4°, similar to other micropillar studies using the same technique [22, 25, 27].

### 3.2 Microcompression Testing

The as-prepared pillars were tested with an MTS XP nanoindenter equipped with a conical diamond or sapphire indenter with a flat 10  $\mu\text{m}$  tip. All tests were conducted at room temperature under load control at fixed loading rates for prescribed displacements. The experiments were performed at a control rate of 500 Hz and a data storage rate of 25 Hz. For the size effect experiments, the loading rate was scaled with the pillar diameter to obtain constant stress rates for pillars with different diameters. To study time dependent deformation processes inherent to the bcc crystal structure, equal sized pillars of a given material were tested with varying loading rates between 1  $\mu\text{N/s}$  and 500  $\mu\text{N/s}$ . Some tests were performed with intermediate unloading and reloading cycles to determine the elastic response of the tested materials. However, to avoid problems related to a misalignment after subsequent reloading, most of the tests were conducted without intermediate unloading and reloading.

Prior to testing the geometrical parameters of the pillars were determined from SEM images. The length and the diameter of each pillar were required to convert the recorded load-displacement data into a stress-strain curve. Due to the tapered pillar shape, the diameter at the top of the pillar was used to calculate engineering stress. The top diameter  $d$  was chosen because it is well defined and the stress is the highest at the top due to the tapered pillar shape. The pillar height  $h$  was defined as the distance between the approximated intersections of the tapered pillar with the base material and the pillar top, as shown in Fig. 3.2. Consequently, the engineering stress  $\sigma$  and engineering strain  $\varepsilon$  were calculated using the standard formulas:

$$\sigma = \frac{4F}{\pi \cdot d^2} \quad (3.1)$$

and

$$\varepsilon = \frac{\Delta x}{h} \quad (3.2)$$

where  $F$  is the load and  $\Delta x$  is the pillar displacement. It was not attempted to use true stress and true strain because of the inhomogeneous deformation of the pillars by localized slip. Nevertheless, the elastic deformation of the base material and the indenter itself had to be considered in order to determine  $\Delta x$  precisely [26]. Following the work by Sneddon [147], the displacement  $\Delta x$  of the pillar can be expressed by

$$\Delta x = \Delta x_{\text{meas}} - \frac{1 - \nu_i^2}{E_i} \left( \frac{F_{\text{meas}}}{d} \right) - \frac{1 - \nu_s^2}{E_s} \left( \frac{F_{\text{meas}}}{d_b} \right) \quad (3.3)$$

where  $\Delta x_{\text{meas}}$  is the measured displacement and  $F_{\text{meas}}$  is the measured force.  $E_s$  and  $\nu_s$  are the Young's modulus and Poisson's ratio of the tested material, while  $E_i$  and  $\nu_i$  are the Young's modulus and Poisson's ratio of the indenter, respectively. The pillar diameter at the top is  $d$ , whereas the diameter at the bottom is  $d_b$ .

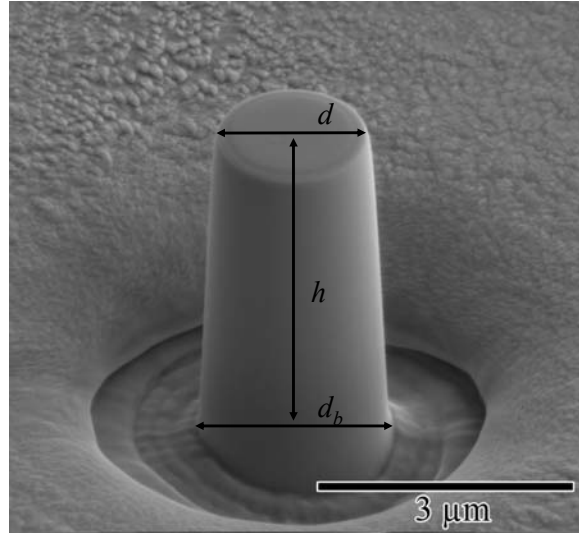


**Figure 3.2:** SEM image taken at 52° tilt of a FIB machined [001] Nb micropillar. The diameter  $d$  measured at the pillar top and the pillar height  $h$  were used to calculate the engineering stress-strain data.

### 3.3 Experimental Limitations

As mentioned above, FIB machined single crystal micropillars are not expected to be free of dislocations and defects. The impact of highly accelerated  $\text{Ga}^+$  ions may lead to a damage layer at the surface of the pillars [29, 148]. TEM investigations have shown that the outer layer of FIB machined Ni [26], Au [127] and Cu [148] pillars is amorphous and that the FIB can lead to the formation of dislocation loops and point defects. Further, TEM studies [26, 127] and Monte Carlo simulations [148] have demonstrated that the thickness of this damage layer is approximately 10 to 20 nm. However, in none of the recent TEM studies pile up of dislocations at the pillar surface was observed, suggesting that the damage layer does not impede the dislocations from leaving the sample. On the contrary, more recent *in situ* TEM compression tests on submicrometer  $\langle 111 \rangle$  Ni pillars have exhibited that the defects caused by the  $\text{Ga}^+$  ions left the pillars during initial loading [125]. Therefore, the FIB may introduce defects in the material, which serve as potential dislocation sources [149]; however, the strengthening effect due to the FIB irradiation damage seems to be negligible. In addition, it was shown that the extent of the damage layer depends on the milling parameters such as the incident angle of the ion beam, the ion energy and the exposure time [148], as well as on material properties such as atomic weight and bonding characteristics [29]. As the cutting parameters of the current study are relatively similar to other pillar studies, the extent of the  $\text{Ga}^+$  damage layer for the tested bcc metals is likely controlled by their specific material properties. However, the atomic weights of the tested bcc refractory metals are between those of recently investigated Al [27], Ni [22, 26], Cu [28] and Au [21, 24]. Further, the interatomic

bonding of the refractory metals is relatively strong as proven by their high melting temperatures compared to other metals. Thus, it is not expected that the extent of the damage layer of the tests materials deviates from other studies.

Another concern related to the FIB cutting procedure is the tapered pillar geometry. Nonuniform stress fields as well as inhomogeneous deformation can arise due to the tapered pillar shape. This effect has been studied analytically [125] and numerically [150] by finite element modeling (FEM). It was shown that the inhomogeneous deformation can lead to an artificial strain hardening rate of the tested pillar and to uncertainties in determining the yield stress. Consequently, special care was taken to minimize the taper angle to the range of 2° to 3°. Further, the pillars were machined with similar taper angles for the full range of diameters, and this self-similarity led to appropriate comparison between different diameters.

A practical concern related to the microcompression technique is the alignment between the pillar and the flat indenter tip [29]. Misalignments greater than 1° can lead to artifacts such as an underestimation of elastic modulus and yield stress. Additionally, it can affect the strain hardening response and can cause buckling of the pillars. To ensure an optimal alignment during the compression tests specimen holders that fit in the FIB and the nanoindenter with low tolerance were used (Fig. 3.1). Moreover, all pillars have been analyzed post deformation to verify that no bending had occurred during testing. For further concerns related to the compression testing such as the stiffness of the nanoindentation system or the integral connection of pillar and substrate, the reader is referred to the review articles by Uchic et al. [29] and Kiener et al. [28].



## 4 Effect of Orientation and Loading Rate on Compression Behavior of Small-Scale Mo Pillars

### 4.1 Abstract

Recently, much work has focused on the size effect in face-centered cubic (fcc) structures, however few pillar studies have focused on body-centered cubic (bcc) metals. This paper explores the role of bcc crystal structure on the size effect, through compression testing of [001] and [235] Molybdenum (Mo) small-scale pillars manufactured by focused ion beam (FIB). The pillar diameters ranged from 200 nm to 5  $\mu\text{m}$ . Results show that the relationship between yield stress and diameter exhibits an inverse relationship ( $\sigma_y \propto d^{-0.22}$  for [001] Mo and  $\sigma_y \propto d^{-0.34}$  for [235] Mo) weaker than that observed for face centered cubic (fcc) metals ( $\sigma_y \propto d^{-0.6 \text{ to } -1.0}$ ). Additional tests at various loading rates revealed that small-scale Mo pillars exhibit a strain rate sensitivity similar to bulk Mo.

## 4.2 Introduction

The mechanical behavior of metals exhibits a size dependence, in which the flow stress is usually inversely proportional to some power of the smallest geometrical dimension. This effect has been convincingly demonstrated for a variety of metals in the micron and nanometer scale. Several mechanical testing techniques (e.g. whiskers [118], nanowires [92, 151], thin films [3, 5, 10], etc.) have confirmed this effect. Recently several studies have also demonstrated a size effect in single crystal metals via compression testing of focused ion beam (FIB) manufactured micro- and nano-pillars [19, 21, 22, 24-26]. Unlike whiskers, and also pillars produced via growth and subsequent etching [119], FIB machined small-scale compression pillars are not initially dislocation free. Consequently, near theoretical strengths are not observed in FIB manufactured pillars, however strength is significantly higher than that measured in bulk. These yield stress values,  $\sigma_y$ , have been shown to correlate with pillar diameter,  $d$ , according to  $\sigma_y \propto d^{-0.6}$  to  $d^{-1.0}$  for all face-center cubic (fcc) metals tested to date [7-11].

A number of theories have been proposed to explain the size effect in fcc pillars. In a study by Greer and Nix on Au pillars, a dislocation starvation theory was put forward [21, 127, 128]. According to this theory, due to the small sample size (and thus the high surface to volume ratio) dislocations leave the pillar at the sample surface more rapidly than new dislocations can be produced, giving rise to a “starved” sample state. As a result, new dislocations must be nucleated within the crystal in order to continue deformation, for which high stresses are required. This concept has been supported by discrete dislocation plasticity analysis [129, 130]. In another Au pillar study, Volkert and Lilleoddeon [24] suggested that the size effect was caused by dislocation source-limited behavior [111, 112], wherein an overall decrease in dislocation density is expected for pillars of decreasing size, and therefore an increase in applied stress is necessary to nucleate/activate sources. Additionally, Parthasarathy et al. [137] developed a mechanistic model which suggests that the finite dimensions of a pillar impose an upper limit to the dislocation source length and give rise to the elevated flow stress. While many efforts have been made to understand the mechanisms responsible for this effect in fcc metals, both through experimentation and theoretical and simulation-based models, little work has been done on alternative crystal structures, such as body-centered cubic (bcc).

The plastic deformation in bcc metals differs fundamentally from that of fcc metals. In bcc metals, the deformation is largely controlled by screw dislocations which, due to the geometry of the glide planes, have non-planar dislocation cores and high Peierls potentials [30, 32, 42,



52, 152]. This intrinsic resistance to their motion can be overcome through thermally activated processes, leading to a strong temperature and strain rate dependence of the flow stress. Although these fundamental differences between the deformation behavior of fcc and bcc metals have been characterized in bulk, it is not well known how the size effect in bcc metals may deviate from that observed in previous fcc studies.

In a recent study by Brinckmann et al. [143] on FIB manufactured bcc Mo pillars, it was proposed that the deformation in bcc pillars was controlled by a mechanism fundamentally different from that in fcc pillars. This idea was based on the experimental observation that the ratio between the measured flow stress for their smallest pillars ( $\sim 200$  nm) and the calculated ideal shear strength was found to be dramatically different. In comparing Au data to Mo data, this ratio was found to be 44% for Au and 7% for Mo. It should be noted, however, that these ratios are highly dependent on the reference used to define the ideal shear strength and the chosen flow stress for the material. For example, using the flow stress of 400 MPa reported by Volkert and Lilleodden for their 200 nm Au pillars [24], and the ideal shear strength for Au of 1390 MPa taken from ab initio calculations by Černý and Pokluda [153] gives a strength ratio of only 14% for Au, which is significantly smaller.

In addition to a difference in the strength ratios for Au and Mo, Brinckmann et al. also observed a different shape for the Mo stress-strain curves. While at smaller diameters curves exhibited jerky flow, at the largest diameter ( $\sim 1\mu\text{m}$ ) the Mo curves were smooth and showed significant strain hardening, which was explained by dislocation-dislocation interaction controlled deformation. This was also supported by a dislocation dynamics simulation by Greer et al. [126], which demonstrated that while in fcc materials the dislocations are able to leave the pillar easily during deformation, in bcc materials this is not the case. By allowing the dislocations to cross-slip readily and by defining the velocity of edge dislocations as 10 times faster than that of screw dislocations, they modeled the behavior of dislocations in a bcc pillar and found that the deformation was dominated by dislocation-dislocation interactions. The screw dislocations in the simulated bcc pillars remained in the crystal longer than the dislocations in fcc pillars, thus allowing for traditional strengthening processes such as junction formation and forest hardening. While this model is able to predict the shape of the curve for the larger pillars, it is unable to explain the transition from smooth to jerky flow as diameter is decreased, or the origin of the size effect in bcc pillars.

In the current study, a broader range of diameters (200 nm to 5  $\mu\text{m}$ ), different orientations, and different loading rates were investigated to study the size effect more extensively than in

previous bcc pillar studies [126, 143, 146]. Through analysis of the size effect in [001] and [235] Mo compression pillars, and through comparison of these results with previous pillar studies, this study sheds light on the role of crystal structure on the deformation mechanisms of metals at small scales.

### 4.3 Experimental Procedure

In order to prepare specimens, two cylindrical Mo single crystal specimens were mechanically and electrochemically polished along the face perpendicular to either the [001] or [235] direction (see [145] for further details). The orientation of the final surface was verified using electron back-scattered diffraction (EBSD). Pillars ranging in diameter from approximately 200 nm to 5  $\mu\text{m}$  were machined with a focused ion beam (FIB) on the surface of both the [001] and [235] Mo single crystal pieces using a DualBeam™ FIB. This instrument, which combines FIB with a scanning electron microscope (SEM), was chosen to reduce exposure to  $\text{Ga}^+$  ions during imaging. In general, pillars were cut with a diameter to length aspect ratio of approximately 3:1, and then compressed in load-control with a nanoindenter fitted with a 10  $\mu\text{m}$  flat sapphire punch. The pillar taper, caused by inherent limitations in the FIB cutting procedure [24], was relatively independent of pillar diameter and found to be on average  $2.9^\circ$  for the Mo pillars. For consistency, the pillar top was used to measure the diameter from which engineering stress-strain was calculated. The methods of fabrication, testing, and analysis were similar to the study by Frick et al. [26].

In order to study the effect of strain rate, additional compression tests were performed on [001] and [235] Mo over a range of loading rates. Loading rate variation was chosen, because it is readily controllable in the inherently load-controlled nanoindenter. This was then converted to an elastic strain rate, by dividing by cross-sectional area and elastic modulus. For the tests on [001], 24 pillars each of 0.37, 0.67, and 1.2  $\mu\text{m}$  diameters were fabricated; for tests on [235], 24 pillars each of 0.35, 0.85, and 3  $\mu\text{m}$  diameters were fabricated. Pillars were then tested at loading rates of 1, 5, 75, 150, 250, and 500  $\mu\text{N/s}$ ; for the 3  $\mu\text{m}$  diameter pillars, additional tests at 750  $\mu\text{N/s}$  were run. All other pillars tested and included in the size effect plot were loaded at 4-250  $\mu\text{N/s}$ , depending on pillar diameter.

## 4.4 Results

Figures 4.1 and 4.2 show representative pillars after deformation: 3  $\mu\text{m}$  and 200 nm diameter [001] Mo pillars (Figures 4.1a and 4.1b), and 3.2  $\mu\text{m}$  and 430 nm diameter [235] Mo pillars (Figures 4.2a and 4.2b). Regardless of size, the [001] Mo pillars exhibited slip along multiple systems, as evidenced by the geometry of slip traces in Figure 4.1, while the [235] Mo pillars exhibited primarily single slip along a preferred slip system (Figure 4.2). As seen in Figures 4.1 and 4.2, the larger pillars had a tendency to display slip traces on the pillar surface throughout their length, while pillars with diameters less than approximately 500 nm were more likely to exhibit observable slip deformation closer to the pillar top. Qualitatively similar behavior has been observed in previous pillar studies [24, 26, 125]. In addition to SEM observation, EBSD of selected post-compression pillars were performed. The measurements were made perpendicular to the pillar top and designed to identify if pillars had significantly bent relative to the surrounding matrix. Results showed that the pillar tops retained their original [001] and [235] orientations, suggesting that the pillars remained parallel during testing.

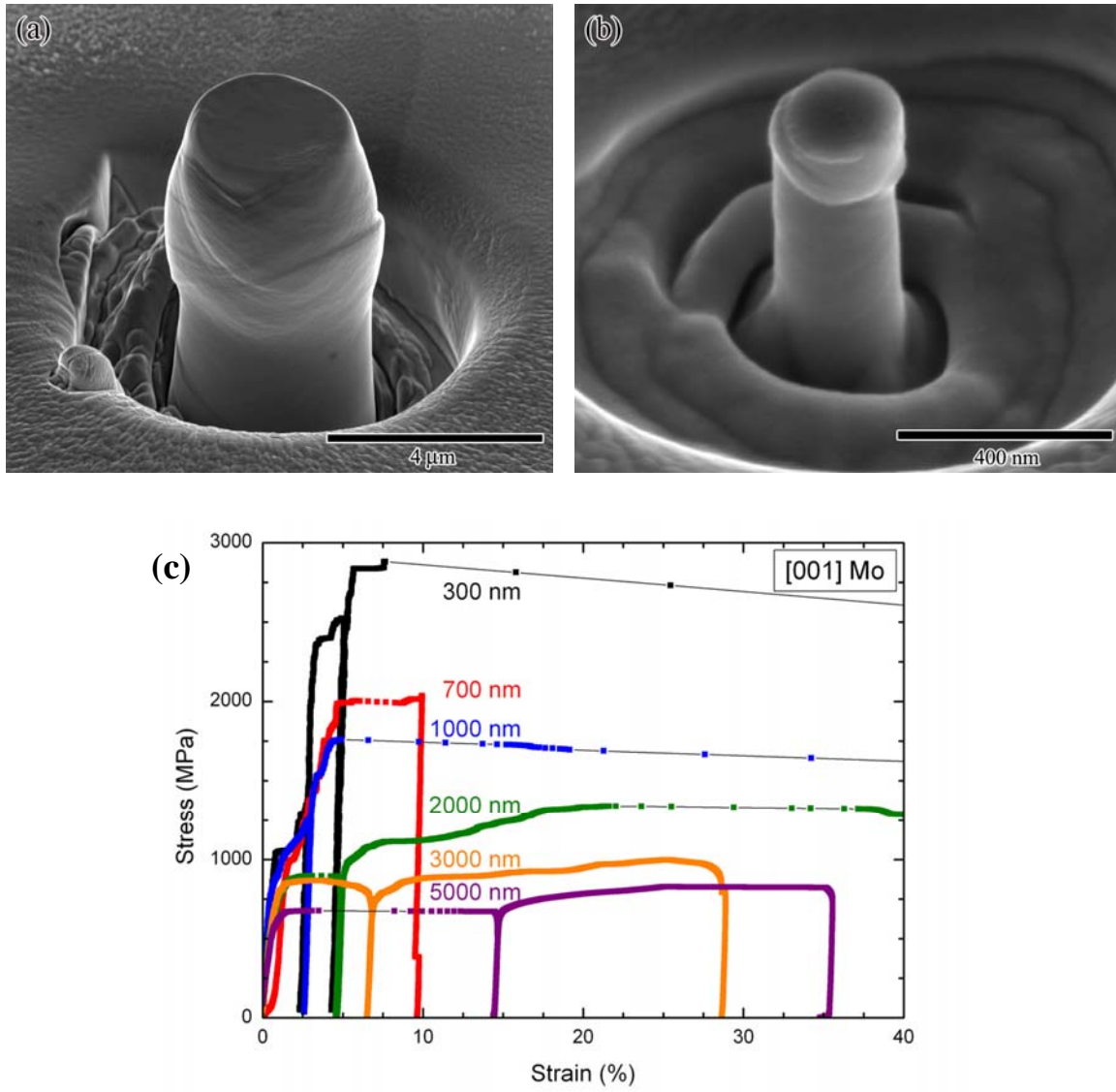


**Figure 4.1:** Post-compression images of [001] Mo pillars of (a) 3  $\mu\text{m}$  and (b) 200 nm diameter. Slip traces on the pillars surfaces confirm multiple slip. (c) Stress-strain plot for [001] Mo pillars over a range of diameters from 300 nm to 5  $\mu\text{m}$ .

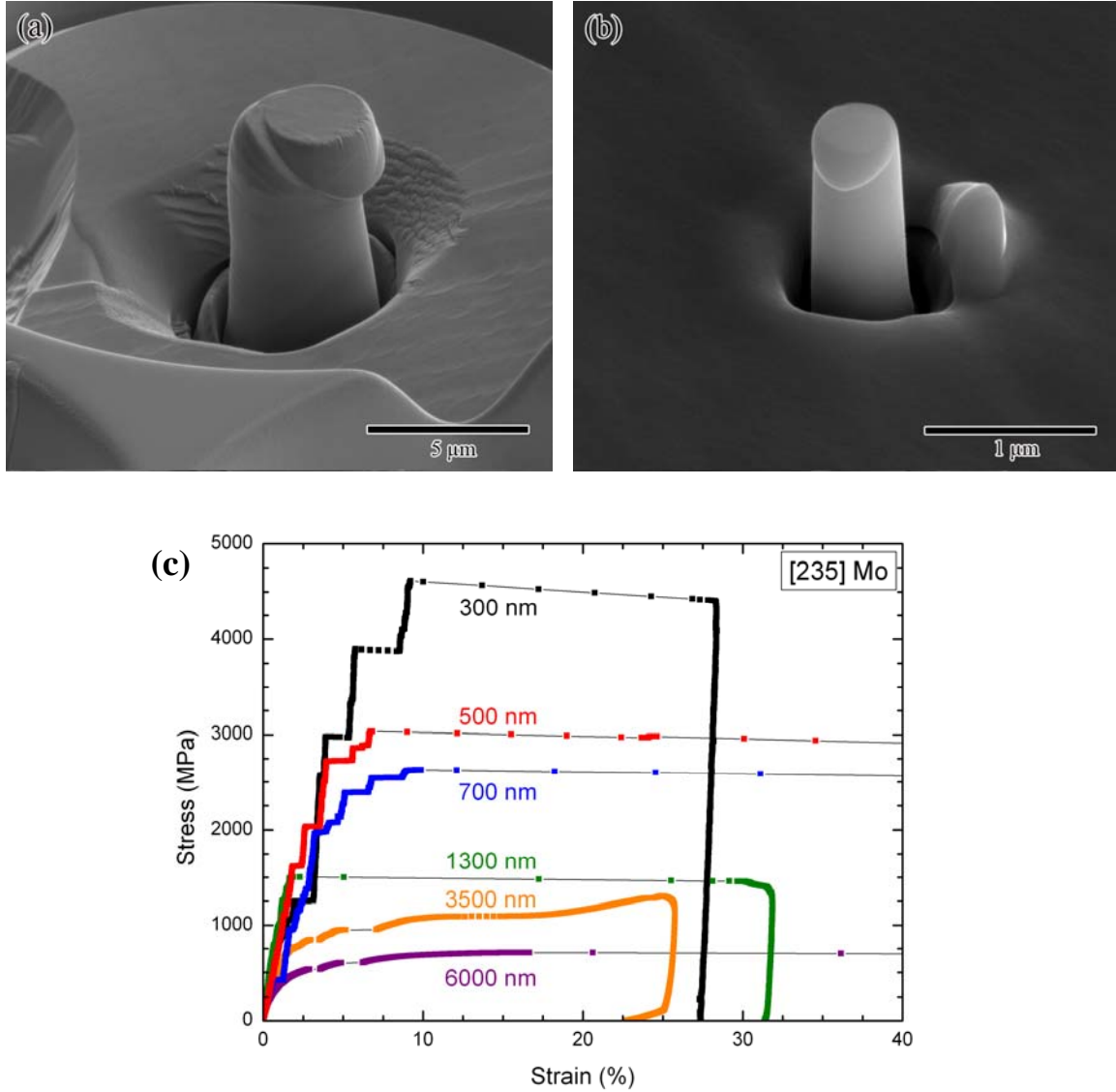


**Figure 4.2:** Post-compression images of [235] Mo pillars of (a) 3.2  $\mu\text{m}$  and (b) 430 nm diameter. Slip traces on the pillars surfaces confirm single slip. (c) Stress-strain plot for [235] Mo pillars over a range of diameters from 300 nm to 5  $\mu\text{m}$ .

Shown in Figures 4.1c and 4.2c are representative stress-strain curves for [001] and [235] Mo pillars, respectively. Both orientations show ‘staircase-like’ stress-strain behavior, qualitatively similar to that observed in prior pillar studies [19, 22, 24, 26, 127] for diameters less than approximately 3  $\mu\text{m}$ . At larger diameters, a gradual transition from discontinuous elastic to smooth plastic deformation is seen, similar to bulk. Also of note is that the larger pillars show less apparent strain hardening than smaller pillars; the increase in stress from 3% to 10% strain is much larger for thinner pillars compared to thicker ones. A similar observation was made in fcc Au [24] and in [111] fcc Ni [26]. When comparing the flow stress values for the two orientations, the [235] Mo pillars exhibit higher stresses relative to the [001] Mo pillars of comparable diameters. Regardless, for both Mo orientations, the flow stress is consistently larger for decreasing pillar diameters, indicating a size effect.

The increase in stress with decreasing diameter is quantified in Figure 4.3, which shows critical resolved shear stress (CRSS) at 2.5% strain plotted as a function of pillar diameter on a log-log scale for both Mo orientations. Stress at an axial strain of 2.5% was chosen as a representation of yield stress as it is high enough to ensure that plastic deformation has occurred, while still low enough to limit the influence of the strain hardening. For the calculation of the CRSS values, the active glide plane was taken to be the (112) plane, resulting in Schmid factors of 0.47 and 0.45 for the [001] and the [235] orientation, respectively. For comparison, choosing the (110) glide plane gives Schmid factors of 0.41 and 0.45. Thus the assumption of the (112) glide plane shifts the absolute values for the [001] orientation 14.6 % upwards, but has no influence on the stress values for the [235] orientation. As shown in Figure 4.3, the relationship between the CRSS and diameter for single crystal Mo is affected by orientation; using a power law fit, slopes of -0.22 and -0.34 were calculated for the [001] and the [235] orientations, respectively. In comparison, a study by Greer et al. found a slope of -0.45 for their [001] Mo pillars, using axial stress measured at 10% strain [126]. If the data in this study is plotted at 10% strain, a similar relationship is found, however CRSS at 2.5% strain was chosen for this study to determine the size effect at the onset of plasticity, since values taken at higher strains are more strongly influenced by strain hardening.

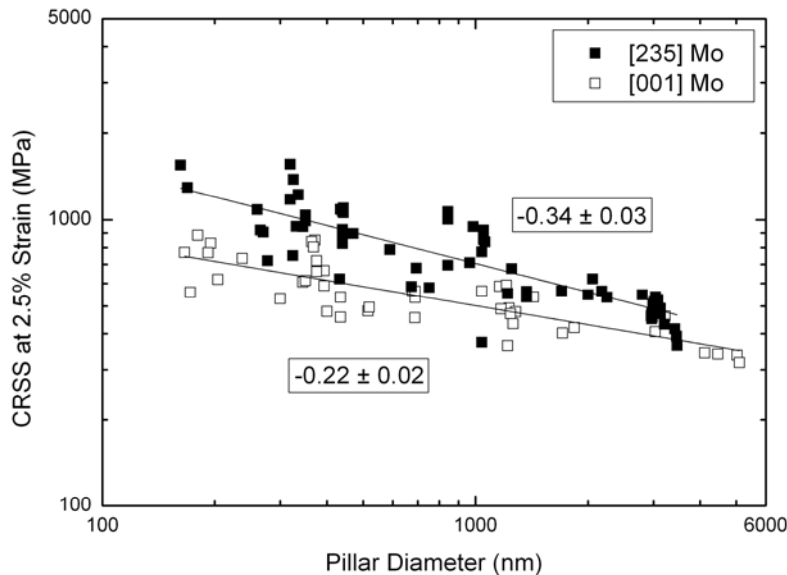


**Figure 4.3:** Critical resolved shear stress taken at 2.5% strain plotted versus pillar diameter for [001] and [235] Mo pillars in this study. Plot is scaled logarithmically, and shows a relationship of  $\text{CRSS}_{\epsilon=2.5\%} \propto d^{-0.22}$  for [001] Mo and  $\text{CRSS}_{\epsilon=2.5\%} \propto d^{-0.34}$  for [235] Mo pillars.

A comparison plot is shown in Figure 4.4, where CRSS values from this study and a previous study [143], along with data for Ni and Au [22, 24, 26], have been normalized with resolved

shear modulus and Burgers vector, and plotted together in order to give a better comparison [154]. Resolved shear modulus,  $\mu$ , was derived for imposed strains in  $\langle 111 \rangle \{112\}$  for Mo, and in  $\langle 110 \rangle \{111\}$  for Ni and Au. Using the stiffness constant values in [155] gave values of 158.4 GPa for Mo, 74.6 GPa for Ni, and 23.7 GPa for Au. The resulting size effect slopes for the [001] and [235] Mo pillar data in this study are shallower than those observed in fcc pillar studies which fall in the range from -0.6 to -1.0 [19, 21, 22, 24, 26]. In addition, Mo pillars with diameters in the micron range show yield stresses significantly higher than those of Ni or Au. However, as pillar diameter decreases, the yield stress for the Mo pillars overlaps with that of fcc metals.

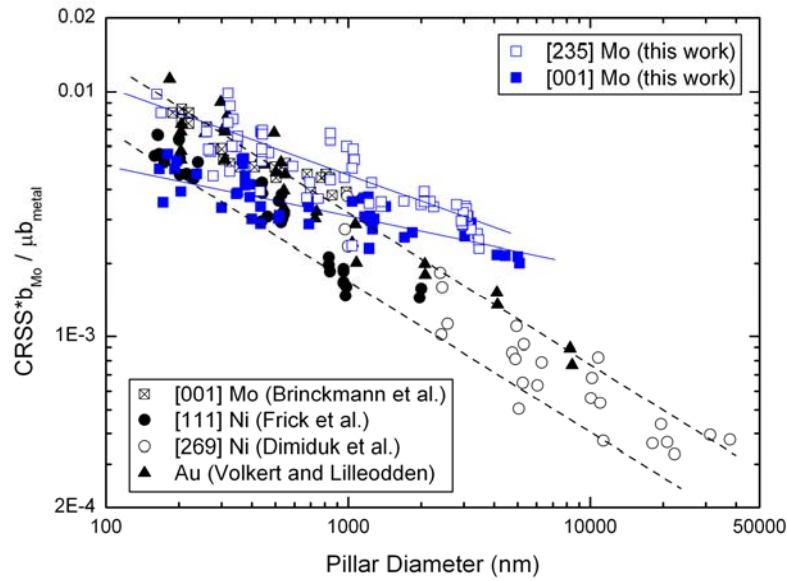


**Figure 4.4:** Comparison plot of CRSS versus diameter showing [001] and [235] Mo pillar data from this work, along with compression data for [001] Mo, [111] Ni, [269] Ni, and low symmetry Au pillars [22, 24, 26, 143]. CRSS values have been normalized with respect to resolved shear modulus and Burgers vector to facilitate direct comparison.

Consistent with the loading rate sensitivity known from bulk compression tests on bcc metals, the yield stresses of the [001] and [235] Mo pillars (taken to be the stress at 2.5% strain) are affected by testing them with different loading rates. Figure 4.5 shows the estimated yield stress as a function of the elastic strain rate for diameters ranging from 370 nm to 3  $\mu\text{m}$ . The elastic strain rate sensitivity, reflected by the slope of the fit lines, varied between 0.07 and 0.1 for all diameters and loading rates tested. This is in close agreement with published data on the strain rate dependence of the yield stress for bulk bcc Mo, which shows a strain rate sensitivity slope of 0.085 [51].

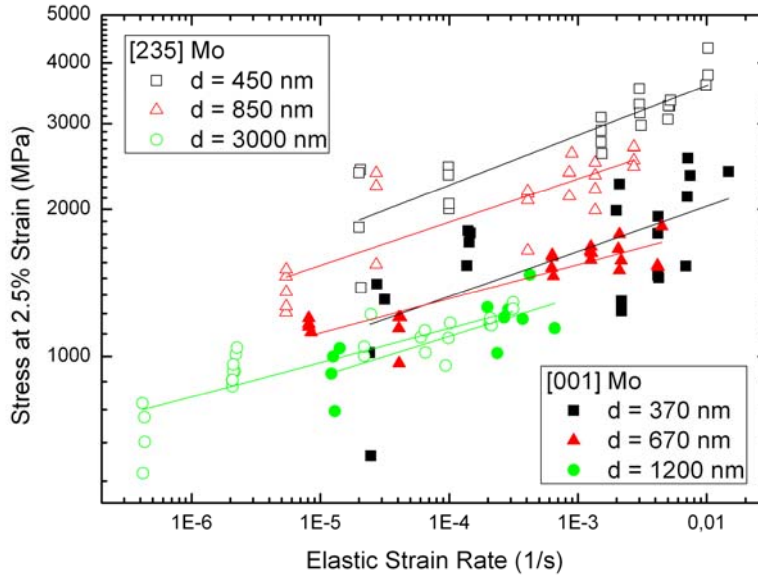


**Figure 4.5:** Compressive stress at 2.5% strain for [001] and [235] Mo pillars over a range of diameters and loading rates, plotted versus elastic strain rate. Slopes from a linear fit of the log-log plot, which are correlated with strain rate sensitivity, were found to be: for [001]: 0.093, 0.070, and 0.081, for 370, 670, and 1200 nm diameters, respectively; for [235]: 0.103, 0.089, and 0.070, for 450, 850, and 3000 nm, respectively.

## 4.5 Discussion

The results of the compression experiments in bcc Mo pillars display key features consistent with previous studies on load-controlled FIB manufactured pillars. The overall shape of the stress-strain curve exhibits displacement bursts, shown in previous studies to be correlated to dislocation motion [125, 156]. Analysis of the statistics of the plastic strain bursts for the [001] and [235] Mo pillars of this study and those of previous fcc pillar studies by Zaiser et al. [145] showed that the distribution of strain bursts for a given diameter was remarkably similar to that of fcc pillars. Furthermore, the stress-strain curves for [001] and [235] Mo pillars transition from smooth, bulk-like flow at larger diameters to a jerky, staircase-like shape for smaller diameters, as shown in Figures 4.1c and 4.2c. At smaller diameters ( $< 1 \mu\text{m}$ ) the staircase-like deformation, i.e. plastic bursts separated by elastic portions of deformation, has been attributed to the activation and subsequent exhaustion of dislocation sources [157]. As pillar diameter is increased, and likewise the sample volume, more sources can be activated within the pillar giving rise to smooth plastic flow as the influence of individual sources is gradually averaged out.

In comparison with fcc pillars, the size effect in bcc Mo is less pronounced. The  $\log(\sigma)$ - $\log(d)$  slopes for the fcc studies are in the range of -0.6 to -1.0, significantly steeper than that observed for Mo; this is shown clearly in Figure 4.4. Keeping in mind the qualitative



similarities between the Mo pillars and fcc pillars (e.g. overall shape of the stress-strain response, statistically similar strain burst behavior, slip traces observed on the sample surface) it is believed that the disparity in the size effect slope stems from the fundamental influence of the bcc crystal structure on dislocation motion. For example, in bcc metals the relatively easy cross-slip of screw dislocations and the different number of preferred glide systems could affect the distribution of source lengths. In addition, the low mobility of screw dislocations resulting from the high Peierls barrier, can greatly influence operation of dislocation sources. Although dislocation sources are initially mixed in character, the disparity in the mobility of pure edge and pure screw segments leads to the creation of long screw dislocations as edge portions move away from the source. As a result, low-mobility screw dislocations begin to pile up in the vicinity of dislocation sources as deformation in bcc metals progresses, as shown in a mesoscopic model by Gröger and Vitek [158]. This is supported by several *in situ* TEM studies, where it has been observed that straight screw dislocations are formed near sources and move slowly as a group [68, 70, 72, 159, 160]. These pile-ups or groups of screw dislocations can apply a back stress on the source, making it increasingly difficult to operate [158]. Due to greater sample volume, the potential size of the pile-up would be increased for increasing pillar diameter, making the influence of this process on the size effect greater for larger pillars than in small pillars. This is consistent with Figure 4.4, where the CRSS values are much greater than for fcc materials at larger diameters, while nearly convergent at smaller diameters.

Another possible explanation is that the dislocation mechanisms in small-scale bcc pillars are fundamentally different than those in fcc pillars, as discussed by Brinckmann et al. [143]. They attributed the size effect in fcc Au pillars to dislocation starvation theory, while in bcc pillars more traditional dislocation-dislocation interactions were believed to influence the deformation behavior. Results from a complementary dislocation dynamics (DD) simulation showed that in bcc pillars dislocations did not exit the pillar at the surface. Instead, they were reflected back into the pillar volume, resulting in further dislocation interactions and giving rise to residual loops and debris in the pillar which facilitated further dislocation multiplication. While this type of mechanism could explain the strain hardening observed for their larger pillars, it does not account for the jerky flow observed for their smaller pillars, or for the similarities in the burst statistics between fcc and bcc [145]. Also of note is that in the current study results show burst behavior at larger diameters than in the Brinckmann et al. study, suggesting that perhaps in the latter case the starting dislocation density was higher.

In addition to an overall difference in slope for the size effects of bcc Mo versus fcc pillars, the slopes of the two different Mo pillar orientations studied were also observed to differ. Data from the [001] Mo pillars showed a less pronounced size effect compared to [235] Mo. This is surprising as similar multiple orientation studies in fcc to date have not shown such a difference. For example, the results of [111] Ni [26] and [269] Ni [22] pillar studies both show a relationship between stress and diameter close to  $\sigma \propto d^{-0.65}$ , although nominal stress values for [111] Ni were slightly lower. Although a difference in initial dislocation density could possibly account for the different slopes, this explanation is unlikely since both the [001] and [235] Mo pillars were cut from the same single crystal. It is possible that in bcc Mo there is greater sensitivity to the number of available glide planes, with [235] being a single slip orientation with limited available slip planes, and [001] being a multiple slip orientation with multiple slip planes available. Intuitively multiple slip planes may facilitate dislocation-dislocation interactions, however, the [001] orientation display lower stresses overall. Ultimately, it is unclear what mechanisms are responsible for the disparity, and further investigation will be required to further characterize this observation.

Lastly, results of loading rate tests on [001] and [235] Mo pillars show that the estimated yield stress (taken to be the stress at 2.5% strain) is strain rate dependent, as is typical for bcc metals and reported for bulk Mo in [51]. Using the following equation [46, 49, 161, 162],

$$v = mkT \left( \frac{\partial \ln \dot{\epsilon}}{\partial \sigma} \right) \quad (4.1)$$

where  $v$  is activation volume for a thermally activated process,  $m$  is a constant taken to be the Taylor factor [50, 51],  $k$  is Boltzmann's constant,  $T$  is temperature,  $\dot{\epsilon}$  is strain rate, and  $\sigma$  is stress, the activation volume for each orientation was calculated. For all pillars tested, the activation volumes were found to be in the range of  $1.3b^3$  to  $5.3b^3$ , where  $b$  is the Burgers vector for Mo ( $2.73\text{\AA}$ ). These values are on the order of bulk bcc values ( $v \cong 10b^3$ ) [46, 64, 161-163], but slightly lower, which may be due to the high stresses attained in the pillars, as well as approximations used to calculate the strain rate and the stress of a pillar. For example, the pillar diameter to calculate stress is taken from the pillar top, which yields minimum values for activation volume. Assuming a linear taper in the pillars, the stress at the center of the pillars was calculated to be 25% less on average. This would accordingly increase the activation volume ( $1.7b^3$  to  $7.0b^3$ ), bringing pillar and bulk values closer together. However, it is believed that using the maximum estimate of the stress is appropriate, because deformation in the pillars had a tendency to initiate in the upper half. The similarity in strain rate

sensitivity and activation volume with respect to bulk indicates that even at these low strain rates and small size scales deformation is within the thermally activated regime. Thus, the same thermally activated processes (e.g. kink-pair nucleation) are likely to control screw dislocation propagation in bcc Mo pillars, even at the micro- and nanoscale.

## 4.6 Conclusions

- Pillars of [001] and [235] bcc Mo were tested in compression, over a range of diameters from ~200 nm up to 5  $\mu\text{m}$ . The general characteristics of the stress-strain curves for Mo pillars were found to be similar to those of fcc. Curves show smooth flow for the largest pillars. Similar burst behavior between bcc Mo and fcc Ni [145] suggests that the underlying dislocation mechanisms at small size scales are also similar.
- For both orientations a size effect was observed, with different slopes:  $\sigma_y \propto d^{-0.22}$  for [001] Mo, and  $\sigma_y \propto d^{-0.34}$  for [235] Mo. The size effect for bcc Mo is smaller than for previous results in fcc single crystals, which fall within the range of  $\sigma \propto d^{-0.6-1.0}$ . Normalized stress values for Mo pillars were found to be substantially higher than for fcc pillars at larger diameters, but similar to fcc at the smallest diameters (~ 200nm).
- Based on the experimental results, it is possible that the low mobility of screw dislocations in the Mo pillars could lead to the formation of pile-ups in the vicinity of dislocation sources [158]. Back stresses on the source from these pile-ups could then hinder their operation. Since at large diameters the pile-ups would involve more dislocations, the influence of the pile-ups would be higher at these diameters and result in larger normalized stress values relative to fcc pillars. However, at smaller diameters the influence would be minimal, resulting in normalized stress values similar to fcc metals.
- For the first time, strain rate sensitivity of bcc Mo pillars was tested by compressing a range of pillar diameters over a range of loading rates. Similar to bulk Mo, [001] and [235] Mo pillars showed a strong dependence on loading rate, demonstrating that the pillar deformation is strain rate sensitive. In addition, calculated activation volumes fell within the range of  $1.3b^3$  to  $5.3b^3$ , which is slightly below bcc bulk values. This suggests that the thermally activated kink pair nucleation required to propagate screw dislocations in bulk Mo may also be dominant at small size scales.

## 4.7 Acknowledgements

The authors would like to thank Arnold Weible and Christof Schwenk for their help in preparing the single crystal Mo. Thanks also to the Berufskolleg für Metallographie at the Max Planck Institute for Metals Research for help with electropolishing, and to Ulrike Eigenthaler for help with the FIB. Finally, many thanks go to Dr. Dieter Brunner for fruitful discussions about bcc metals.

## **5 Correlation Between Critical Temperature and Strength of Small-Scale BCC Pillars**

### **5.1 Abstract**

Microcompression tests were performed on focused ion beam machined micropillars of several body-centered cubic metals (W, Mo, Ta and Nb) at room temperature. The relationship between yield strength and pillar diameter as well as the deformation morphologies were found to correlate with a parameter specific for bcc metals, i.e. the critical temperature  $T_c$ . This finding sheds new light on the phenomenon of small-scale plasticity in largely unexplored non-fcc metals.

## 5.2 Introduction

Recent experiments involving compression of small-scale pillars formed by focused ion beam (FIB) micro-machining have shown that the size dependence of the yield stress differs fundamentally between face-centered cubic (fcc) and body-centered cubic (bcc) metals. In both materials, the yield strength  $\sigma_y$  scales inversely with some power of the pillar diameter  $d$ : in fcc pillars the relationship is  $\sigma_y \propto d^{-0.6}$  to  $d^{-1.0}$  [19, 21, 22, 24, 26], whereas bcc pillars exhibit a less pronounced size effect with  $\sigma_y \propto d^{-0.22}$  to  $d^{-0.45}$  [143, 164]. Various models including size dependent dislocation nucleation [133, 137] and dislocation starvation [127] have been proposed to account for size effects in fcc metals. In bcc metals, dislocation processes differ from those in fcc crystals: dislocation motion occurs on various slip systems with screw dislocations being slower than edge dislocations. The low mobility of screw dislocations is due to their non-planar core structure and the associated need to overcome the Peierls potential by thermal activation [30, 42]. The different size dependence for bcc pillars has been attributed to the low mobility of screw dislocations leading to enhanced dislocation-dislocation interactions [126] or to kinetic pile-ups of screw dislocations in the vicinity of dislocation sources [164].

In this study compression experiments were conducted at room temperature (RT) on bcc metals with different critical temperatures (Table 5.1) to investigate the effect of screw dislocation mobility on the size effect of bcc pillars. The critical temperature ( $T_c$ ) is defined as the temperature at which the flow stress becomes insensitive to the test temperature, i.e. screw and edge dislocations have equal mobility due to thermal activation of the screw dislocations [67]. Below  $T_c$ , screw dislocations are less mobile than edge dislocations and their mobility is a function of test temperature  $T_{\text{test}}$  relative to  $T_c$ .

**Table 5.1:** Critical temperatures of the bcc metals used in this study; data from [57, 63, 65, 67].  $T_{\text{test}} = 298$  K in our experiments.

Material	Nb	Ta	Mo	W
Critical temperature $T_c$ [K]	350	450	480	800
Temperature Ratio $T_{\text{test}}/T_c$	0.85	0.66	0.62	0.37

### 5.3 Experimental Procedure

Tungsten, molybdenum and niobium [001] oriented samples were cut from high purity single crystals grown by the Czochralski method by electron discharge machining. The crystallographic orientation of the samples was determined before cutting by Laue diffraction. Tantalum pillars were cut in [001] oriented grains of a polycrystal after electron backscatter diffraction (EBSD) mapping of the sample surface. For all materials, pillars with diameters ranging from 200 nm to 6  $\mu\text{m}$ , an approximate aspect ratio of 3:1, and taper angles of roughly  $3^\circ$  were machined with a focused ion beam (FIB, Dual Beam<sup>TM</sup> FIB) on the surfaces of the [001] oriented samples. In total, 155 pillars were compressed under load control with a 10  $\mu\text{m}$  sapphire or diamond flat punch using an MTS XP nanoindenter. In order to minimize the effects of variation in strain rate, the load rate was scaled with the cross-sectional area of the pillars resulting in comparable stress rates for all pillars of  $33 \pm 23$  MPa/s. For consistency, the diameter measured at the top of the pillar was used to calculate the engineering stress-strain relationship. A detailed description of fabrication, testing and analysis can be found in [26].

### 5.4 Results

Representative compressive stress-strain curves for [001] oriented W, Mo, Ta, and Nb pillars for various diameters are shown in Figure 5.1. The overall shapes of the stress-strain curves are typical for load-controlled single crystal pillar compression and display the stochastic nature of slip in small dimensions. Strength increases markedly with decreasing diameter. Pillars larger than roughly 2  $\mu\text{m}$  exhibit bulk-like flow [31, 57, 63, 65] with a gradual transition from elastic to plastic deformation and relatively little strain hardening. Pillars with smaller diameters exhibit a staircase-like deformation due to strain bursts associated with individual dislocation events [138]. In general, increasing strain hardening was observed with decreasing diameter, with the exception of large strain bursts in small pillars that led to an apparent strain softening. Increasing strain hardening rates can be explained in terms of kinetic hardening [164]. Although the nominal values for the materials tested are different, the qualitative features of the stress-strain response are consistent with one another, and are similar to observations in fcc single crystalline pillars [24]. The stress-strain response was analyzed in a previous study [145], showing that the distribution of strain bursts in bcc Mo for a given diameter was remarkably similar to that of fcc pillars.

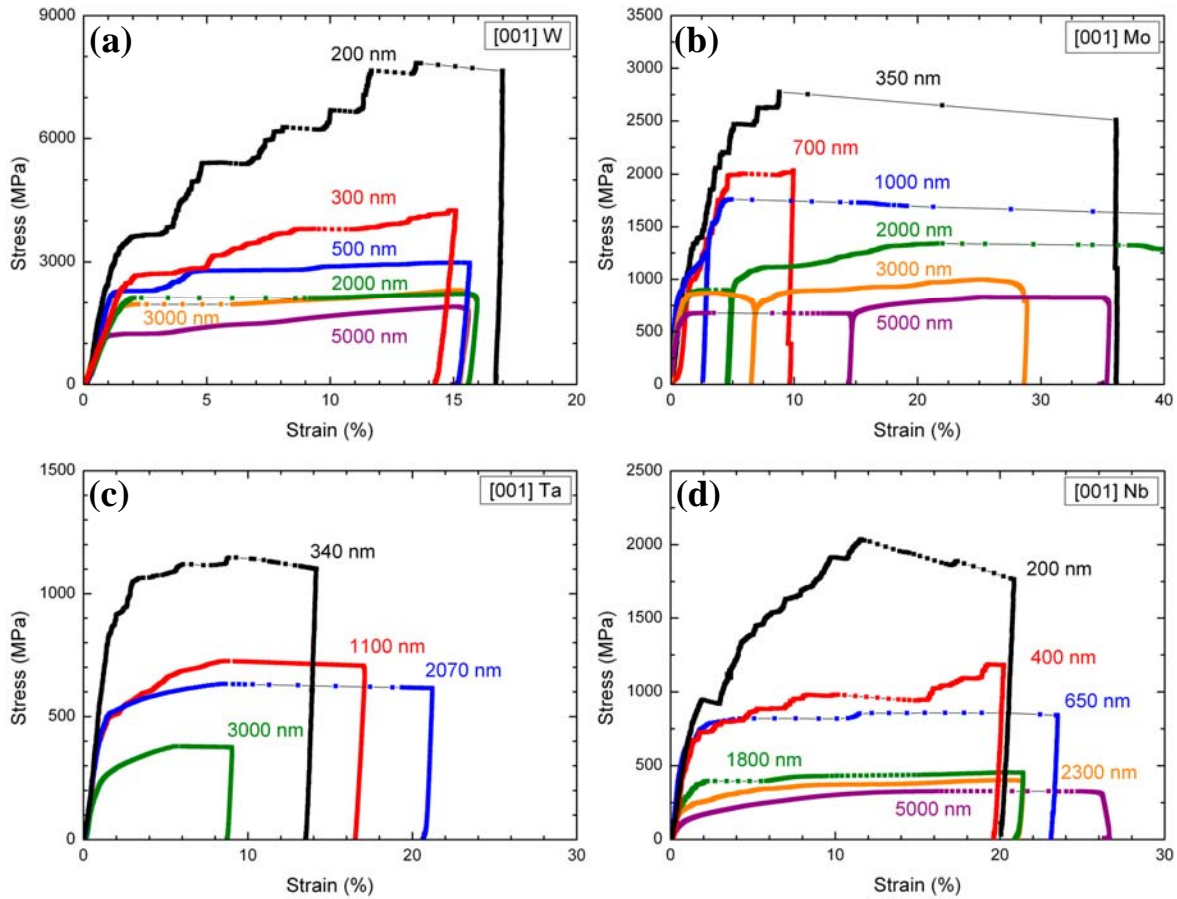


**Figure 5.1:** Representative stress-strain curves for [001] (a) W, (b) Mo, (c) Ta and (d) Nb pillars over a range of diameters from 200 nm to 6  $\mu\text{m}$ . Details about figure (b) can be found in [164].

Figure 5.2 shows representative scanning electron microscope (SEM) images of deformed W and Nb pillars with diameters close to 200 nm (5.2a and b) and 5  $\mu\text{m}$  (5.2c and d). Pictures of Mo [164] and Ta [165] pillars are not shown in the interest of space; however, the deformation morphology of Mo is similar to that of W and the behavior of Ta coincides with that of Nb. All pillars show traces indicative of multiple slip. Pillars with diameters smaller than approximately 1-2  $\mu\text{m}$  exhibited localized slip on a few glide planes, preferentially at the top, as shown in Figs. 5.2a and b. For pillars with larger diameters, two different deformation morphologies were identified. In large W and Mo pillars, there are no continuous slip steps on the pillar surfaces. The slip steps appear wavy throughout the sample, as is typically observed for bulk bcc metals [30, 67]. Wavy slip planes are consistently more difficult to observe in the Ta and Nb pillars, which primarily exhibit localized slip on preferred glide planes with clear slip traces ranging across the pillar surface. The deformation morphology for Nb is in agreement with experimental findings by Kim et al. [166].



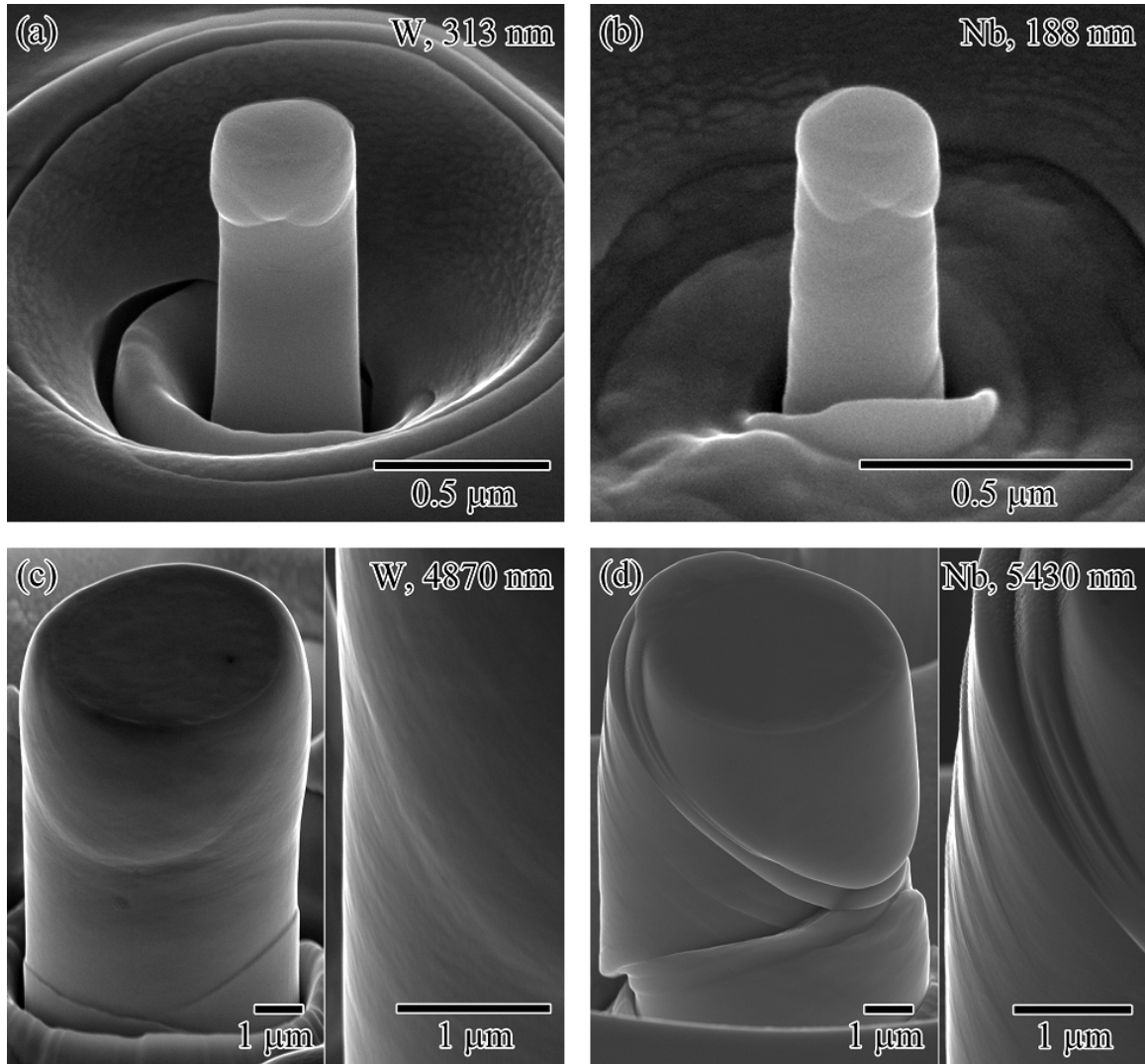


**Figure 5.2:** Post-compression SEM images of representative [001] oriented Nb and W pillars: (a) 313 nm W, (b) 188 nm Nb, (c) 4870 nm W, and (d) 5430 nm Nb pillars. Higher magnification insets in (c) and (d) highlight differences in slip trace morphologies between W and Nb. In all cases, slip traces on the pillar surfaces indicate multiple slip.

The mechanical size effect of different bcc pillars is shown in Fig. 5.3a, which illustrates the stress at 5% strain as a function of diameter. The data for Mo from a recent study by Brinckmann et al. [143] is consistent with the presented Mo data, as shown in [164]. For comparison, typical fcc data from Au pillars with low symmetry compression axes [24] was added. The strengths of the bcc metals are higher than those of Au and the relative differences in strength between the different materials decrease with decreasing pillar size. Comparing W and Nb, the strengths differ by a factor of 5.5 at 5  $\mu\text{m}$  (1410 MPa vs. 257 MPa) and only differ by a factor of 2.2 at 200 nm (2800 MPa vs. 1275 MPa). The order of the strength of the bcc pillars correlates with the critical temperature of the individual material. Using a power law fit, slopes of -0.21, -0.38, -0.41 and -0.48 are obtained for W, Mo, Ta and Nb pillars, respectively. The slope for the Nb pillars is significantly smaller than recently observed by Kim et al. [166]. This difference is most likely a reflection of the stochastic nature of the

stress-strain response of small-scale pillars in combination with the limited number of tests performed in the study by Kim et al. [166]. By comparing the slopes of the current study with the critical temperatures given in Table 5.1, it can be seen that the higher the critical temperature, the weaker the size dependence. It is important to note that this trend is independent of the strain value at which the stresses are measured or of specific normalization conditions [165]. In Fig. 5.3b the power law exponent is plotted as a function of test temperature divided by  $T_c$ , to examine the role of screw dislocation mobility on the size dependence. The ratio of  $T_{\text{test}}$  to  $T_c$  is a measure for the thermal activation of the screw dislocations: a larger ratio means higher thermal activation and therefore higher mobility of the screw dislocations. The data points in Fig. 5.3b follow roughly a linear relationship. The extrapolation of the line of best fit to lower critical temperatures yields an exponent of about -0.6 (represented by the horizontal line in Fig. 5.3b) for  $T_c = T_{\text{test}}$ , which corresponds to the condition where screw and edge dislocations have equal mobility. This value is in agreement with exponents found for fcc metal pillars [22, 24] where screw and edge dislocations have the same mobility at room temperature.

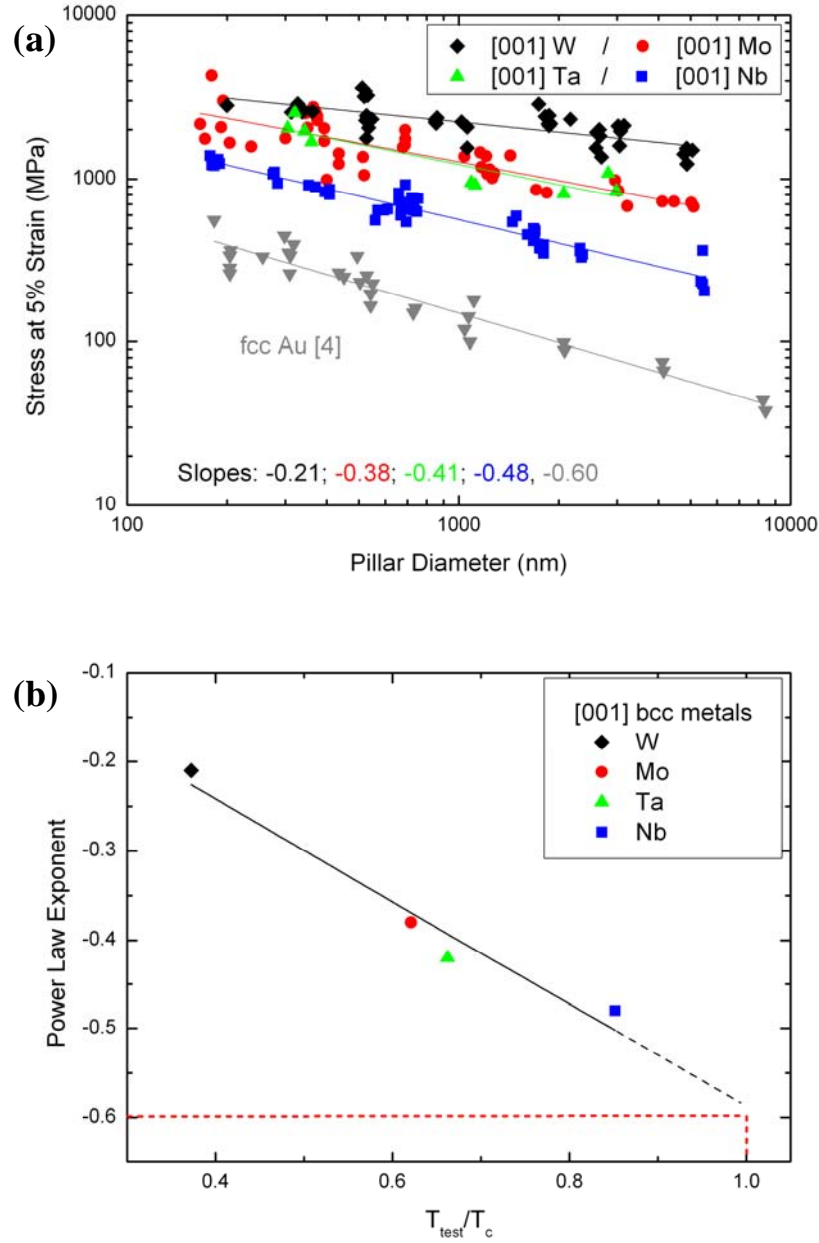


**Figure 5.3:** Comparison plots: (a) of stress measured at 5% strain versus pillar top diameter for all [001] bcc pillars tested (i.e. W, Mo, Ta, and Nb) as well as [001] Au pillar data [24], (b) slope of the line of best fit (exponent) for the size dependence of the bcc metals shown in (a) versus normalized test temperature  $T_{\text{test}}/T_c$  (see Text and Table 5.1).

## 5.5 Discussion

The results presented here show that deformation mechanisms in small-scale bcc metals depend on size as well as on critical temperature. All materials tested show an increase in strength with decreasing pillar diameter, indicating that confinement of dislocation processes starts to dominate the deformation; this leads to a transition from continuous, bulk-like to jerky, staircase-like stress-strain behavior and a significant change in the deformation morphology between small and large pillars. The critical temperature of the bcc metals was

found to have a strong influence on the deformation morphology of the large pillars. Large pillars with low  $T_c$  (Ta, Nb) showed localized slip, whereas metals with higher  $T_c$  (Mo, W) show wavy slip as is typically observed for bulk bcc metals (Fig. 5.2c and 5.2d). In general, the deformation of bcc metals is controlled by the motion of long and straight screw dislocations [30]. Their ability to cross-slip between crystallographic planes which intersect along the  $\langle 111 \rangle$  direction leads to wavy slip steps. The cross-slip of screw dislocations may account for the deformation morphology of the large W and Mo pillars. The well-resolved slip steps of Nb and Ta indicate that less cross slip occurred during deformation. For metals with low  $T_c$  (Nb, Ta) the dislocations may bow out and deviate from pure screw character over considerable length of the pillar. As dislocations of mixed character are confined to specific glide planes, this may lead to localized slip. For small pillars no influence of the critical temperature on deformation morphology was found. One explanation is that the periodicity of wavy slip is on the order of the pillar diameter and hence not observable at this size scale. Another possible explanation is that for the smallest pillars dislocation nucleation is controlling the deformation instead of dislocation propagation. Immediately after nucleation, dislocations are highly curved and therefore of mixed character, explaining the localized deformation of the smallest pillars (Fig. 5.2a and 5.2b). This indicates that thermally activated screw dislocation motion and related processes are not prevalent in very small bcc pillars. However, in a previous study on Mo pillars [164] it was shown that the strain rate dependence of the yield strength does not depend on pillar diameter and that it is comparable to values obtained from bulk materials. This suggests that on the one hand athermal dislocation nucleation controls the deformation at small size scales but a thermal component still exists. This is in contrast to nanocrystalline bcc metals, where it was found that the strain rate sensitivity decreases with decreasing grain size [161]. This indicates that at small scale the interaction of dislocations with interfaces becomes dominant rather than screw dislocation motion as such.

Besides the deformation morphologies, the strength values and their size dependence were also found to correlate with  $T_c$  (Fig. 5.3). A general correlation of the strength values with  $T_c$  is not surprising as the strength of bcc bulk metals at temperatures below  $T_c$  is related to the low mobility of screw dislocations. As  $T_c$  increases from Nb to W, the mobility of screw dislocations decreases because thermal energy becomes small relative to the height of the Peierls potential, resulting in high stresses for materials with a high  $T_c$ . The correlation between size dependence and  $T_c$  suggests that the mobility of screw dislocations affects the size scaling: (i) From Fig. 5.3a it can be seen that for the pillars with the smallest diameters,

the relative differences in strength between the different materials are smallest, suggesting that the relative contribution of the Peierls mechanism on the overall strength decreases for decreasing sample size. (ii) As can be seen in Fig. 5.3b, the power law exponent scales with the inverse of the critical temperature. It seems that for temperatures close to  $T_c$ , where the influence of the low mobility of screw dislocations becomes negligible, the behavior of bcc also approaches that of fcc metals. The similar behavior of fcc and bcc pillars for small diameters and for test temperatures near  $T_c$  indicates that under conditions where screw dislocation motion is not the limiting mechanism, the strength of bcc and fcc pillars may be controlled by the same dislocation processes. With increasing sample size and increasing critical temperature an increasing effect of screw dislocation mobility becomes apparent, leading to a deviation from fcc behavior that scales with  $T_{\text{test}}/T_c$ .

One concept that can account for observations (i) and (ii) is based on kink nucleation at the sample surface [144, 165]. Kinks can easily nucleate at the sample surface and can enhance screw dislocation mobility. Since the surface to volume ratio increases with decreasing sample size, kink nucleation becomes more likely and the mobility of screw dislocations may increase, possibly reaching the mobility of edge dislocations for the smallest samples. Another mechanism that can account for both observations (i) and (ii) is the kinetic pile-up of screw dislocations in front of dislocation sources [158, 164] which exert a back stress on the source. In smaller bcc pillars only small pile-ups can form and less back stress is exerted on the dislocation source so that the activation stress is more or less determined by the line tension of the emitted dislocation. The influence of both mechanisms depends on the mobility of screw dislocations indicating that the critical temperature appears as an additional parameter influencing the deformation behavior of bcc metals in small dimensions.

## 5.6 Conclusions

- Microcompression tests were performed on [001] oriented W, Mo, Ta and Nb micro- and nanopillars. Independent of the material, the stress-strain curves of the large pillars are continuous, whereas those of the smaller pillars ( $< 1\text{-}2\ \mu\text{m}$ ) show strain bursts separated by elastic loading segments.
- The deformation morphology of the bcc pillars was found to be dependent on pillar diameter and critical temperature of the metal. For pillars with diameters larger than approximately  $1\text{-}2\ \mu\text{m}$  diameters, two different deformation morphologies were identified:

Similar to bulk, the W and Mo pillars demonstrate wavy slip lines, which can be correlated to the cross-slip of screw dislocations. In contrast, the glide steps of the Ta and Nb pillars are well resolved on single crystallographic planes indicating that the propensity for cross-slip is reduced compared to bulk. For smaller diameters, the deformation morphology is similar for the different materials suggesting that screw dislocation motion is less dominant at this size.

- [001] W, Mo, Ta and Nb pillars show a strong increase in yield strength with decreasing pillar diameter. The absolute values of the yield strength and the relationship between yield strength and pillar diameter were found to scale with  $T_{\text{test}}/T_c$ . This suggests that the mobility of the screw dislocations controls the size effect of bcc pillars. Further, the convergence of the yield stress values for small pillar diameters and the scaling of the size dependence with  $T_{\text{test}}/T_c$  indicate that the effect of the screw dislocations is small for materials with a low  $T_c$  and for small pillar diameters.
- The results demonstrate that for large pillar diameters, the low mobility of the screw dislocations inherent to the bcc structure leads to elevated yield stresses compared to fcc pillars. However, for small pillars kink-nucleation at the surface or the limited space for the formation of kinetic pile-ups of screw dislocations could explain the decreasing influence of the screw dislocations with decreasing pillar diameter. For materials with a low critical temperature, the screw dislocations motion is less relevant and therefore fcc and bcc pillars show a similar behavior.

## 5.7 Acknowledgements

The authors would like to thank Arnold Weible and Christof Schwenk for sample preparation and Dan Gianola for fruitful discussions. BGC thanks the Alexander von Humboldt-Foundation for financial support. DK, RM and OK acknowledge support by the European Union through the NANOMESO project.

## **6 Effect of Pre-straining on the Size Effect in Molybdenum Pillars**

### **6.1 Abstract**

The effect of prior deformation on mechanical behavior as a function of size is investigated for body-centered cubic (bcc) molybdenum (Mo) pillars. Experiments were performed using focus ion beam (FIB) manufactured [001] and [235] Mo micro/nanopillars, which were compressed, re-FIB machined, and compressed again. Unlike bulk materials, pre-straining has a negligible effect on stress-strain behavior of the pillars, suggesting that dislocation storage does not occur in small-scale bcc specimens. The prevailing mechanism behind the size effect is attributed to dislocation nucleation mechanisms.

## 6.2 Introduction

Micron and sub-micron pillar compression experiments have provided significant insight into the mechanisms responsible for size dependent deformation behavior [167]. Experiments with focus ion beam (FIB) machined pillars of face-centered cubic (fcc) metals have consistently shown an increase in strength with decreasing diameter; flow stresses  $\sigma_y$  were generally found to scale with an inverse power of specimen diameter  $d$ :  $\sigma_y \propto d^{-n}$  with  $n \approx 0.6$  [123, 124]. Several analytical models [127, 137, 168], and dislocation dynamics (DD) simulations [129, 130, 141, 169] have been developed to help explain this size effect. The models vary significantly, but all assume that the proximity of a free surface fundamentally influences dislocation processes relative to bulk material. Usually, the size dependent yield stress is found to depend on the ratio of source size to pillar diameter [29]. Intermittent plastic flow as well as increasing strain hardening rates for decreasing pillar diameters are reported and explained in terms of source exhaustion [123].

In contrast to the majority of pillar studies on fcc metals, pillars cut from body-centered cubic (bcc) molybdenum (Mo) have exhibited a less pronounced size effect, with  $n$  between 0.21 and 0.48 [143, 164, 170]. The dislocation processes inherent to the bcc crystal structure fundamentally differ from those in fcc metals: In bulk bcc metals the flow stress is controlled by the stress-assisted, thermally-activated motion of screw dislocations. This is a consequence of the three-dimensional core structure of  $a/2 \langle 111 \rangle$  screw dislocations leading to a particularly high Peierls potential [31, 90]. Based on DD simulations, Greer et al. argued that the size dependence disparity between the bcc Mo and fcc pillars is due to a principally different effect, i.e. the long lifetime of screw dislocations in bcc pillars, leading to junction formation and conventional strain-hardening [126]. This would suggest that for bcc pillars, dislocation storage plays a significant role in size dependent dislocation processes. However, experiments on bcc micropillars cut in proximity to nanoindenters did not reveal an increase in strength, despite the increased dislocation density [146].

An alternate explanation for the different scaling behavior of fcc and bcc pillars was recently suggested by the present authors [164, 170]. Based on the observations that load-controlled compression of both fcc and bcc pillars exhibit similar strain burst behavior [145], as well as similar yield stress values at diameters of approximately 200 nm [170], it was suggested that the mechanisms related to size-dependent dislocation behavior are similar in both crystal structures. The discrepancy in the exponent  $n$  was attributed to the high Peierls potential which causes a high “background” stress for the size effect in bcc structures. Recent testing of



several bcc metals suggested that the value of  $n$  was directly linked to screw dislocation mobility at the test temperature [170].

### 6.3 Motivation and Experimental Procedure

In order to discriminate between the two paths of explanation, this study reports on compression tests of pre-strained Mo pillars. Crystallographic orientations of high and low symmetry ([001] and [235], respectively) were chosen to gauge the behavior for different slip systems. In total, 57 columnar pillars with diameters between 300 and 3000 nm were pre-compressed to strains ranging from 10 to nearly 40% in a previous study [164]. The deformation was introduced under load control using an MTS nanoindenter equipped with a diamond or sapphire flat punch of 10  $\mu\text{m}$  diameter. The deformed pillars were now re-cut using the FIB to again obtain a cylindrical shape while removing all prior surface steps. The amount of material removed during re-cutting depended on the original pillar diameter and the extent of pre-deformation. Care was taken to maintain a comparable height-to-diameter ratio and similar taper angles for corresponding original and pre-strained pillars. Table 1 lists the average percentage of diameter reduction and height-to-diameter ratio for several ranges of pre-straining. Re-cut, pre-strained FIB pillars were then compressed a second time to approximately 10% additional strain. Calculations of engineering stress-strain data was done as reported by Frick et al. [26], where the pillar top diameter was used for a maximum stress estimate.

**Table 6.1:** Average percentage of diameter reduction ( $\pm$  one standard deviation) and height-to-diameter aspect ratio for Mo pillars

Pre-straining [%]	Average diameter Decrease [%]		Aspect Ratio			
			Original Pillars		Pre-strained pillars	
	[001]	[235]	[001]	[235]	[001]	[235]
10-15	$13 \pm 5$	$9 \pm 7$	3.1	3.6	3.5	4.4
15-20	$16 \pm 6$	$10 \pm 5$	3.4	3.3	3.5	3.3
20-30	$15 \pm 8$	$19 \pm 11$	2.2	3.2	2.8	3.5
> 30	$23 \pm 8$	$35 \pm 17$	2.1	2.5	2.7	3.3

## 6.4 Results

Scanning electron microscope (SEM) images shown in Figure 6.1 illustrate the various stages of testing for two representative pillars. The pillar shown in Figures 6.1a is of [001] oriented Mo with an original diameter of 3200 nm that had been deformed to 40% strain. This pillar was then subsequently re-FIB machined to a diameter of 2660 nm, and re-compressed to approximately 10 % strain. The second pillar, shown in Figure 6.1b is also [001] Mo and follows the same sequence. In that case, the original 370 nm pillar had been deformed to 16%, re-FIB machined to a diameter of 300 nm and further compressed about 10%. These examples were chosen because they represent the extremes in pillar size and original strain magnitudes. Multiple dislocation slip systems are observed on the sample surface for the [001] oriented pillars, whereas the favorably oriented single slip system was consistently observed for the [235] oriented pillars [164]. This observation is consistent with the number of favorable slip planes available for each orientation. The deformation of the pre-strained pillars generally occurred in the same fashion and in the same location where it had appeared on the original pillars. Barreling, which was frequently observed in larger pillars with [001] orientation, re-appeared during the second deformation.

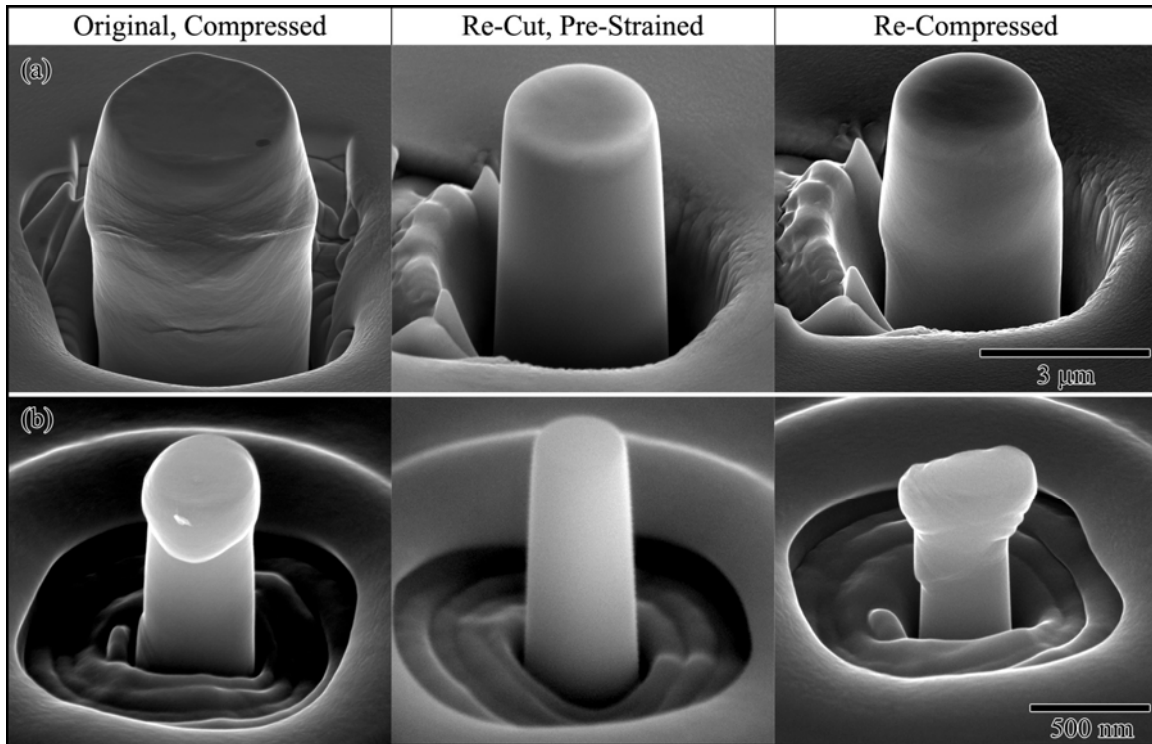


**Figure 6.1:** SEM images illustrating the testing sequence for two [001] Mo pillars: compressed, original pillars from previous study [164], pre-strained pillars re-cut using the FIB, and re-cut, pre-strained pillars that have been re-compressed. For the pillar in sequence (a), original pillar diameter was 3220 nm and re-cut, pre-strained diameter was 2660 nm. For the pillar in sequence (b), original pillar diameter was 370 nm and re-cut, pre-strained diameter was 300 nm.

Corresponding stress-strain curves for representative [001] and [235] oriented Mo pillars during first (original pillar) and second deformation (pre-strained pillar) are illustrated in Figure 2. For comparison, Figures 2b and d also show representative curves with intermediate elastic unloading and reloading (gray) taken from Ref. [164]; however, these tests were not used for the pre-straining experiments. All Mo pillars tested demonstrate the key features typical of load controlled pillar compression [145, 164]: Frequent plastic strain bursts separated by regions of nearly elastic loading were observed, except for the coarsest pillars.

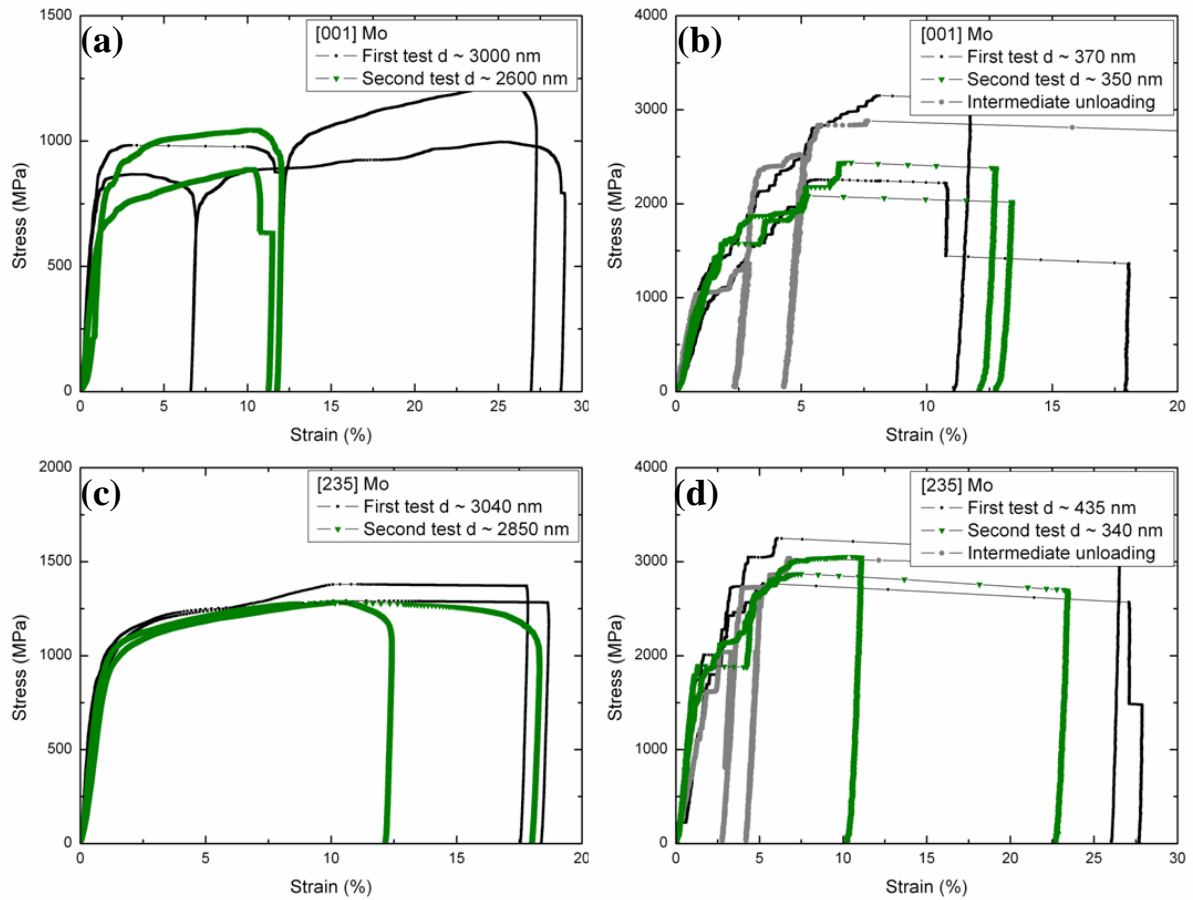


**Figure 6.2:** Stress-strain response during the first and second deformation for representative Mo pillars, (a) and (b): [001] orientation, initial diameters about 3000 and 350 nm. (c) and (d): [235] orientation, initial diameters of about 3000 nm and 400 nm. Also shown in (b) and (d) are representative curves with intermediate elastic unloading and reloading (gray) taken from Ref. [164].

Additionally, flow stress as well as apparent hardening rate was found to increase with decreasing pillar diameter. Comparison of the stress-strain response of original and pre-strained Mo pillars shows that qualitatively the strain burst behavior is not affected by the pre-straining. Surprisingly, the yield stress of the pre-strained pillars, with reduced diameters, is well *below* the maximum stress achieved during the deformation of the original pillars. Conversely, for specimens where intermediate unloading and reloading were performed

without re-machining, the hardening experienced during the initial loading tends to be “remembered” upon reloading.

In order to quantify the effect of pre-straining on plastic strength, Figure 3 illustrates the relationship between the stress measured at 2.5% strain and pillar diameter for corresponding original and pre-strained [001] and [235] Mo pillars. This stress value is an estimate of yield strength; it is insensitive to surface roughness and misalignment, which can lower the initial loading stiffness [24]. It is seen that pre-straining does not systematically influence the yield strength. Additionally, yield stress of the pre-strained pillars shows no relationship with respect to the magnitude of the stress-strain values sustained by corresponding original pillars.

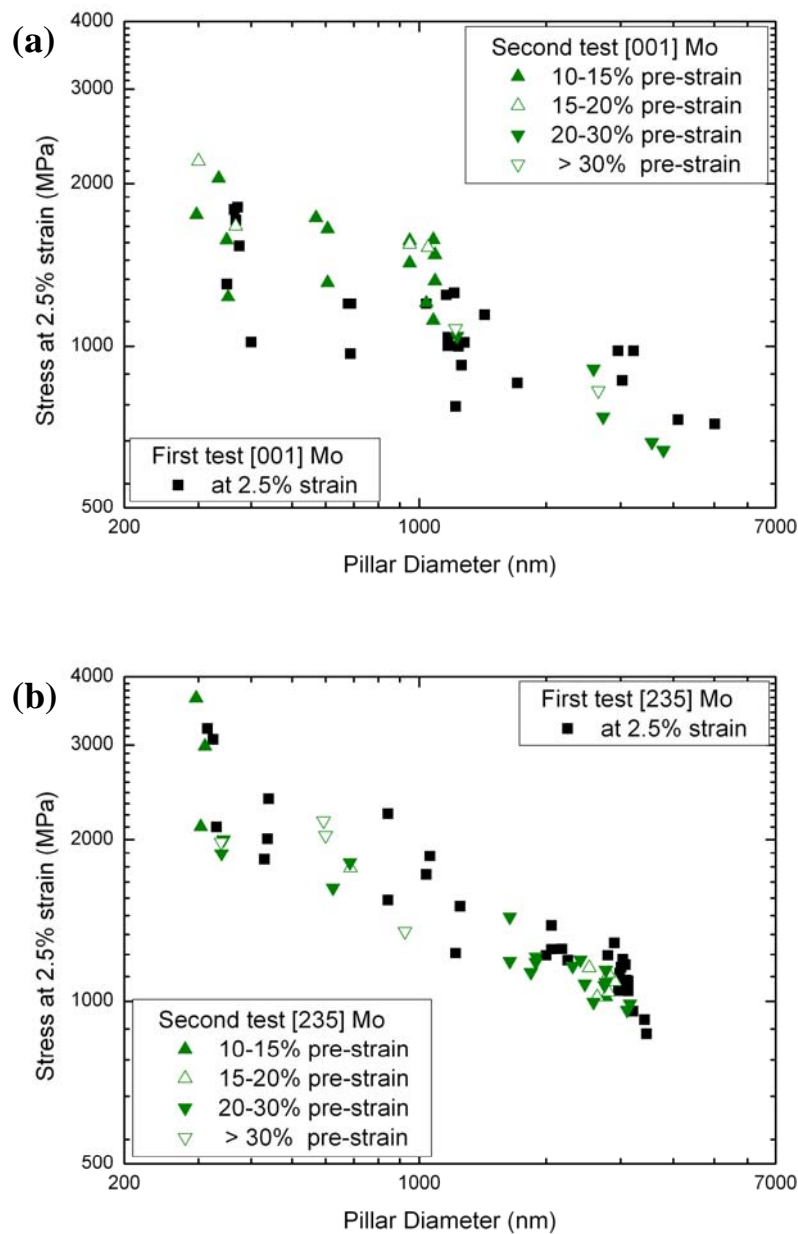


**Figure 6.3:** Stress at 2.5% plastic strain vs. pillar diameter for original and pre-strained Mo pillars with (a) [001] and (b) [235] orientation. Magnitude of pre-straining ranged from 10% to over 30% strain.

In the case of bulk metals, pre-straining would cause an increase in strength due to dislocation storage and subsequent dislocation-dislocation interactions [171]. Bulk strain hardening behavior in bcc metals is known to correlate with the deformation temperature: at low temperature the effect of strain hardening is usually small compared to the low mobility of screw dislocations [31]. However, the bcc Mo pillars show significant hardening in the stress-strain response, which increases with decreasing diameter. This is quantified in Figure 6.4, which shows the strain hardening rate (SHR) of the original and pre-strained pillars versus diameter. Due to the burst behavior of the smaller pillars, the SHR is defined as the slope between 2.5 and 10% strain, consistent with previous fcc small-scale pillar studies [24, 26]. The SHR as a function of diameter is not related to deformation history. Larger pillars of both states show SHRs close to the bulk value that was calculated based on typical shear stress/strain hardening rates of bcc metals [90]. Below approximately 1.5  $\mu\text{m}$  in diameter, the SHR begins to dramatically increase to values several times larger than for bulk Mo. Furthermore, despite the additional slip systems available in the [001] orientation, and thus the potential for more dislocation interactions, nominal SHRs for both orientations are similar.

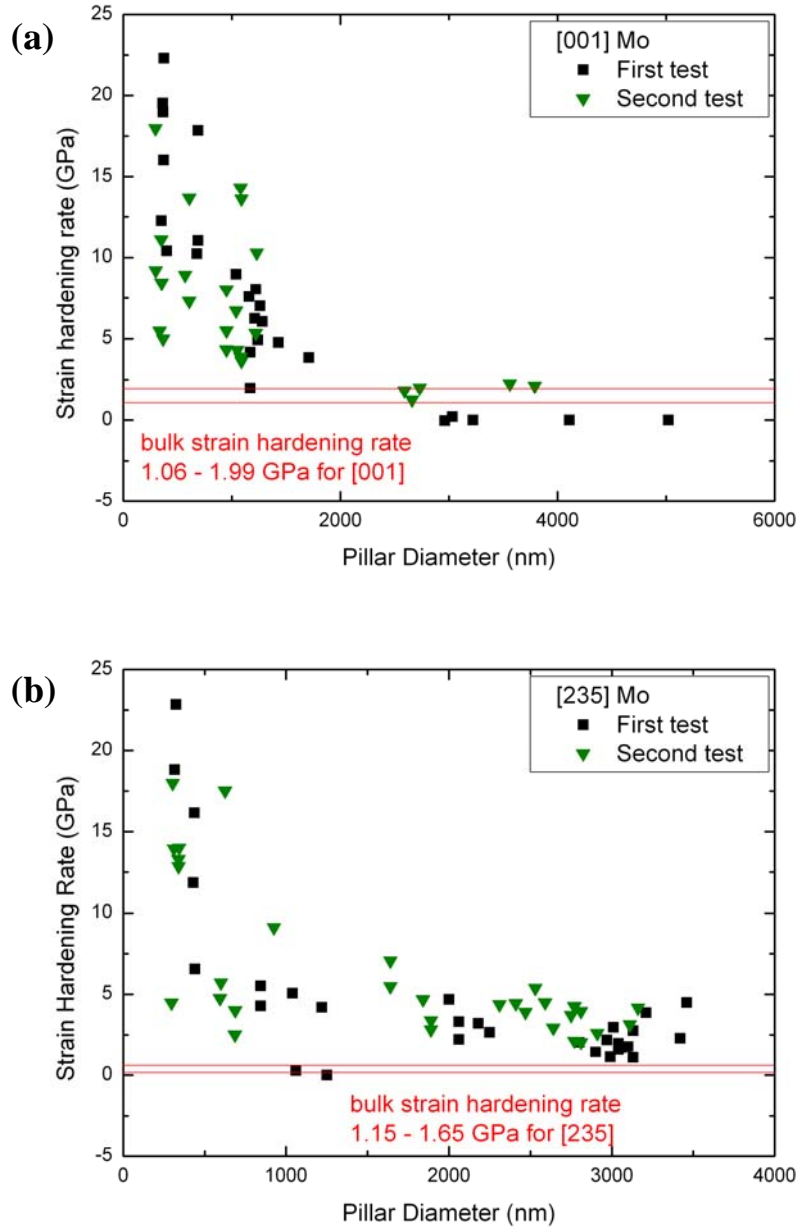


**Figure 6.4:** Strain hardening rate (SHR) versus pillar diameter for original and pre-strained Mo pillars with (a) [001] and (b) [235] orientation.

## 6.5 Discussion

Overall, the results show that the mechanical properties of the tested Mo pillars are not considerably affected by pre-straining, although significant strain hardening is observed in the stress-strain response of the original pillars. Since the achieved hardening is “remembered” during intermediate unloading and reloading in a single test, it must be concluded that re-cutting with the FIB essentially “resets” the stress-strain response of the pre-strained pillars. Therefore it is highly unlikely that the strain hardening is related to traditional work hardening, i.e. dislocation-dislocation interactions.

We propose, instead, that for the Mo pillars, as compression progresses, the dislocation sources become exhausted and activation of less favorable sources leads to strain hardening. This conclusion is consistent with recent fcc pillar experimental studies where emphasis has been placed on understanding the nature of dislocation nucleation and dislocation storage in pillars. For example, *in situ* transmission electron microscopy (TEM) experiments of [111] Ni showed dislocations quickly exited the 150-300 nm diameter pillars upon loading [125]. The underlying physical mechanism was explained as a competition between dislocation activation/nucleation rate and the rate at which dislocations leave the pillar, leading to a progressive exhaustion of dislocation sources and therefore a hardening response during the compression test. By extension, the results shown in this study clearly demonstrate that the dislocation sources come primarily from the FIB, and the propensity for dislocation storage does little to influence the mechanical strength. Therefore, new dislocation sources, which can be introduced into the material by subsequent FIB cutting [149], control the yield strength as well as the hardening of the pre-strained pillars.

It has to be emphasized that the insensitivity of the yield stresses to pre-straining differs from the results of Bei et al. [120], who found Mo alloy pillars, produced via directional solidification and etching, to be significantly weaker after pre-straining. This discrepancy may be due to the fact that such pillars, being initially defect-free, will behave in a whisker-like manner during initial deformation [118]: at first dislocations have to be nucleated in a perfect crystal, which requires stresses close to the theoretical limit; once deformed, residual defects act as nucleation sources, effectively lowering the yield strength. Similar behavior is observed for these directionally solidified Mo-alloy pillars post FIB milling [149]. FIB cutting is well known to create a  $\text{Ga}^+$ -ion implanted amorphous damage layer several nanometers in depth [26, 148]. It is believed that the defects introduced by FIB milling, similar to the defects created by pre-straining, act as dislocation sources of the initially defect-free Mo-alloy pillars, also lowering the material strength [149]. The FIB manufactured pillars used in this study were machined from a single crystal grown via the Czochralski method, which does not yield an initially dislocation free sample. Our results show that the yield stress of original and pre-strained pillars for any given diameter are very similar, which suggests that the defects created during FIB manufacturing serve as the primary source for mobile dislocations. Additionally, because the magnitude of prior deformation exhibits no influence on the yield strength, it is unlikely that dislocation storage is a predominant mechanism in bcc micron-scale pillar deformation.

## 6.6 Conclusions

- Microcompression tests were performed on [001] and [235] oriented Mo pillars, which had been pre-deformed to strains ranging from 10 to 40% and subsequently re-machined with the FIB. It was observed that the deformation of the pre-strained pillars occurs in the same fashion and in the same location where it appeared on the original pillars.
- Similar to the original pillars, the stress-strain curves of the pre-strained pillars exhibit the key features typical for load-controlled pillar compression: The frequency of the strain bursts, the yield strength and the strain hardening rate increase with decreasing pillar diameter.
- Although significant strain hardening was observed for the original pillars, the yield strength and the strain hardening rate of the pre-strained pillars show no relationship with respect to the magnitude of stress-strain values sustained by the corresponding original pillars. In contrast, for samples, where the intermediate unloading and reloading was performed without re-machining the pillars, the hardening experienced during the initial loading is remembered upon reloading.
- Based on the experimental results, it is evident that pre-straining does not lead to a significant increase in the dislocation density, because this should result in a hardening, which is relevant for the deformation of the pre-strained pillars. Further, the reset of the mechanical properties after re-cutting the pillars with the FIB demonstrates that the deformation of the Mo pillars is source controlled. The activation and exhaustion of dislocation sources can cause an apparent hardening; however, defects introduced in the material by the FIB can serve as potential dislocation sources. These sources may control the properties of the pre-strained pillars.



## **7 Influence of Orientation on the Size Effect in BCC Pillars with Different Critical Temperature**

### **7.1 Abstract**

The size effect in body-centered cubic (bcc) metals is comprehensively investigated through microcompression tests performed on focused ion beam machined tungsten (W), molybdenum (Mo) and niobium (Nb) pillars, with single slip  $[235]$  and multiple slip  $[001]$  orientations. The results demonstrate that the stress-strain response is not affected by the number of activated slip systems, indicating that dislocation-dislocation interaction is not a dominant mechanism for the observed diameter dependent yield strength and strain hardening. Furthermore, the limited mobility of screw dislocations, which scale differently for each material, act as an additional strengthening mechanism leading to a material dependent size effect. Nominal values and the scaling of the flow stress significantly deviate from that observed for face-centered cubic (fcc) metals. This is demonstrated by the correlation of size dependence and material specific critical temperature.

## 7.2 Introduction

Small-scale compression tests on focused ion beam (FIB) machined, single crystalline metal pillars have consistently shown that the flow stress scales with the pillar diameter [29, 123]. Theoretical [127, 137] and simulation [129, 130, 141] work has been performed to understand this size effect in the absence of strain gradients and hard interfaces. It has been demonstrated that dislocation processes involved in small-scale deformation deviate from those in bulk material. Dislocation multiplication and related forest hardening, which play a dominant role in the flow stress of fcc bulk metals, become increasingly less significant as the sample size decreases [167]. This is due to the fact that for sample size smaller than a few micrometers the critical length for dislocation multiplication is larger than the sample size [172], as e.g. dislocations may annihilate at the free surface before conventional dislocation multiplication can occur [127, 128]. If the crystal is starved of mobile dislocations, the nucleation of new dislocations is necessary for deformation. Further, it was demonstrated in simulations [129, 173] and recent *in situ* TEM compression tests on submicrometer [111] Ni pillars [125] that source exhaustion in sub-micrometer sized pillars can cause intermittent plastic flow as well as high strain hardening rates.

Experiments on bcc and fcc pillars have shown a different size scaling. Relative to fcc single crystal metals, bcc metals exhibit a weaker size dependence [126, 143, 164, 170]. Recent dislocation and molecular dynamics DD/MD [126, 144] simulations suggested that dislocations have a longer residence time in bcc pillars, and that a single dislocation typically multiplies before leaving the pillar. Experimental studies demonstrated an increase in dislocation density subsequent to deformation for a 100 nm diameter Nb pillar [166], and that normalized strength values are significantly higher for bcc pillars compared to fcc pillars [126, 143]. Based on these observations, it was concluded that the size effect of bcc metals is controlled by dislocation-dislocation interactions [126]. However, this mechanism is inconsistent with our recent results on Mo pillars (chapter 6, [174]): These experiments demonstrated no observable difference in strength or strain hardening behavior between pre-strained and original pillars indicating that dislocation accumulation is not a prevalent mechanism in bcc pillar deformation.

In recent comprehensive experiments on W, Mo, Ta and Nb pillars it was found that the size dependence of these bcc pillars correlated with the ratio of test temperature  $T_{test}$  to the critical temperature  $T_c$  (chapter 5, [170]). The critical temperature represents the temperature above which the flow stress becomes insensitive to temperature and strain rate [31]. Below this

temperature, screw dislocations are less mobile than edge dislocations, and their motion is controlled by thermally activated nucleation of kink-pairs [42]. Above  $T_c$ , screw and edge dislocations have the same mobility due to sufficient thermal activation. The critical temperature is highly dependent on atomic structure and bond strength, and therefore varies substantially for the particular metal [31]. This has been explained by the high Peierls potential inherent to the bcc structure, which is caused by the three-fold symmetry of the core of screw dislocation [30, 32]. Size dependent pillar testing conducted at room temperature for the above mentioned bcc metals revealed that materials with a small ratio of  $T_{test}/T_c$  showed weak size dependence, whereas materials with a large ratio of  $T_{test}/T_c$  exhibited size dependence close to the ones observed for fcc pillars [170]. Since the ratio of  $T_{test}/T_c$  is a measure for the mobility of screw dislocations, it was concluded that the screw dislocation mobility is an additional parameter influencing the small-scale deformation of bcc metals. Additionally, the size dependence of bcc metals was found to approach that of fcc metals for  $T_{test}/T_c$  equal to one. Thus, it can be further assumed that for equal mobility of edge and screw dislocations the size effect in fcc and bcc pillars may be attributed to the same dislocation processes.

The effect of orientation on the behavior of bcc metal pillars is not well understood. Only one study has systematically investigated the size dependence of Mo pillars oriented for single slip and multiple slip [164]. It was shown that in Mo single slip led to a stronger size dependence than multiple slip. This behavior is inconsistent with studies on fcc metal pillars, where orientation was found to have a minor influence on the critical resolved shear stress and its size dependence [24, 26]. Therefore, this study aims to shed light on the effect of orientation on the size dependence of bcc pillars by analyzing the stress-strain response as well as the deformation morphology for single slip and multiple slip configurations of different bcc metals. To avoid differences in microstructure, all orientations of a given material were prepared from the same bulk single crystal. Micro- and nanopillars were FIB machined on the surfaces of Nb and W crystals oriented for single slip deformation and subsequently compressed with a nanoindenter. Post-mortem scanning electron microscopy (SEM) was used to verify the expected slip behavior. The results were compared to those of previous studies on [001] Nb and W (chapter 5, [170]) as well as [001] and [235] Mo (chapter 4, [164]).

### 7.3 Experimental Procedure

Tungsten (W), molybdenum (Mo) and niobium (Nb) samples with multiple slip [001] and single slip [235] orientation were prepared from single crystals by means of electron discharge machining after the orientations of the crystals were determined by Laue diffraction. The sample surfaces perpendicular to either the [235] or [001] direction were mechanically and electrochemically polished using material specific solutions [175]. It is important to note that both orientations of a given material were cut from the same bulk sample and that the surface preparation was identical for the different orientations of the same material. Pillars with diameters ranging from 200 nm to 6  $\mu\text{m}$  were machined on the surfaces of the oriented bcc samples by using a Dual Beam FIB. During the cutting procedure the sample surface was held normal to the ion beam, which created a slight taper of the pillar amounting to  $2.7^\circ$  on average. The pillars were compressed in a load-controlled mode by a nanoindenter equipped with a 10  $\mu\text{m}$  diameter diamond or sapphire flat punch. In order to ensure equal deformation rates, the loading rates were varied between 1 and 250  $\mu\text{N/S}$  depending on pillar diameter. For consistency, the pillar top diameter was used to calculate engineering stress-strain data. To get an accurate measure of the strain, the elastic deformation of the indenter and the base material were estimated and subtracted. Further description of the testing and the data analysis can be found in [26].

### 7.4 Results

Figure 7.1 shows representative SEM images of [235] oriented W and Nb pillars after deformation. The W pillars in Fig 7.1a and b have diameters of approximately 280 nm and 3000 nm; the Nb pillars in Fig 7.1d and e have diameters of 400 nm and 4500 nm. These pillars were chosen to represent the deformation behavior over the size range tested in this study. For the W pillars, which were deformed to approximately 10% strain, slip traces indicative of slip along a preferred slip system were observed on the pillar surface. However, high magnification images of the glide steps, as shown in Fig. 7.1c, demonstrate that several crystallographic glide planes contribute to the deformation. A similar waviness of glide steps was found for [001] W and [001] Mo pillars (chapter 4 and 5), and has also been observed in bulk single crystal studies [30, 32], where the wavy slip behavior was attributed to cross-slip of  $a/2 \langle 111 \rangle$  screw dislocations [30, 32]. In contrast, the glide steps of the Nb pillars are well resolved on single crystallographic planes even at higher magnifications (Fig. 7.1f), which is consistent with the observations in previous studies [166, 170]. Additionally, for Nb pillars

deformed to larger strains, a contribution of a secondary slip system was detected. In other words, slip traces were observed along a system that was clearly less favorable. This observation was made exclusively for pillars that were heavily deformed ( $> 20\%$  strain), similar to the example pillar shown in Fig. 7.1e.

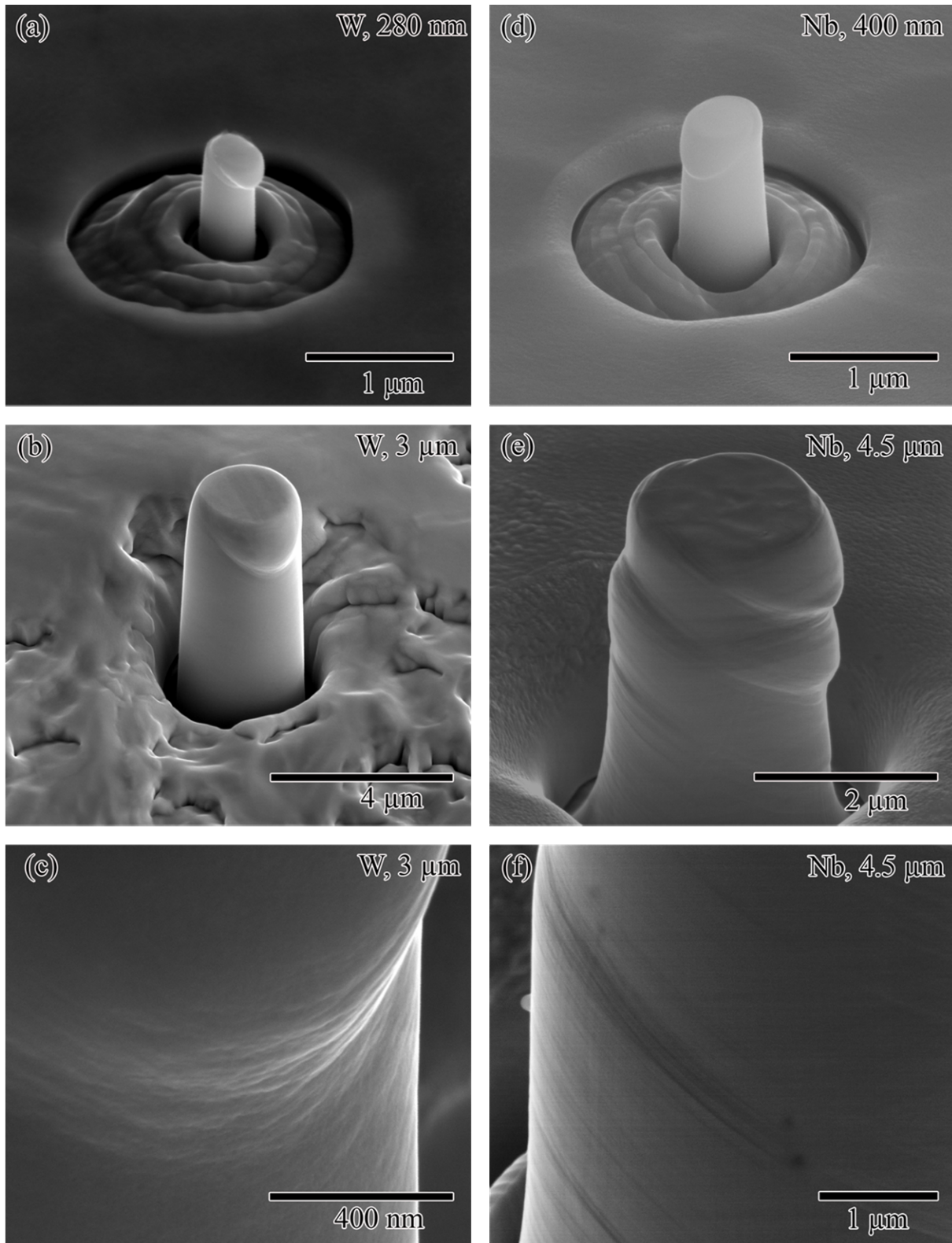


**Figure 7.1:** Post-compression SEM images of representative [235] oriented W and Nb pillars: (a) 280 nm W, (b-c) 3000 nm W, (d) 400 nm Nb, and (e-f) 4500 nm Nb pillars. The pillars in (a-d) were deformed to 10 %, whereas the pillar in (e) was deformed to 40%. Both materials show slip traces indicative for single slip deformation; only at higher strains other slip systems were observed for the Nb pillars. Higher magnification images of (c) W and (f) Nb pillars highlight differences in slip trace morphologies between both materials.

Representative stress-strain curves for the [235] oriented W and Nb pillars, with diameters ranging from 200 to 4500 nm, can be seen in Fig 7.2a and b. For both materials, the stress-strain data displays key features indicative of load-controlled pillar compression [29, 124]. Pillars with diameters above 2  $\mu\text{m}$  exhibit relatively continuous stress-strain curves, whereas for smaller pillars strain bursts separated by nearly elastic loading segments appear. The strain hardening rate (SHR) increases with decreasing pillar diameter, with exception of large strain bursts in small pillars that led to brief apparent strain softening.

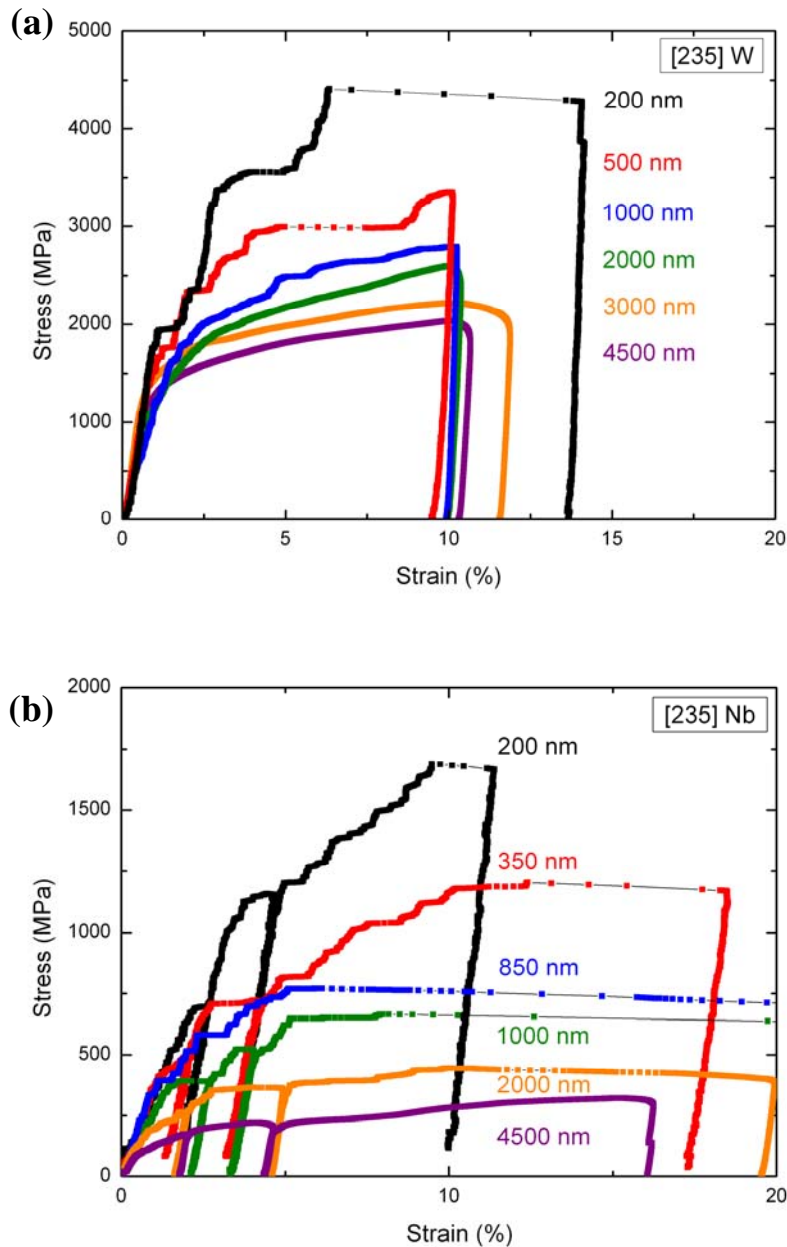


**Figure 7.2:** Representative stress-strain curves of [235] oriented W (a) and Nb (b) pillars with diameters ranging from 200 to 4500 nm

The SHR is plotted in comparison with data for [001] W and [001] Nb in Fig. 7.3. The strain hardening rate is defined to be the slope of the stress-strain data between 2.5 and 10% strain, consistent with previous pillar studies [24, 26]. This definition also captures large strain bursts, and therefore the scatter in the data is significant. It is evident that for comparable diameters, the W pillars generally show higher SHR than the Nb pillars, while an overall increase in SHR with decreasing pillar diameter is found for both materials. A similar increase in the SHR with decreasing pillar diameter and comparable nominal values were observed for fcc Au [24] and fcc Ni [26].

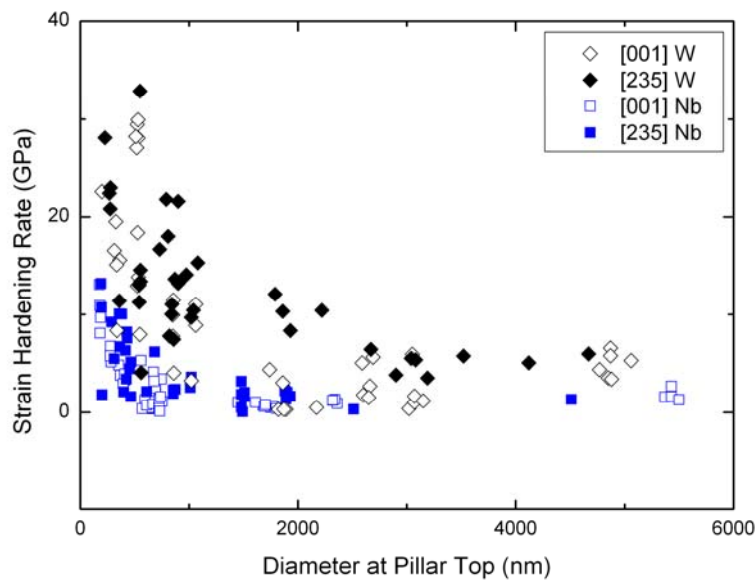


**Figure 7.3:** Strain hardening rate versus pillar diameter for all [235] and [001] oriented W and Nb pillars. The strain hardening rate is defined to be the slope of the stress-strain curves measured between 2.5 and 10% strain.

The yield strength, taken to be the stress at 2.5% strain, as a function of pillar diameter for the [235] oriented W and Nb pillars as well as data for [001] oriented W and Nb pillars from a previous study [170] is explicitly shown in Fig. 7.4. The use of the 0.2% offset method for determining the yield stress was not possible, due to the low initial stiffness caused by slight indenter-pillars misalignment and surface roughness. Stress at an axial strain of 2.5% was chosen as a representation of yield strength as it is high enough to ensure that plastic deformation had occurred, while still low enough to limit the influence of the strain hardening. The strength values for the W pillars are significantly larger than for the Nb pillars over the entire size range investigated, although the relative difference between the strength values is the largest for the largest pillar diameters. With decreasing pillar diameter, the relative difference in strength decreases from a factor of 11.4 at 4  $\mu\text{m}$  (1650 MPa vs. 145 MPa) to a factor of 4.2 at 200 nm (2800 MPa vs. 670 MPa) for the [235] oriented samples.



For both materials the strength is shown to be inversely related to the pillar diameter, with a best fit line of  $\sigma_y \propto d^{-0.16}$  for the [235] and [001] W pillars and  $\sigma_y \propto d^{-0.42} - d^{-0.45}$  for [235] and [001] Nb pillars, respectively. The relatively similar size dependence for the different orientations of the same material is in contrast to results on Mo pillars, where a significantly different size effect given by  $\sigma_y \propto d^{-0.22}$  and  $d^{-0.36}$  was observed for [001] and [235] oriented Mo pillars, respectively (chapter 4, [164]).

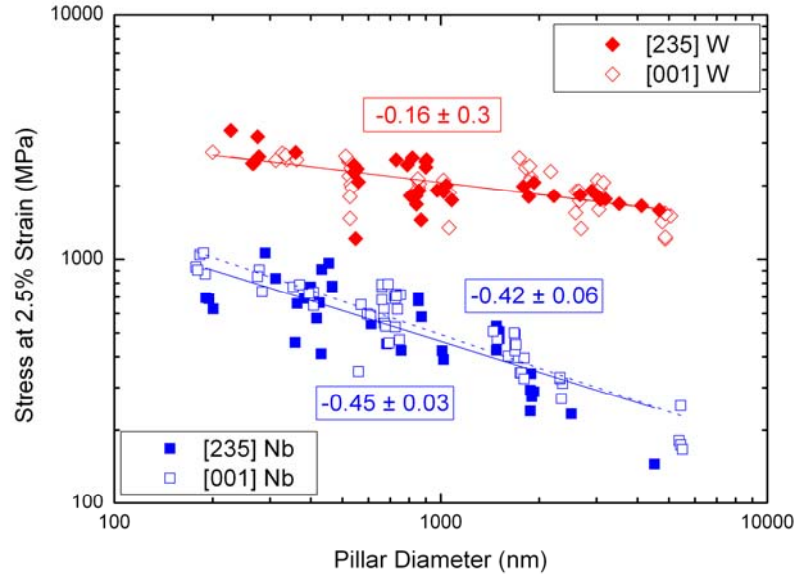


**Figure 7.4:** Stress at 2.5% strain as a function of pillar diameter for [235] and [001] oriented W and Nb. Plot is scaled logarithmically, and shows a power law exponent of -0.166 for [235] W and -0.163 for [001] W pillars, whereas Nb pillars exhibit a power law exponent of -0.42 for [235] and -0.45 for [001] orientations.

For the single slip and multiple slip samples of W, Mo and Nb, the scaling of the yield strengths relative to diameter was found to be material dependent. To account for the different deformation temperature with respect to the critical temperature, the power law exponent obtained from the best fit line is plotted as a function of the ratio  $T_{test}/T_c$  in Fig. 7.5. For comparison, the power law exponent obtained from the best fit line of the flow stress measured at 5% strain is also shown. It can be seen that independent of the strain value at which the size dependence was determined, the [235] oriented bcc pillars show a similar scaling of the power law exponent with  $T_c$  as recently observed for [001] oriented bcc pillars (chapter 5, [170]). For W with a small ratio of  $T_{test}/T_c$  the size dependence is weaker than for Nb with a large ratio of  $T_{test}/T_c$ . Extrapolation of the fit lines shown in Fig. 7.5 demonstrates that for  $T_{test}/T_c$  close to one, the relationship between yield strength and diameter would give values between  $d^{-0.5}$  to  $d^{-0.6}$ . These values are remarkable similar to the power law exponents reported for fcc pillars [29, 122, 124].

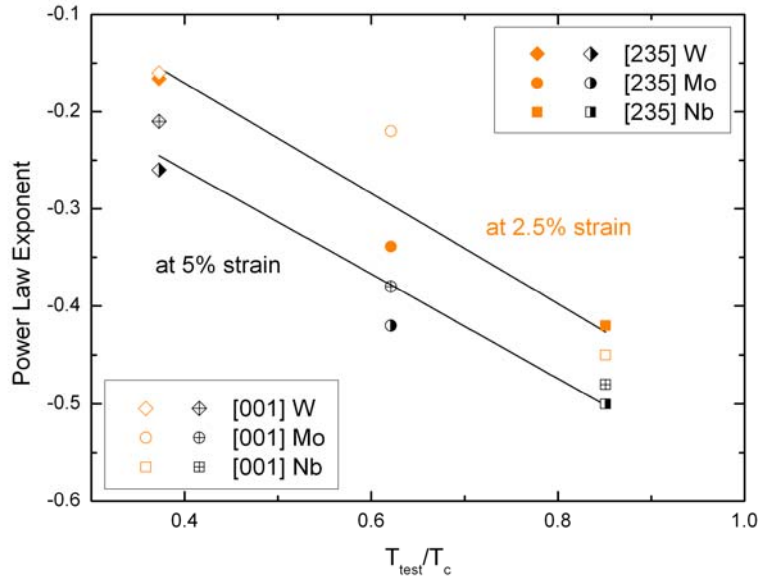


**Figure 7.5:** Slope of the line of best fit (exponent) for the size dependence of the bcc metals shown in Fig. 7.4 and [170] as a function of  $T_{\text{test}}/T_c$  (see text). Also shown are the power law exponents obtained for the flow stress measured at 5% strain for the same materials. The critical temperature for W is 800 K [65]; for Mo  $T_c$  is 480 K [63] and for Nb  $T_c = 350\text{K}$  [67].

In Fig. 7.6 the critical resolved shear stresses (CRSS) of the bcc pillars from Fig. 7.4 are compared with data from recent fcc pillar studies [22, 24, 26]. For the calculation of the CRSS values, the active glide plane was taken to be the (112) plane, resulting in Schmid factors of 0.45 and 0.47 for the [235] and [001] orientation, respectively. To account for specific material parameters, the CRSS values were normalized with the resolved shear modulus and the Burgers vector. The explicit purpose of this normalization is to directly compare strength values as a function of diameter for multiple fcc and bcc materials. The resolved shear modulus,  $\mu$ , was calculated for imposed strain in  $\langle 111 \rangle \{112\}$  for bcc metals, and in  $\langle 110 \rangle \{111\}$  for fcc metals. Calculations using the stiffness values in [155] gave values of 188 GPa for W and 58.7 GPa for Nb. The values for Au and Ni were calculated to be 23.7 GPa and 74.6 GPa, respectively. In general, both W and Nb demonstrate elevated strength values relative to the fcc materials. This observation is most pronounced for relatively large diameters in the micron range. For Nb, in Fig 7.6a, the normalized CRSS values overlap with the fcc pillar data over a considerable size range, whereas for W shown in Fig. 7.6b, comparable values are only found for pillar diameters close to 200 nm.

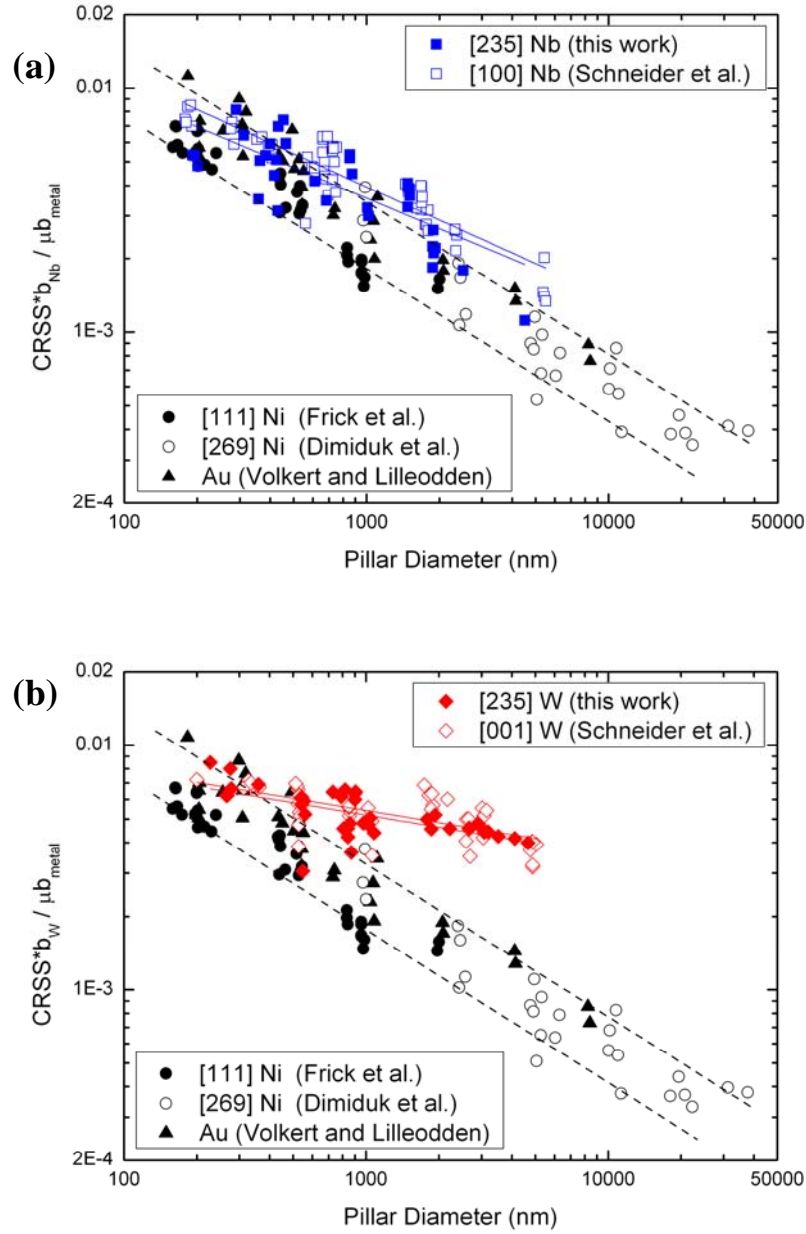


**Figure 7.6:** Comparison plots of CRSS versus diameter showing [001] and [235] Nb (a) and W (b) pillar data from this work, along with compression data for [111] Ni, [269] Ni, and low symmetry Au pillars [22, 24, 26]. For the calculation of the CRSS values a Schmid factor of 0.27 was used for [111] Ni, while a Schmid factor of 0.48 was utilized for [269] Ni and low symmetry Au. CRSS values have been normalized with respect to resolved shear modulus and Burgers vector to facilitate direct comparison.

## 7.5 Discussion

The SEM images of the [235] W and Nb pillars show that on a macroscopic level the deformation occurs on a single glide plane (Fig.7.1). However, high magnification images of the W pillars demonstrate that the glide steps are wavy in nature. This has been frequently observed in previous studies on bcc bulk metals and indicates that on a microscopic level the screw dislocations cross-slip between several crystallographic planes with their Burgers

vector as zone axis [30, 32]. In contrast, the glide planes for Nb are well defined indicating a minor contribution of cross-slip. A similar material dependent deformation morphology was observed in a previous study on [001] oriented bcc pillars and was explained by the effect of the critical temperature on the ability of the dislocations to cross-slip (chapter 5; [170]). Due to their relative immobility, the average length of the screw dislocation segments will increase with increasing difference between  $T_{\text{test}}$  and  $T_c$ . Thus for W, the dislocations are almost entirely of screw character and therefore have a high inherent tendency to cross-slip. For Nb, the dislocations deviate from pure screw character over a considerable length, mitigating their ability to cross-slip and thus dislocation motion occurs on a well defined slip plane. Furthermore, less favorable slip systems relative to the primary ones were observed for heavily deformed Nb pillars (Figure 7.1e). The activation of these slip systems could be caused by an exhaustion of mobile dislocations on the primary slip system or by a slight rotation of the pillar axis [176], which can lead to increased resolved shear stresses on originally unfavorable glide planes. However, due to the fact that the activation of less favorable slip systems occurred only at high strains ( $> 20\%$  strain), their influence was neglected for the following interpretation of the mechanical properties such as yield strength and SHR, which were both determined at strain values smaller than 10%.

For both bcc materials tested in this study, the key features of load-controlled pillar compression are visible in the stress-strain curves. Large pillars show continuous stress-strain curves while small pillars exhibit a staircase-like stress-strain response, where strain bursts are separated by elastic loading segments. Strain bursts have been shown to be related to avalanche-like dislocation events [138]. The strain generated by these events is relatively minor for large pillars; however, it becomes more significant with decreasing pillar size. The intermittency of plastic flow may be explained by the activation and subsequent exhaustion of dislocation sources [127, 141]. Qualitatively, the shape of the stress-strain curves of the [235] oriented pillars is very similar to those of the [001] oriented pillars of the same material. This was shown for [235] and [001] Mo in a study by Zaiser et al. [145], where the different orientations were found to have a remarkable similarity in the strain burst distribution for a given pillar diameter. Although the ratio between test temperature and  $T_c$  is different for Nb and W, both metals qualitatively demonstrate a similar strain hardening behavior. This is inconsistent with the deformation of bulk bcc single crystals, where the critical temperature has a strong influence on the shape of the stress-strain curves [31]. Tested well below  $T_c$ , for example W tested at RT, the stress-strain curve of bulk bcc single crystals has a parabolic shape [65]. For an elevated test temperature close to  $T_c$ , the shape of the stress-strain curve for

bulk bcc resembles the classical III stage hardening curves of fcc metals [90]. This suggests that for bcc metal samples with micron and submicron dimensions other dislocation processes than in bulk dominate the deformation and overwhelm temperature dependent characteristics, which are observed in the stress-strain response of bulk bcc single crystals.

Similar to fcc pillars and independent of orientation, the SHR of the W and Nb pillars increases with decreasing pillar diameter. In addition, the nominal values for the SHR are of the same order for the different bcc metals and are remarkably similar to those of fcc metals [24, 26]. Tungsten, the material with the highest  $T_c$ , exhibits slightly higher SHR values compared to Nb, which is somewhat surprising, as bulk bcc metals tested well below  $T_c$  are known to have vanishing strain hardening [32]. Below  $T_c$ , the SHR of bulk bcc metals is nominally zero, because the flow stress is primarily controlled by the thermally activated motion of screw dislocations, and dislocation-dislocation interactions are not the dominant contribution [32]. Because the dislocation density is not expected to be significantly higher in pillars than in bulk material, it seems highly unlikely that dislocation-dislocation interactions can explain the high SHR values. This is in agreement with our recent experiments on Mo pillars, which have been deformed, then re-cut with the FIB and tested again (chapter 6, [174]). This study revealed that the yield strength as well as the SHR were not affected by pre-straining demonstrating that dislocation multiplication and related forest hardening are not of crucial importance for the strength and the strain hardening behavior of bcc pillars. This may also explain why the SHR values for the single slip and multiple slip orientation are similar, even if strain hardening in bulk material is known to correlate with the number of activated slip systems. The missing sensitivity of the SHR to pre-straining, orientation and material suggests that, similar to fcc pillars, other dislocation processes than dislocation-dislocation interactions are responsible for the observed hardening. For fcc metals, the apparent hardening is frequently explained in terms of a source limited behavior, where the exhaustion of the weakest source leads to an increase in stress associated with the activation of less favorable dislocation sources [141]. Based on the observation that fcc and bcc pillars exhibit similar SHR values, it seems likely that for bcc pillars the same process leads to the observed hardening.

However, in contrast to fcc pillars, the size effect of the bcc pillars was found to correlate with a material specific parameter, i.e. the critical temperature. Since the same correlation was observed for single slip and multiple slip orientations, it can be assumed that conventional dislocation-dislocation interactions are not responsible for this effect. Instead, the strong influence of  $T_{\text{test}}/T_c$  – a temperature ratio, characteristic for the mobility of the screw

dislocations in bcc metals – suggests that the different size dependence of fcc and bcc metals is related to the low mobility of screw dislocations in bcc metals. If screw dislocation mobility is enhanced due to a high ratio of  $T_{\text{test}}/T_c$ , the bcc size effect is increased and approaches those of fcc pillars for a ratio of  $T_{\text{test}}/T_c$  close to one, further indicating that besides the screw dislocation mobility the size dependence of bcc and fcc pillars is controlled by similar dislocation processes, e.g. dislocation nucleation. In addition, it is demonstrated in Fig. 7.5 that the scaling of the power law exponent with respect to  $T_c$  is relatively independent of the strain value at which the stresses were determined, although the magnitude of the power law exponents increases with increasing strain. This shows that the effect of the screw dislocation mobility is independent of the amount of strain, which is reasonable, because the screw dislocation mobility is not controlled by dislocation-dislocation interactions.

If the yield stress is composed of a thermal and an athermal part, as proposed by Seeger for bulk bcc metals [83], the thermal part can be related to the thermally activated screw dislocation motion, whereas the athermal part is likely controlled by dislocation nucleation. For test temperatures close to  $T_c$ , the thermal part becomes negligible due to sufficient thermal activation of the screw dislocations and the flow stress of the bcc pillar is determined by the athermal dislocation processes. Because the critical temperature of Nb (350 K) is close to  $T_{\text{test}}$ , the strength of the Nb pillars is primarily controlled by athermal dislocation processes resulting in comparable normalized yield stresses for bcc Nb and fcc pillars. In contrast, for W the critical temperature (800 K) is far above the test temperature and therefore the thermal contribution to the flow stress associated with low screw dislocation mobility is significant. As a result, the W pillars exhibit much higher normalized yield stresses, and only at small diameters do the stresses converge with the fcc pillar data, further indicating that at small diameters the effect of screw dislocation mobility is weak.

Two concepts may explain the observations that for the smallest dimensions the influence of the screw dislocations is weak. Both are based on the assumption that the high Peierls potential of the screw dislocations is the primary difference between fcc and bcc pillar deformation. The first concept was proposed by the present author to explain the different size effect of bcc Mo and fcc pillars [164]. Slowly moving screw dislocations are thought to pile-up in front of dislocation sources. These kinetic pile-ups exert back stresses on dislocation sources making their operation more difficult in bcc compared to fcc metals [158]. For large pillar diameters there is enough space for the formation of such dislocation pile-ups explaining the large discrepancy in the normalized stresses (Fig. 7.6b). In small pillars, less space is available for pile-up formation and therefore bcc pillars and fcc pillars show similar

normalized stress values. If the influence of screw dislocation mobility is reduced by a higher deformation temperature, again no pile-up of the screw segments may occur and the flow stresses of fcc and bcc pillars are related to similar dislocation processes, e.g. dislocation nucleation, resulting in similar size dependence and comparable normalized yield strengths (Fig. 7.6a).

Additionally, another mechanism may play a significant role in bcc deformation behavior. The second concept is based on kink nucleation at the pillar surface, which can enhance the mobility of the screw dislocations [32, 144]. With increasing surface to volume ratio, the mobility of the screw dislocations increases and likely approaches those of edge dislocations at pillar diameters close to 200 nm. Thus, if the screw dislocations overcome the Peierls potential by surface assisted kink nucleation, the strength of bcc and fcc pillars may be controlled by the same size dependent dislocation processes; this would explain why bcc and fcc pillars show comparable normalized strengths at this size. It is important to note that these mechanisms are not mutually exclusive, and both may be active.

## 7.6 Conclusions

- Compression tests were performed on single slip Nb and W pillars. On a macroscopic level, slip traces indicative for single slip were observed on the surfaces of the deformed Nb and W pillars. However, high magnification images of the glide steps demonstrate that for W pillars several crystallographic glide planes contribute to the deformation, whereas for the Nb pillars the glide steps are well resolved on single crystallographic planes. As in bulk metals, the wavy glide steps of the W pillars can be attributed to the frequent cross-slip of screw dislocations. For the Nb pillars, the well resolved glide steps indicate that the propensity for cross-slip is reduced compared to bulk.
- The general characteristics of the stress-strain curves were found to be consistent to those observed in fcc pillars and other bcc pillars oriented for multiple slip. The similar behavior indicates that the shape of the stress strain curves is related to dislocation processes, which are not primarily controlled by the crystallographic nature of the sample.
- Size dependent yield stresses were observed for both materials, with relationships of:  $\sigma_y \propto d^{-0.16}$  for [235] W, and  $\sigma_y \propto d^{-0.42}$  for [235] Nb. The size dependence of the W and Nb pillars was shown to be independent of the orientation and to scale with  $T_c$ . With decreasing  $T_c$ , normalized yield stresses and size dependence of bcc pillars were found to

converge with those of fcc pillars. Similar convergence of the normalized yield stresses was observed with decreasing pillar diameter.

- Based on these results, it can be assumed that the mobility of the screw dislocation controls the size effect of the bcc pillars. With decreasing  $T_c$  or pillar diameter, the effect of the screw dislocations becomes less important and consequently the strength of fcc and bcc pillars are determined by similar dislocation processes. Possible explanations for this behavior include kinetic pile-ups of screw dislocations [164] and kink nucleation at the pillar surface [144].



## **8 Correlation Between Activation Volume and Pillar Diameter for BCC Pillars**

### **8.1 Abstract**

Compression tests with varying loading rates were performed on [001] and [235] oriented small-scale W, Mo and Nb pillars to determine the contribution of thermally activated screw dislocation motion during deformation. Calculated activation volumes were shown to be in the range of  $1.3b^3$  to  $9b^3$  and were found to decrease with pillar diameter. This suggests that the kink-pair nucleation of screw dislocations is enhanced by surface effects in the micron and submicron range.

## 8.2 Introduction

Compression tests on focused ion beam (FIB) machined, single crystal metal micropillars have shown that the flow stress is inversely related to pillar diameter [19, 21, 22, 24, 26]. Although the fundamental mechanisms which govern the size effect are still under debate, a consistent scaling relationship for the flow stress  $\sigma_y$  with pillar diameter  $d$  of the form  $\sigma_y \propto d^{-0.6}$  to  $d^{-1.0}$  has been found for several face-centered cubic metals [19, 21, 22, 24, 26]. Because fcc and body-centered cubic (bcc) metals differ fundamentally in their dislocation processes, it is perhaps not surprising that bcc metals show a different size scaling on the order of  $\sigma_y \propto d^{-0.2}$  to  $d^{-0.4}$  [143, 164]. The weaker size dependence of bcc metals has been attributed to the low mobility of screw dislocations in bcc metals leading to either conventional dislocation-dislocation interactions [143] or kinetic pile-ups of screw dislocations in the vicinity of dislocation sources [164]. To elaborate on the role of thermally activated screw dislocation motion in the deformation of small-scale bcc metal pillars, compression tests on Mo pillars were performed at various loading rates in a previous study [164]. Calculated activation volumes were found to be in the range of  $1.3b^3$  to  $5.3b^3$ , where  $b$  is the Burgers vector, which is in good agreement with activation volumes measured for thermally activated kink-pair nucleation of screw dislocations in bulk bcc Mo [163]. In this study the relationship between pillar diameter and calculated activation volumes are examined in more detail for Mo, and compared to new results from W and Nb pillars.

## 8.3 Experimental Procedure

For this study, [001] and [235] oriented Nb pillars, as well as [001] oriented W pillars with diameters between 300 and 2350 nm were FIB machined on the surfaces of high purity single crystals using a Dual Beam<sup>TM</sup> FIB. The different orientations for Nb were obtained from the same bulk single crystal by electron discharge machining after the orientations were first determined by Laue diffraction. For each orientation several diameters were investigated and for each diameter about 24 pillars were prepared. The pillars were tested at loading rates between 1 and 500  $\mu\text{N/s}$ . Loading rate variation was chosen, because it is readily controllable in the load-controlled nanoindenter. Top pillar diameters were used to calculate the engineering stress-strain and activation volumes. Further experimental details can be found in [164].

## 8.4 Results

The results of the loading rate tests for the [001] and the [235] oriented Nb and W pillars are shown in Figures 8.1a and b. Results for the [001] and [235] oriented Mo pillars can be found in (chapter 4). Consistent with the loading rate sensitivity known from bulk compression tests on bcc metals, the yield stress of the bcc pillars (taken to be the stress at 2.5% strain) increases with increasing loading rate independent of pillar diameter.

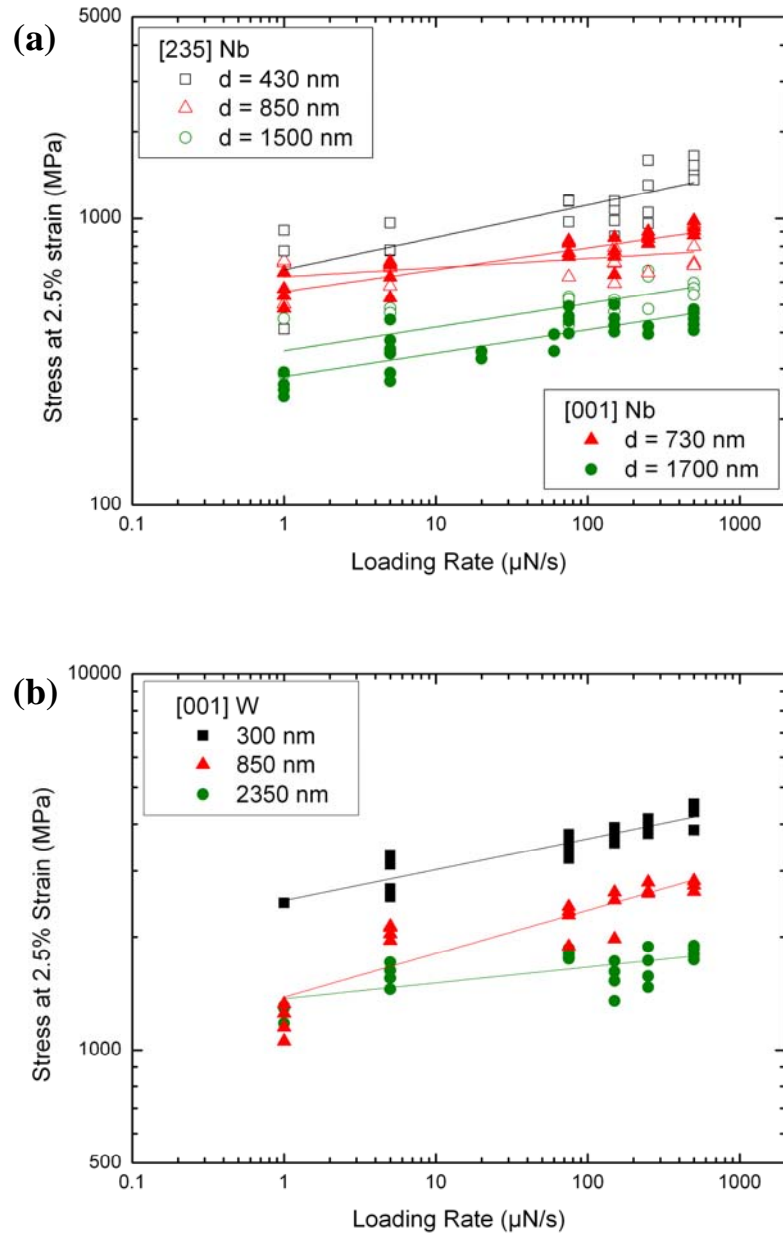


**Figure 8.1:** (a) Loading rate dependence for [001] and [235] oriented Nb pillars with diameters ranging from 430 nm to 1700 nm. (b) Loading rate dependence for [001] oriented W pillars with diameters ranging from 300 nm to 2350 nm.

To calculate the activation volumes based on the results shown in Figure 8.1, the loading rate was first converted to an elastic strain rate by dividing it by cross-sectional area and elastic modulus. For these inherently load controlled experiments the elastic strain rate was used as an approximation for the real strain rate. This seems to be valid, because the stresses were measured at very low strains, and it can be assumed that the deformation up to this point was nearly elastic. The activation volume  $v$  was calculated based on the equation [49]:

$$v = mkT \left( \frac{\partial \ln \dot{\epsilon}}{\partial \sigma} \right) \quad (8.1)$$

where  $m$  is a constant taken to be the reciprocal Schmid factor (2.128 for the [001] and 2.222 for the [235] orientation),  $k$  is Boltzmann's constant,  $T$  is temperature,  $\dot{\epsilon}$  is strain rate, and  $\sigma$  is stress. According to Equation 8.1, the slope obtained from plotting the natural log of the strain rate versus stress, as demonstrated in Figure 8.2 for the [001] oriented W pillars, is proportional to the activation volume. For the W pillars, calculated activation volumes were found to be in the range of  $1.3$  to  $3.1b^3$ , while for the Nb pillars slightly higher values were obtained ( $2.2$  to  $8.8b^3$ ). Thus, the Nb and W pillars exhibit very similar activation volumes as observed for [001] and [235] Mo (chapter 4; [164]). The calculated activation volumes are summarized in Fig. 8.3.

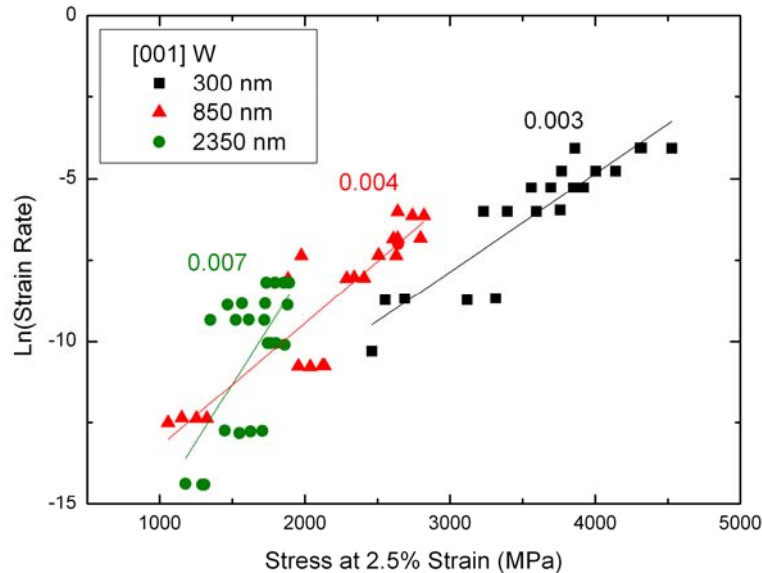


**Figure 8.2:** Natural log of elastic strain rate versus stress at 2.5% strain for [001] oriented W pillars. The slope of each curve is proportional to the activation volume for that pillar diameter (see Equation 8.1).

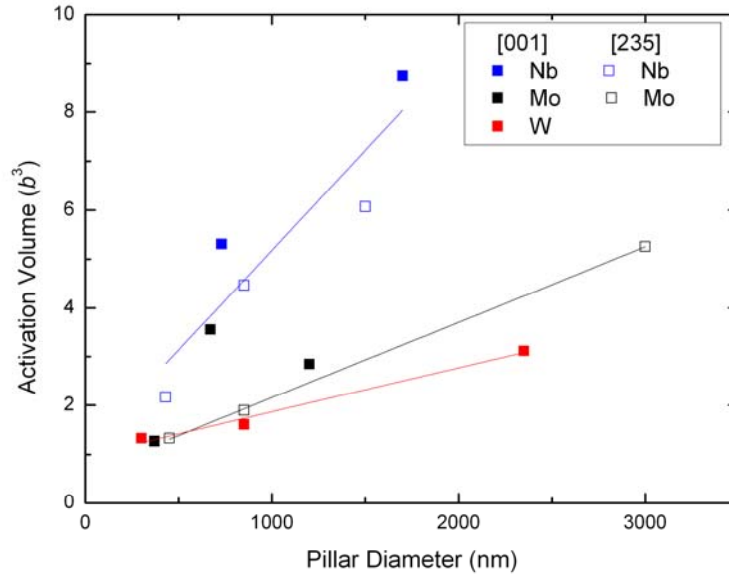


**Figure 8.3:** Calculated activation volumes for [001] and [235] oriented bcc metals as a function of pillar diameter. Activation volumes decrease with decreasing pillar diameter.

By comparing Fig. 8.1 and 8.3, it can be seen that for pillars with relatively large diameters, the activation volumes inversely scale with the yield stress. In other words, the materials with higher strength show smaller activation volumes. However, irrespective of the bcc metal, the activation volumes decrease with decreasing pillar diameter, with nominal values converging near 200 nm. For Nb, the material with the highest activation volume for a given diameter, the observed decrease is stronger than for W and Mo. For W, the material with the smallest activation volumes, the correlation between pillar diameter and activation volume is less pronounced. It is interesting to note that the material which shows the strongest size effect in strength (cf. chapter 5) also exhibits the strongest size effect for the calculated activation volumes. Further, it can be seen that the activation volumes for Nb and Mo pillars are relatively independent of the orientation. In addition, both orientations of Nb as well as of Mo show decreasing activation volumes with decreasing pillar diameter.

## 8.5 Discussion

The loading rate dependence of the yield stress and the calculated activation volumes in the range of  $1b^3$  to  $9b^3$  can be attributed to the screw dislocations, which surmount the Peierls potential with the aid of the thermally activated formation of kink-pairs. Activation volumes of about  $10b^3$  to  $50b^3$  are usually found for bcc bulk metals [46, 64, 161-163]. The slightly smaller values compared to bcc bulk material can be explained in terms of the high stresses in small-scale bcc pillars. At high stresses, which are due to the size effect of strength, less

thermal energy is required for the dislocations to overcome the Peierls potential. This is consistent with the findings that for a given diameter the activation volumes for the different materials show the inverse scaling as the yield strengths and that for all the tested bcc metals, including the different orientations of Nb and Mo, the calculated activation volumes consistently decrease with decreasing pillar diameter. In order to quantify this effect, the activation volume for the thermally activated kink-pair nucleation and its stress dependence were calculated following the approach of Seeger and Schiller [177]. Accordingly, the activation volume is given by

$$v = bh\lambda^*, \quad (8.2)$$

where  $b$  is the magnitude of the Burgers vector,  $h$  is the height of the kink, which is  $2\sqrt{2}/\sqrt{3}$  times the magnitude of  $b$  for slip on (112) planes, and  $\lambda^*$  is the distance between the two kinks of a kink-pair.  $\lambda^*$  is a strong function of the stress and can be expressed as

$$\lambda^* = \left( \frac{\mu b h}{8\pi\sigma} \right)^{1/2}, \quad (8.3)$$

where  $\mu$  is the shear modulus and  $\sigma$  is the applied stress. Using the average yield strength values measured with the lowest loading rate for each set of diameters and the anisotropic shear modulus for the most favorable (112) slip system (188 GPa for W, 158.4 GPa for Mo, and 58.7 GPa for Nb), activation volumes of  $3.6b^3$  to  $5.2b^3$  were calculated for the W pillars,  $3.7b^3$  to  $6.3b^3$  for the Mo pillars and  $3.8b^3$  to  $6.2b^3$  for the Nb pillars. These activation volumes are very close to those obtained from the measured loading rate dependence. However, for the small pillar diameters, the experimental values are smaller than predicted by the kink-pair theory. This suggests that the high flow stress of the bcc pillars may be responsible for the small activation volumes compared to bulk; however, the size dependence of strength is insufficient to explain the size effect of the measured activation volumes. The latter can be verified by using equation (8.3) and the previously determined stress diameter relationship (chapter 5 and 7) for estimating the expected diameter dependence of the activation volume associated with the size dependence in strength. For example, this results in  $v \propto d^{0.08}$ ,  $v \propto d^{0.11}$  and  $v \propto d^{0.21}$  for [001] W, Mo and Nb, respectively. Thus, the estimated diameter dependence reflects the trends observed in Fig. 8.3; however, it significantly underestimates the measured diameter dependence of the activation volumes, which is  $v \propto d^{0.41}$  for W,  $d^{0.73}$  for Mo and  $d^{0.83}$  for Nb. Therefore, the strength increase alone cannot account for the size dependence of the activation volumes. Another mechanism most certainly

assists the screw dislocations to overcome the Peierls potential and reduces the thermal energy required for screw dislocation motion. As previous studies [32, 144] have pointed out that single kinks can be nucleated at the free surface, it is likely that due to the large surface to volume ratio of the tested pillars surface assisted kink nucleation reduces the thermal energy required for screw dislocation motion compared to bulk. Consequently, the thermal component of the yield stress associated with the screw dislocation motion decreases with decreasing pillar diameter.

In previously published work comparing bcc pillars to fcc pillars [164, 170], normalized stresses were found to be very similar at pillar diameters close to 200 nm. Enhanced mobility of screw dislocations and ease of kink-pair nucleation due to surface effects could explain this similarity. The difference in mobility between bcc edge and screw dislocations, which is responsible for the different mechanical behavior of bcc and fcc bulk metals, could be reduced due to surface assisted kink nucleation. Thus in smaller pillars, similar dislocation processes may lead to comparable strengths for fcc and bcc. For larger bcc pillars, with smaller surface to volume ratio and therefore less surface assisted kink nucleation, the difference in mobilities of screw and edge dislocations would result in a deviation in strength between fcc and bcc pillars, as observed for W, Mo and Nb pillars (chapter 4 and 7).

However, further experiments and modeling have to be done to sort out the relative contribution of surface effects and stress level on the size dependence of the activation volume. For future work, we consider loading rate tests on pillars with different cross-sectional shapes. Varying the cross-sectional shape while keeping the cross-sectional area constant would enable to test different surface to volume ratios at equal stresses. Thus, it should be possible to distinguish between both contributions.

## 8.6 Conclusions

- Bcc micro- and nanopillars were compressed at various loading rates ranging from 1 to 500  $\mu\text{N/s}$ . Similar to bulk, the yield stress of the bcc pillars increases with increasing loading rate, which indicates the presence of thermally activated dislocation processes.
- The activation volumes calculated from the measured loading rate sensitivity are in the range of  $1b^3$  to  $9b^3$ . This shows that the time-dependent deformation is caused by the thermally activated kink-pair formation on screw dislocations. Further, the activation

volumes were found to decrease with decreasing pillar diameter suggesting that in small dimensions less thermal energy is required for screw dislocation motion.

- Due to an inverse scaling of activation volume and yield stress, the size dependence of the activation volumes may be caused by the size effect of strength observed for the bcc pillars. However, calculations according to Seeger's kink-pair theory have shown that the strength increase alone cannot account for the size dependence of the activation volumes.
- It is suggested that with decreasing pillar diameter, i.e. with increasing surface to volume ratio, kinks are favorably nucleated at the sample surface and therefore less thermal energy is required for screw dislocation motion. Thus in smaller pillars, similar dislocation processes may lead to comparable strengths for fcc and bcc.



## 9 Summary

The plastic deformation in bcc metals differs fundamentally from that of fcc metals. In bcc metals, the deformation is largely controlled by screw dislocations which, due to the geometry of the glide planes, have non-planar dislocation cores and high Peierls potentials. This intrinsic resistance to their motion can be overcome through thermally activated kink-pair formation, leading to a strong temperature and strain rate dependence of the flow stress. Although these fundamental differences between the deformation behavior of fcc and bcc metals have been characterized in bulk, it is not well known how the mechanical properties of bcc metals may deviate from those observed in previous studies on fcc metals with dimensions in the micrometer and submicrometer range.

In the present study the mechanical properties of small-scaled bcc metal structures were investigated. For this purpose, microcompression tests were performed on FIB machined, [001] and [235] oriented W, Mo and Nb pillars with diameters ranging from 200 nm to 6  $\mu\text{m}$ . The main results can be summarized as follows:

- The stress-strain curves of the [001] and [235] oriented W, Mo and Nb pillars exhibit the key features of load-controlled single crystal pillar compression. Large pillars show smooth plastic flow, while small pillars demonstrate strain bursts separated by elastic loading segments. In contrast to bulk, the sample orientation and the critical temperature of the tested material have no influence on the strain hardening behavior.
- Both the critical temperature  $T_c$  and the pillar diameter have a strong influence on the deformation morphology. For metals with a high critical temperature, the glide steps are wavy in nature. This is typical for bcc metals and indicates frequent cross-slip of screw dislocations. However, for pillars with smaller diameters and metals with a low critical temperature, the glide steps are well resolved on single crystallographic planes.
- [001] and [235] oriented W, Mo and Nb pillars show size dependent yield stresses. However, the size dependence scales with  $T_{\text{test}}/T_c$  and for  $T_{\text{test}} < T_c$  it is less pronounced than for fcc pillars. Bcc metals with a high critical temperature relative to  $T_{\text{test}}$  exhibit a weak size dependence, whereas bcc metals with a low critical temperature demonstrate a strong size dependence.
- Normalized yield stress values for fcc and bcc pillars converge at pillar diameters of approximately 200 nm. At larger diameters, the yield stresses for bcc pillars are

substantially higher than for fcc pillars, and the relative differences increase with the critical temperature of the bcc metal.

- The yield stress of the bcc pillars is strain rate dependent. Similar to bulk, the yield stress of the bcc pillars increases with increasing strain rate. Calculated activation volumes are in the range of  $1b^3$  to  $9b^3$  and were found to decrease with decreasing pillar diameter.
- The bcc pillars show significant strain hardening, which increases with decreasing pillar diameter. However, pre-straining of several percent has no influence on the mechanical properties such as yield stress and strain hardening rate if the pillar is re-shaped with the FIB before testing.

In Table 9.1 and 9.2, the mechanical properties of the tested bcc pillars are compared to those of bcc bulk material and fcc pillars.

**Table 9.2:** Comparison of the mechanical properties of bcc pillars and bcc bulk material.

	<b>Bcc pillars</b>	<b>Bcc bulk material</b>	<b>Conclusion</b>
<b>Shape of the stress-strain curve</b>	<ul style="list-style-type: none"> <li>- Jerky deformation, i.e. plastic strain bursts separated by elastic loading segments</li> <li>- SHR increases with decreasing pillar diameter</li> <li>- Strain hardening is not affected by the critical temperature and the sample orientation</li> </ul>	<ul style="list-style-type: none"> <li>- Continuous deformation</li> <li>- SHR is size independent</li> <li>- Strong effect of critical temperature and sample orientation on strain hardening</li> </ul>	The different deformation and strain hardening behavior of the pillars compared to bulk material suggests that other dislocation processes than in bulk dominate the deformation of the pillars.
<b>Deformation morphology</b>	<ul style="list-style-type: none"> <li>- Wavy slip lines for large W and Mo pillars; well resolved slip lines for Ta and Nb pillars</li> <li>- W and Mo pillars show a transition in the slip behavior. Below 1-2 <math>\mu\text{m}</math> the slip lines are no more wavy</li> </ul>	<ul style="list-style-type: none"> <li>- Wavy slip lines for W, Mo, Ta and Nb</li> <li>- Deformation morphology is size independent</li> </ul>	As for bulk material, the wavy slip lines indicate the frequent cross-slip of screw dislocations. For the Ta and Nb pillars as well as for the small W and Mo pillars, the propensity for cross-slip is reduced compared to bulk. This suggests that screw dislocation motion is less relevant for the deformation of these pillars.
<b>Yield stress</b>	<ul style="list-style-type: none"> <li>- Increases with decreasing pillar diameter</li> <li>- Strain rate dependent</li> <li>- Scales with <math>T_c</math>, i.e. <math>T_{\text{test}}/T_c</math></li> </ul>	<ul style="list-style-type: none"> <li>- Size independent</li> <li>- Strain rate dependent</li> <li>- Scales with <math>T_c</math>, i.e. <math>T_{\text{test}}/T_c</math></li> </ul>	Similar to bulk, the yield stress of the bcc pillars is related to the thermally activated screw dislocation motion; however, other dislocation processes may cause the size dependence of the yield stress.

**Table 9.2:** Comparison of the mechanical properties of bcc and fcc pillars.

	<b>Bcc Pillars</b>	<b>Fcc Pillars</b>	<b>Conclusion</b>
<b>Shape of the stress-strain curve</b>	<ul style="list-style-type: none"> <li>- Frequent plastic strain bursts separated by elastic loading segments</li> <li>- SHR increases with decreasing pillar diameter</li> <li>- Orientation has no effect on SHR</li> </ul>	<ul style="list-style-type: none"> <li>- Frequent plastic strain bursts separated by elastic loading segments</li> <li>- SHR increases with decreasing pillar diameter</li> <li>- Orientation has no effect on SHR</li> </ul>	Similarities in the stress-strain curves indicate that similar dislocation processes occur in fcc and bcc pillars.
<b>Deformation morphology</b>	<ul style="list-style-type: none"> <li>- Wavy slip lines for large W and Mo pillars</li> <li>- Well resolved slip lines for Ta and Nb pillars as well as for small W and Mo pillars</li> </ul>	<ul style="list-style-type: none"> <li>- Well resolved slip lines</li> </ul>	In contrast to fcc pillars, screw dislocation motion greatly influences the deformation of the bcc pillars. For Nb and Ta as well as for small pillar diameters, the influence is less dominant.
<b>Yield stress</b>	<ul style="list-style-type: none"> <li>- Size dependent</li> <li>- Strain rate dependent</li> <li>- Different materials show different normalized yield stresses, which scale with <math>T_{\text{test}}/T_c</math></li> <li>- Converge with fcc pillar data at diameters of about 200 nm</li> </ul>	<ul style="list-style-type: none"> <li>- Size dependent</li> <li>- Expected to be strain rate independent</li> <li>- Different materials exhibit comparable normalized yield stresses</li> <li>- Converge with bcc pillar data at diameters of about 200 nm</li> </ul>	In both crystal structures, the limited sample volume has a strong influence on the dislocation processes. For bcc pillars, the screw dislocations contribute to the deformation leading to the strain rate dependence and the scaling of the yield stress with $T_{\text{test}}/T_c$ . Similar yield stresses for fcc and bcc pillars at small diameters suggest that the contribution of the screw dislocations decreases with the pillar diameter.
<b>Size dependence</b>	<ul style="list-style-type: none"> <li>- Can be described by a power law</li> <li>- Power law exponent is different for different materials</li> <li>- Power law exponent scales with <math>T_{\text{test}}/T_c</math> and for <math>T_{\text{test}}/T_c &lt; 1</math>, its magnitude is smaller than for fcc metals. For <math>T_{\text{test}}/T_c</math> close to one, the power law exponent approaches a value of about -0.6</li> </ul>	<ul style="list-style-type: none"> <li>- Can be described by a power law</li> <li>- Universal power law exponent of -0.6 for different fcc metals</li> </ul>	The scaling of the power law exponent with $T_{\text{test}}/T_c$ shows that the mobility of the screw dislocations is an important parameter for the size effect in bcc metals.

The comparisons in Tables 9.1 and 9.2 show that, similar to fcc pillars, the mechanical properties of the bcc pillars are size dependent: The yield stress, the strain hardening rate and the frequency of the strain bursts increase with decreasing sample size. This indicates that the limited sample volume has a strong influence on the dislocation processes in bcc metals as well. Besides this, the size dependence as well as the yield stress is correlated to  $T_{\text{test}}/T_c$  – a temperature ratio, characteristic for the mobility of the screw dislocations in bcc metals – suggesting that, as for bcc bulk material, the mobility of the screw dislocations is an important parameter for the deformation of small-scale bcc metal structures. The different size dependence of fcc and bcc pillars, which is schematically shown in Fig. 9.1, is likely related to this material specific parameter.

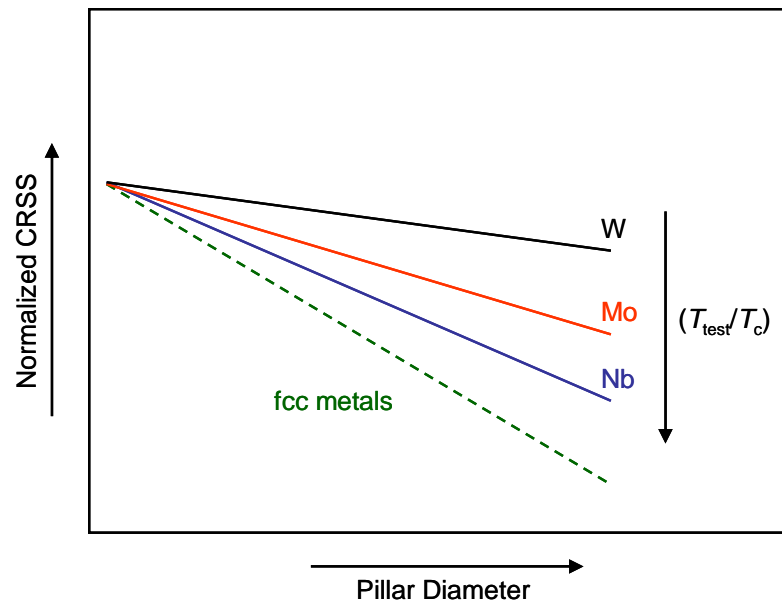


**Figure 9.1:** Schematic showing the size dependence of the normalized yield stress for bcc and fcc pillars.

Since the size dependence of the bcc pillars approaches those of fcc pillars for  $T_{\text{test}}/T_c$  close to one, it can be assumed that for a similar mobility of edge and screw dislocations the size effect in fcc and bcc pillars is caused by the same dislocation processes. For different mobilities, i.e. for  $T_{\text{test}}/T_c < 1$ , the dislocation processes in bcc pillars may deviate from those in fcc pillars. For example, in recent studies by Greer et al. [126] and Brinckmann et al. [143] it was shown that the low mobility of the screw dislocations can enhance dislocation-dislocation interactions in bcc pillars compared to fcc pillars. However, our experiments on pre-strained Mo pillars (chapter 6) demonstrate that dislocation accumulation and related forest hardening are not of crucial importance for the mechanical behavior of the bcc pillars. In addition, the tested bcc pillars exhibit the same strain burst behaviour as recently observed

for fcc pillars, which is usually attributed to the activation and subsequent exhaustion of dislocation sources.

Consequently, the mechanical behavior of bcc pillars could be explained by the activation of dislocation sources and the special role of screw dislocations in bcc metals. The activation and subsequent exhaustion of dislocation sources may lead to the characteristic stress-strain response of micropillar compression and increasing strain hardening rates with decreasing pillar diameter. The yield stress and its size dependence may then be determined by the activation stress of the sources and the low mobility of the screw dislocations inherent to the bcc crystal structure. For large diameters the low mobility of the screw dislocations may lead to backstresses on dislocation sources and thus make source operation more difficult. This could explain the high yield stresses compared to fcc pillars. A decreasing influence of the screw dislocations with decreasing diameter may result in the convergence of the yield stresses for fcc and bcc pillars at smaller diameters. Additionally, this may account for the transition in the deformation morphology and the decreasing activation volumes with decreasing pillar diameter. A possible reason for the negligible effect of screw dislocations for small pillar diameters may be kink nucleation at the surface. Kinks can easily nucleate at the sample surface and can enhance screw dislocation mobility [144]. Therefore, similar to fcc pillars, the yield stress of small bcc pillars may be controlled by the activation of dislocation sources. On the other hand, if sufficient thermal energy is available, the influence of the screw dislocations may be negligible even for pillars with larger diameters. Thus, the yield stress and the size dependence of bcc pillars can approach those of fcc pillars for  $T_{\text{test}}/T_c \geq 1$ .

# 10 Zusammenfassung in deutscher Sprache

## 10.1 Stand der Forschung und Motivation

Die mechanischen Eigenschaften von Metallen werden für Probendimensionen im Bereich von wenigen Mikrometern oder Nanometern durch so genannte Größeneffekte bestimmt. Für die Untersuchung dieser Größeneffekte werden in letzter Zeit vermehrt Mikrodruckversuche verwendet. Dabei werden mit einem Ionenstrahlmikroskop (Focused Ion Beam FIB) Säulen mit Dimensionen im Bereich von etwa 200 nm bis zu einigen Mikrometern in ein Massivmaterial geschnitten und anschließend in einem konventionellen Nanoindenter mit einer flachen Indenterspitze getestet [19, 29].

Mikrodruckversuche an kubisch-flächenzentrierten (kfz) Metallen haben durchweg gezeigt, dass die Fließspannung  $\sigma_y$  mit abnehmenden Säulendurchmesser  $d$  zunimmt und dabei einem Exponentialgesetz der Form  $\sigma_y \propto d^{-0,6}$  folgt [19, 21, 22, 24, 26]. In ersten Arbeiten an kubisch-raumzentrierten (krz) Mo-Säulen wurde eine deutlich geringere Abhängigkeit der Fließspannung vom Säulendurchmesser beobachtet [126, 143]. Dies deutet darauf hin, dass die Größeneffekte in krz und kfz Metallen durch unterschiedliche Versetzungsprozesse verursacht werden. Bei kfz Metallen geht man davon aus, dass die vorhandenen Versetzungen aufgrund des großen Oberflächen- zu Volumenverhältnis den Kristall verlassen [125, 127]. Dadurch verarmt der Kristall an mobilen Versetzungen und die Aktivierung von zusätzlichen Versetzungsquellen wird notwendig, um die Verformung aufrechtzuerhalten. Die geringe Mobilität der Schraubenversetzungen in krz Metallen könnte hingegen zu einer langen Verweilzeit der Versetzungen im Kristall führen, wodurch andere Versetzungsprozesse, wie zum Beispiel Versetzungswechselwirkungen, begünstigt werden können [126].

Ziel dieser Arbeit ist es, die Versetzungsprozesse, die das mechanische Verhalten krz Metalle in kleinen Dimensionen bestimmen, zu untersuchen. Hierzu wurden mit dem FIB Säulen mit Durchmessern von 200 nm bis 6  $\mu\text{m}$  in einkristallines Molybdän (Mo), Niob (Nb) und Wolfram (W) geschnitten und anschließend in einem Nanoindenter verformt. Diese Materialien wurden verwendet, weil sie sich in ihrer kritischen Temperatur  $T_c$  unterscheiden und somit der Einfluss der Mobilität der Schraubenversetzungen in krz Metallen bei einer konstanten, durch den verwendeten Nanoindenter festgelegten Testtemperatur  $T_{\text{test}}$  von 25°C bestimmt werden kann. Die kritische Temperatur ist ein Maß dafür, wie viel thermische Energie die Schraubenversetzung für die Überwindung des Peierls-Potentials benötigt, wenn

keine äußere Spannung ihre Bewegung unterstützt [31]. Für Testtemperaturen unterhalb von  $T_c$  muss umso mehr Spannung aufgebracht werden, je größer der Unterschied zwischen  $T_c$  und  $T_{\text{test}}$  ist. Daher wird erwartet, dass der Einfluss der Schraubenversetzungen für W ( $T_c = 800$  K) größer ist als für Mo ( $T_c = 480$  K) und Nb ( $T_c = 350$  K).

## 10.2 Spannungs-Dehnungsverhalten von krz Mikro- und Nanosäulen

Das Spannungs-Dehnungsverhalten wird in Kap. 4 für [001] und [235] orientierten Mo-Säulen, in Kap. 5 für [001] orientierte und in Kap. 7 für [235] orientierte W- und Nb-Säulen gezeigt. Alle getesteten Materialien weisen ein vom Säulendurchmesser abhängiges Verformungsverhalten auf: Bei Säulen mit Durchmesser von etwa 2 bis 6  $\mu\text{m}$  verläuft die Verformung kontinuierlich, wie bei einem entsprechenden Massivmaterial. Für Säulen mit Durchmessern unter 2  $\mu\text{m}$  tritt eine deutliche Änderung im Spannungs-Dehnungsverhalten auf. In diesem Größenbereich erfolgt die plastische Verformung sprunghaft in mehreren Einzelschritten, die durch Bereiche elastischer Verformung voneinander getrennt sind. Zudem wird beobachtet, dass die Kaltverfestigung speziell im Bereich unterhalb von 2  $\mu\text{m}$  mit abnehmendem Säulendurchmesser zunimmt und dass die Form der Spannungs-Dehnungskurven nicht von der Probenorientierung abhängig ist. Damit zeigen die getesteten krz Säulen die gleichen charakteristischen Merkmale, wie sie zuvor für lastkontrollierte Mikrodruckversuche an kfz Säulen gefunden wurden. Anders als für krz Massivmaterialien hat die kritische Temperatur bzw. die Mobilität der Schraubenversetzungen keinen Einfluss auf die Form der gemessenen Spannungs-Dehnungskurven. Folglich kann davon ausgegangen werden, dass sich die Versetzungsprozesse krz Metalle in kleinen Dimensionen von denen im Massivmaterial unterscheiden. In krz Massivmaterialien wird die Verformung durch die thermisch aktivierte Bewegung der Schraubenversetzungen bestimmt. Diese führt im Massivmaterial zu einer starken Abhängigkeit des Verformungsverhaltens von  $T_c$ . In kleinen Dimensionen können jedoch aufgrund von Oberflächeneffekten [144] oder einem Mangel an mobilen Versetzungen [125, 127] andere Versetzungsprozesse an Bedeutung erlangen, die somit das mechanische Verhalten bestimmen.



## 10.3 Verformungsmorphologie

Nach der mechanischen Belastung wurde die Verformungsmorphologie der Säulen in einem Rasterelektronenmikroskop untersucht. Die Ergebnisse für die Mo Säulen sind in Kap. 4, die der W und Nb Säulen in Kap. 5 und 7 dargestellt. Unabhängig vom Säulendurchmesser werden an den Seitenflächen der verformten W, Mo und Nb Säulen Gleitstufen beobachtet. Dies bestätigt, dass die plastische Verformung der Säulen durch Versetzungsbewegung erfolgt. Bei den [001] orientierten Säulen deuten die Gleitstufen drauf hin, dass die Versetzungsbewegung auf mehreren Gleitsystemen stattfindet, wohingegen die Gleitstufen der [235] orientierten Säulen die Aktivierung eines einzelnen Gleitsystems anzeigen. Obwohl die jeweiligen Orientierungen bei den verschiedenen Materialien an Massivproben zu sehr ähnlichen Verformungsmorphologien führen, unterscheiden sich die Gleitstufen an den W, Mo und Nb Säulen erheblich. Diese Unterschiede treten jedoch nur an Säulen mit Durchmessern größer als 1 – 2  $\mu\text{m}$  auf und sind am deutlichsten zwischen Nb und W zu erkennen. An den W und Mo Säulen werden wellenförmige Gleitstufen beobachtet, die charakteristisch für die Verformung krz Massivmaterialien sind und einen Hinweis für das häufige Quergleiten der Schraubenversetzungen darstellen. Im Gegensatz dazu, sind die Gleitstufen der Nb Säulen klar definiert und besitzen keinen wellenförmigen Charakter, was vermuten lässt, dass die Tendenz für das Quergleiten der Schraubenversetzungen in den Nb Säulen geringer ist als im Massivmaterial. Vermutlich führt die relativ niedrige kritische Temperatur von Nb dazu, dass in kleinen Dimensionen die plastische Verformung zum großen Teil durch die Bewegung von Stufenversetzungen erfolgt und damit die Versetzungsbewegung auf klar definierten Ebenen stattfindet. Für Säulen mit kleineren Durchmessern werden die Unterschiede in der Verformungsmorphologie nicht beobachtet. Es wird angenommen, dass in diesem Größenbereich die Bewegung der Schraubenversetzungen einen geringeren Einfluss auf die mechanischen Eigenschaften der Säulen hat und daher auch nicht zu einer materialabhängigen Verformungsmorphologie führen kann. Der abnehmende Einfluss der Schraubenversetzungsbewegung wird auch durch den Vergleich der normalisierten Fließspannungen krz und kfz Säulen (siehe Kap. 4 und 7) sowie durch die Berechnung der jeweiligen Aktivierungsvolumen (siehe Kap. 4 und 8) bestätigt.

## 10.4 Größen- und Temperaturabhängigkeit der Fließspannung

In den Kap. 4, 5 und 7 wird die Größenabhängigkeit der Fließspannung der [001] und [235] orientierten W, Mo und Nb Säulen untersucht. Die Temperaturabhängigkeit der Fließspannung ist Gegenstand der Kap. 5 und 7. Im untersuchten Größenbereich von 200 nm bis 6  $\mu\text{m}$  zeigen die getesteten Materialien für beide Orientierungen eine deutliche Zunahme der Fließspannung mit abnehmendem Säulendurchmesser. Das Skalierungsverhalten der Fließspannung kann wie für kfz Metalle mittels eines Exponentialgesetzes der Form  $\sigma_y \propto d^n$  beschrieben werden. Der Exponent  $n$  ist für die W Säulen unabhängig von der Probenorientierung und besitzt einen Wert von 0,16. Bei den Mo Säulen führen die verschiedenen Orientierungen zu Exponenten von 0,22 und 0,36, wobei die stärkere Größenabhängigkeit für die [235] Orientierung beobachtet wird. Für die Nb Säulen werden Exponenten von 0,42 bzw. 0,45 für die [001] bzw. [235] Orientierung erhalten. Im Vergleich zu kfz Metallen, für die unabhängig vom getesteten Material ein Exponent von 0.6 gefunden wurde, ist die Größenabhängigkeit krz Metalle damit deutlich schwächer ausgeprägt. Ein Vergleich der für die unterschiedlichen Materialien gemessenen Exponenten mit der jeweiligen kritischen Temperatur zeigt, dass die Größenabhängigkeit der Fließspannung mit einem ansteigenden Verhältnis aus  $T_{\text{test}}/T_c$  zunimmt und dass für  $T_{\text{test}}/T_c = 1$  ein Skalierungsverhalten ähnlich dem der kfz Metalle erwartet werden kann. Die Abhängigkeit des Größeneffekts von  $T_{\text{test}}/T_c$  deutet darauf hin, dass das unterschiedliche Verhalten krz und kfz Säulen vermutlich durch die unterschiedlichen Mobilitäten der Schraubenversetzungen verursacht wird. Bei einer ausreichenden thermischen Aktivierung wird der Effekt der Schraubenversetzungen vernachlässigbar. Dies führt für  $T_{\text{test}}/T_c = 1$  zu einem identischen Skalierungsverhalten der Fließspannung für krz und kfz Metalle. Folglich kann angenommen werden, dass der Größeneffekt in krz und kfz Metallen durch ähnliche Versetzungsprozesse verursacht wird, wenn Schrauben- und Stufenversetzungen identische Mobilitäten besitzen. Für  $T_{\text{test}}/T_c < 1$  beeinflusst jedoch die Kinetik der Schraubenversetzungen diese Prozesse und führt somit zu einer geringeren Größenabhängigkeit für die krz Metalle.

Neben dem Größeneffekt unterschieden sich krz und kfz Säulen auch in ihren, mit dem Schubmodul und dem Burgers-Vektor, normalisierten Fließspannungen. Größere Fließspannungen werden an krz Säulen beobachtet, wobei der relative Unterschied zwischen kfz und krz mit der kritischen Temperatur des Materials und mit ansteigendem Säulendurchmesser zunimmt. Für Säulen mit Durchmessern von ungefähr 200 nm werden für krz und kfz Metalle vergleichbare Spannungen gemessen. Dies zeigt, dass die Mobilität der

Schraubenversetzungen bei großen Durchmessern einen signifikanten Einfluss auf die Fließspannung der krz Säulen hat. Mit abnehmendem Säulendurchmesser scheint dieser Effekt jedoch an Bedeutung zu verlieren, was zu den vergleichbaren Fließspannungen für krz und kfz Säulen führen könnte.

Zwei Modelle werden vorgeschlagen um die beschriebenen Abhängigkeiten zu erklären. Beide basieren auf der Annahme, dass, bei ausreichender thermischer Aktivierung der Schraubenversetzungen, der Größeneffekt in krz und kfz Metallen durch die gleichen Versetzungsprozesse verursacht wird. Daher geht das erste Modell davon aus, dass es bei krz Metallen, aufgrund der geringen Mobilität der Schraubenversetzungen, zu einem kinetischen Aufstau von Versetzungen vor Versetzungsquellen kommt. Dieser kann eine Rückspannung auf die Quelle bewirken, die die Quellaktivierung im Vergleich zu kfz Metallen erschwert und damit zu höheren normalisierten Fließspannungen führt. Bei Säulen mit kleinen Durchmessern besteht wenig Platz für die Bildung eines kinetischen Aufstaus, weil die Versetzungen den Kristall an der freien Oberfläche verlassen können. Folglich ist die Fließspannung sehr kleiner Säulen durch die Aktivierungsspannung der Versetzungsquellen bestimmt. Diese ist primär durch die Quellgröße bestimmt, wodurch die ähnlichen normalisierten Spannungen kfz und krz Metalle für Säulendurchmesser von etwa 200 nm erklärt werden können. Das zweite Modell geht von einer vereinfachten Bildung von Kinken an der Oberfläche der Säulen aus. In krz Metallen erfolgt die Bewegung der Schraubenversetzungen durch die thermisch aktivierte Bildung und anschließende Wanderung von Kinkpaaren. Bei Schraubenversetzungen die an Oberflächen enden unterstützen Bildkräfte die Bildung von Kinken [144]. Mit zunehmendem Oberflächen- zu Volumenverhältnis gewinnt dieser Mechanismus an Bedeutung und führt somit zu einer ansteigenden Mobilität der Schraubenversetzungen mit abnehmendem Säulendurchmesser. Bei kleinen Durchmessern ist die thermische Komponente der Fließspannung damit vernachlässigbar und folglich bestimmt, wie im ersten Modell, die Quellaktivierung die Fließspannung.

## 10.5 Einfluss der Probenorientierung

Arbeiten von Greer et al. [126] und Brinckmann et al. [143] deuten darauf hin, dass die mechanischen Eigenschaften krz Säulen durch konventionelle Versetzungswechselwirkungen bestimmt werden könnten. Die Abhängigkeit dieser Wechselwirkungen von der Anzahl an aktivierten Gleitebenen sollte für krz Säulen zu einer starken Orientierungsabhängigkeit des

mechanischen Verhaltens führen, welche für kfz Säulen nicht beobachtet wird. Der Einfluss der Probenorientierung auf das mechanische Verhalten kfz Säulen wird in Kap 4 an Mo Säulen und in Kap. 7 an Nb und W untersucht. Dafür wurden jeweils Säulen mit einer [001] und einer [235] Orientierung verformt und die erhaltenen Ergebnisse verglichen. Die Untersuchung der Gleitstufen an den verformten Säulen zeigt (vgl. 10.3), dass sich die [001] orientierten Säulen mittels Mehrfachgleitung und [235] orientierten Säulen durch Einfachgleitung verformen. Trotz der unterschiedlichen Anzahl an aktivierten Gleitsystemen kann kein signifikanter Unterschied im Spannungs-Dehnungsverhalten der [001] und [235] orientierten Säulen festgestellt werden. Unabhängig vom getesteten Material wird für beide Orientierungen ein Anstieg der Fließspannung mit abnehmendem Säulendurchmesser beobachtet. Dabei ergeben sich nahezu identische Abhängigkeiten der Fließspannung vom Säulendurchmesser für die [001] und die [235] Orientierung im Fall von W und Nb. Bei den Mo Säulen hingegen unterscheiden sich die für die verschiedenen Orientierungen bestimmten Größenabhängigkeiten, wobei ein stärkerer Größeneffekt für die Einfachgleit-Orientierung gefunden wird. Weiterhin sind für die W und Nb Säulen die Absolutwerte der Fließspannung unabhängig von der Probenorientierung, während bei den Mo Säulen die Einfachgleit-Orientierung zu höheren Fließspannungen führt. Die Übereinstimmung der Fließspannungen sowie die identischen Größenabhängigkeiten für [001] und [235] orientierte W bzw. Nb Säulen zeigen, dass zumindest für diese kfz Metalle der Größeneffekt nicht von der Anzahl an aktivierten Gleitebenen abhängig ist und somit nicht durch Versetzungswechselwirkungen verursacht werden kann. Die größeren Fließspannungen der [235] gegenüber denen der [001] orientierten Mo Säulen lässt vermuten, dass auch für Mo Versetzungswechselwirkungen von geringer Bedeutung sind, denn diese sollten aufgrund der größeren Zahl an möglichen Gleitsystemen zu einer größeren Festigkeit der [001] orientierten Säulen führen. Damit widersprechen die gefundenen Ergebnisse den Arbeiten von Greer et al. [126] und Brinckmann et al. [143] und zeigen, dass die Probenorientierung keinen wesentlichen Einfluss auf das mechanische Verhalten der kfz Säulen hat. Es kann davon ausgegangen werden, dass für Probendimensionen im Bereich von wenigen Mikrometern oder Nanometern andere Versetzungsprozesse, die nicht primär von der Probenorientierung abhängig sind, das mechanische Verhalten bestimmen.

## 10.6 Dehnratenabhängigkeit und Aktivierungsvolumen

Eine charakteristische Parameter für Metalle, der Aufschluss über die thermisch aktivierte Bewegung der Schraubenversetzungen geben kann, ist die Dehnratenabhängigkeit der Fließspannung. In Kap. 5 und 7 wird ein Zusammenhang zwischen der Größenabhängigkeit der Fließspannung und der Mobilität der Schraubenversetzungen aufgezeigt. Weiterhin wird vermutet, dass der Einfluss der Schraubenversetzungen mit dem Säulendurchmesser abnimmt. Um den Beitrag der Schraubenversetzungen zum mechanischen Verhalten der getesteten Säulen zu quantifizieren, wird in Kap 4 und 8 die Dehnratenabhängigkeit der Fließspannung untersucht. Dazu wurden für jedes Material jeweils mehrere Säulen mit Durchmessern im Bereich von 300 nm bis 3  $\mu\text{m}$  hergestellt und mit unterschiedlichen Belastungsraten im Bereich von 1  $\mu\text{N/s}$  bis 500  $\mu\text{N/s}$  verformt. Daraus wurden die Dehnratenabhängigkeit sowie die zugehörigen Aktivierungsvolumen bestimmt. Wie bei den entsprechenden Massivmaterialien wird ein deutlicher Anstieg der Fließspannung mit zunehmender Dehnraten beobachtet, was bestätigt, dass die Verformung der krz Säulen eine zeitabhängige Komponente besitzt. Die aus der Dehnratenempfindlichkeit berechneten Aktivierungsvolumen mit Werten zwischen  $1b^3 - 9b^3$  deuten darauf hin, dass die thermisch aktivierte Kinkpaarbildung der Schraubenversetzungen für diese Abhängigkeit verantwortlich ist. Weiterhin wird festgestellt, dass das Aktivierungsvolumen mit dem Säulendurchmesser abnimmt. Demzufolge wird in kleinen Dimensionen weniger thermische Energie für die Bewegung der Schraubenversetzungen benötigt. Eine mögliche Ursache hierfür, ist die Abhängigkeit der Fließspannung vom Säulendurchmesser. Die hohen Spannungen in kleinen Säulen können dazu führen, dass die Schraubenversetzungen weniger thermische Energie für die Überwindung des Peierls-Potential benötigen. Berechnungen, basierend auf der Kinkpaar-Theorie von Seeger, zeigen jedoch, dass die Größenabhängigkeit der Fließspannung nicht die alleinige Ursache für die Größenabhängigkeit des Aktivierungsvolumens sein kann. Demnach muss ein anderer Mechanismus zu einer geringeren Aktivierungsenergie der Schraubenversetzungsbewegung in kleinen Dimensionen führen. Möglich ist, dass die Bildung von Kinken mit ansteigendem Oberflächen- zu Volumenverhältnis bevorzugt an der Oberfläche erfolgt und damit die für die Schraubenversetzungsbewegung notwendige thermische Energie reduziert wird.

## 10.7 Einfluss der Vorverformung

*In situ* TEM Experimente an kfz Säulen haben gezeigt, dass Versetzungen den Kristall verlassen, unmittelbar nachdem sie von Versetzungsquellen emittiert werden [125]. Bei krz Säulen könnte die geringe Mobilität der Schraubenversetzungen zu einer längeren Verweilzeit der Versetzungen im Kristall führen [126]. Dadurch steigt die Wahrscheinlichkeit für Versetzungswechselwirkungen. Um deren Beitrag zum mechanischen Verhalten krz Säulen zu untersuchen, beschäftigt sich das Kap 6 mit Druckversuchen an bereits verformten Mo Säulen, wobei das Verhalten während der ersten Belastung Gegenstand von Kap. 4 ist. Nach der ersten Belastung wurden die verformten Säulen mit dem FIB nachpräpariert und anschließend ein zweites Mal belastet. Es wird festgestellt, dass die Vorverformung keinen signifikanten Einfluss auf die Verformungsmorphologie und die Form der Spannungs-Dehnungskurven hat. Gleitstufen treten in der ersten und zweiten Belastung meist an ähnlichen Stellen entlang der Säulen auf und die Spannungs-Dehnungskurven zeigen jeweils die charakteristischen Merkmale lastkontrollierter Druckversuche. Die Fließspannung und die Kaltverfestigungsrate der vorverformten Säulen nehmen wie im Ausgangszustand mit abnehmendem Säulendurchmesser zu. Obwohl die Proben während der ersten Belastung eine ausgeprägte Kaltverfestigung aufweisen, sind die Absolutwerte für die Fließspannung der vorverformten Säulen unabhängig vom Ausmaß der Vorverformung. Weiterhin wird beobachtet, dass die Fließspannung der vorverformten Säulen deutlich kleiner ist als die bei der ersten Belastung gemessene Maximalspannung. Demzufolge hat die aus der ersten Belastung resultierende Kaltverfestigung keinen Einfluss auf die Fließspannung der vorverformten Säulen. Im Gegensatz dazu zeigen Mo Säulen, die während eines Druckversuches entlastet wurden, vor und nach der Entlastung vergleichbare Spannungen. Dies verdeutlicht, dass die Verfestigung während der ersten Belastung die Fließspannung der Probe in der zweiten Belastung nur dann beeinflusst, wenn die Säule zwischen der ersten und zweiten Belastung nicht mit dem FIB bearbeitet wurde. Folgende Schlüsse können aus diesen Beobachtungen gezogen werden: Zum einen, kontrollieren die durch das FIB verursachten Defekte die mechanischen Eigenschaften der vorverformten Säulen und zum anderen kann die Kaltverfestigung nicht durch die Speicherung und Wechselwirkung von Versetzungen verursacht werden, da dies zu einer relevanten Festigkeitssteigerung der vorverformten Proben führen sollte. Demnach kann davon ausgegangen werden, dass die Aktivierung von Versetzungsquellen entscheidend für die Verformung der Mo Säulen ist. Zunächst aktive Quellen können im Verlauf der Verformung versiegen, was zur Aktivierung ungünstigerer Quellen bei höheren Spannungen und damit zu einer Verfestigung führen kann [141]. Wird

eine verfestigte Probe mit dem FIB bestrahlt, dann werden zusätzliche Defekte und damit potentielle Versetzungsquellen in das Material eingebracht. Die neuen Quellen besitzen möglicherweise niedrigere Aktivierungsspannungen als die in der Probe ursprünglich vorhandenen Quellen. Damit wird die Fließspannung der vorverformten Säulen durch die Aktivierung der neuen Quellen bestimmt und die Verfestigung während der ersten Belastung wird somit unbedeutend für die zweite Belastung der Säulen.

## 10.8 Zusammenfassung

Mikrodruckversuche wurden an krz, [001] und [235] orientierten W, Mo und Nb Säulen mit Durchmessern von 200 nm bis 6  $\mu\text{m}$  durchgeführt. Die wichtigsten Beobachtungen sind:

- Die Spannungs-Dehnungskurven der krz Säulen zeigen die charakteristischen Merkmale lastkontrollierter Mikrodruckversuche. Die Probenorientierung und die kritische Temperatur des Metalls haben einen geringen Einfluss auf die Kaltverfestigung.
- Die Verformungsmorphologie ist vom Säulendurchmesser und der kritischen Temperatur abhängig. Bei einer hohen kritischen Temperatur führt das Quergleiten der Schraubenversetzungen zu wellenförmigen Gleitstufen. In Säulen mit kleinen Durchmessern und bei Metallen mit einer niedrigen kritischen Temperatur nimmt die Tendenz zum Quergleiten ab.
- Für beide Orientierungen zeigen die W, Mo und Nb Säulen eine vom Durchmesser abhängige Fließspannung. Die Größenabhängigkeit der Fließspannung skaliert mit  $T_{\text{test}}/T_c$  und ist für  $T_{\text{test}} < T_c$  deutlich schwächer als für kfz Metalle.
- Normierte Fließspannungen von kfz und krz Säulen konvergieren bei Säulendurchmessern von etwa 200 nm. Bei größeren Durchmessern besitzen krz Säulen größere Fließspannungen als kfz Säulen, wobei der relative Unterschied umso größer ist je größer die kritische Temperatur des krz Metalls ist.
- Die Fließspannung der W, Mo und Nb Säulen ist dehnratenabhängig. Wie im Massivmaterial steigt die Fließspannung mit zunehmender Dehnrates an.
- Aus der Dehnratenempfindlichkeit berechnete Aktivierungsvolumen liegen im Bereich von  $1b^3 - 9b^3$ . Unabhängig vom Material nehmen die berechneten Aktivierungsvolumen mit dem Säulendurchmesser ab.

- Eine Vorverformung um mehrere Prozent hat keinen Einfluss auf die mechanischen Eigenschaften krz Mo Säulen, wenn diese zuvor mit einem FIB bearbeitet wurden.

Das mechanische Verhalten der krz Säulen lässt sich durch die Aktivierung von Versetzungsquellen und die besondere Rolle der Schraubenversetzungen in krz Metallen erklären. Die sukzessive Aktivierung und Versiegung von Versetzungsquellen führt zu den für Mikrodruckversuche charakteristischen Spannungs-Dehnungskurven. Die Größenabhängigkeit der Fließspannungen ist dabei durch die Aktivierungsspannung der Quellen und die Mobilität der Schraubenversetzungen bestimmt. Bei großen Durchmessern erschwert die geringe Beweglichkeit der Schraubenversetzungen die Quellaktivierung. Dies erklärt die hohen Fließspannungen im Vergleich zu kfz Metallen. Die Konvergenz der Fließspannungen krz und kfz Metalle bei kleinen Durchmessern wird durch einen mit dem Säulendurchmesser abnehmenden Einfluss der Schraubenversetzungen erklärt. Mit zunehmendem Oberflächen- zu Volumenverhältnis, d.h. mit abnehmendem Säulendurchmesser, kann die Kinkbildung der Schraubenversetzungen bevorzugt an der Oberfläche erfolgen, wodurch die für die Schraubenversetzungsbewegung notwendige Spannung reduziert wird. Der abnehmende Einfluss der Schraubenversetzungen zeigt sich auch in der Verformungsmorphologie und in den berechneten Aktivierungsvolumen, die ebenfalls mit dem Säulendurchmesser abnehmen. Bei einer ausreichenden thermischen Aktivierung verlieren die Schraubenversetzungen auch bei großen Durchmessern an Bedeutung. Dies erklärt, dass für krz Metalle mit einer niedrigen kritischen Temperatur, vergleichbare Fließspannungen und eine ähnliche Größenabhängigkeit wie für kfz Metalle beobachtet werden.



# 11 References

- [1] E. Arzt, *Acta Mater.* 46/16 (1998) 5611.
- [2] G. Dehm, T. Wagner, T.J. Balk, E. Arzt, B.J. Inkson, *J. Mater. Sci. Tech.* 18/2 (2002) 113.
- [3] G. Dehm, T.J. Balk, H. Edongue, E. Arzt, *Microelectron. Eng.* 70 /2-4 (2003) 412.
- [4] P.A. Gruber, J. Bohm, F. Onuseit, A. Wanner, R. Spolenak, E. Arzt, *Acta Mater.* 56/10 (2008) 2318.
- [5] P.A. Gruber, C. Solenthaler, E. Arzt, R. Spolenak, *Acta Mater.* 56/8 (2008) 1876.
- [6] Y. Xiang, X. Chen, J.J. Vlassak, *J. Mater. Res.* 20/9 (2005) 2360.
- [7] Y. Xiang, T.Y. Tsui, J.J. Vlassak, *J. Mater. Res.* 21/6 (2006) 1607.
- [8] M.A. Haque, M.T.A. Saif, *Experimental Mech.* 43/3 (2003) 248.
- [9] L.B. Freund, *J. Appl. Mech.* 54/3 (1987) 553.
- [10] W.D. Nix, *Metall. Trans. A* 20/11 (1989) 2217.
- [11] P. Chaudhari, *Philos. Mag.* 39/4 (1979) 507.
- [12] C.V. Thompson, *J. Mater. Res.* 8/2 (1993) 237.
- [13] M.S. De Guzman, G. Neubauer, P. Flinn, W.D. Nix, *Mater. Res. Symp. Proc.* 308 (1993) 613.
- [14] M. Atkinson, *J. Mater. Res.* 10/11 (1995) 2908.
- [15] S. Suresh, T.G. Nieh, B.W. Choi, *Scripta Mater.* 41/9 (1999) 951.
- [16] W.D. Nix, H.J. Gao, *J. Mech. Phys. Solids* 46/3 (1998) 411.
- [17] W. Zielinski, H. Huang, S. Venkataraman, W.W. Gerberich, *Philos. Mag.* 72/5 (1995) 1221.
- [18] W.W. Gerberich, J.C. Nelson, E.T. Lilleodden, P. Anderson, J.T. Wroblek, *Acta Mater.* 44/9 (1996) 3585.
- [19] M.D. Uchic, D.M. Dimiduk, J.N. Florando, W.D. Nix, *Science* 305/5686 (2004) 986.
- [20] M.D. Uchic, D.M. Dimiduk, *Mater. Sci. Eng. A* 400 (2005) 268.
- [21] J.R. Greer, W.C. Oliver, W.D. Nix, *Acta Mater.* 53/6 (2005) 1821.
- [22] D.M. Dimiduk, M.D. Uchic, T.A. Parthasarathy, *Acta Mater.* 53/15 (2005) 4065.

## References

---

- [23] M.D. Uchic, D.M. Dimiduk, R. Wheeler, P.A. Shade, H.L. Fraser, *Scripta Mater.* 54/5 (2006) 759.
- [24] C.A. Volkert, E.T. Lilleodden, *Philos. Mag.* 86/33-35 (2006) 5567.
- [25] D. Kiener, C. Motz, T. Schoberl, M. Jenko, G. Dehm, *Adv. Eng. Mater.* 8/11 (2006) 1119.
- [26] C.P. Frick, B.G. Clark, S. Orso, A.S. Schneider, E. Arzt, *Mater. Sci. Eng. A* 489 (2008) 319.
- [27] K.S. Ng, A.H.W. Ngan, *Acta Mater.* 56/8 (2008) 1712.
- [28] D. Kiener, C. Motz, G. Dehm, *Mater. Sci. Eng. A* 505/1-2 (2009) 79.
- [29] M.D. Uchic, P.A. Shade, D.M. Dimiduk, *Annu. Rev. Mater. Res.* 39/1 (2009) 361.
- [30] J.W. Christian, *Met. Trans. A* 14/7 (1983) 1237.
- [31] B. Sestak, A. Seeger, *Z. Metallkd.* 69/4 (1978) 195.
- [32] B. Sestak, A. Seeger, *Z. Metallkd.* 69/6 (1978) 355.
- [33] B. Sestak, A. Seeger, *Z. Metallkd.* 69/7 (1978) 425.
- [34] J.M. Burgers, *Proc. Koninkl. Ned. Akad. Wet.* 42/1/5 (1939) 293.
- [35] J.M. Burgers, *Proc. Koninkl. Ned. Akad. Wet.* 42/1/5 (1939) 378.
- [36] K.M. Ralls, T.H. Courtney, J. Wulff, *An Introduction to Materials Science and Engineering*, John Wiley & Sons, New York, 1976.
- [37] H. Gough, *Proc. Roy. Soc. Lond. A* 118/780 (1928) 498.
- [38] W. Fahrenhorst, E. Schmid, *Z. Phys.* 78 (1932) 383.
- [39] D.K. Bowen, J.W. Christian, G. Taylor, *Can. J. Phys.* 45/2P3 (1967) 903.
- [40] G. Taylor, J.W. Christian, *Philos. Mag.* 15/137 (1967) 873.
- [41] A. Seeger, *Z. Metallkd.* 72/6 (1981) 369.
- [42] A. Seeger, *Z. Metallkd.* 93/8 (2002) 760.
- [43] E. Schmid, in: *Proceedings of the International Congress on Applied Mechanics*, Delft, 1924, p. 342.
- [44] T.H. Courtney, *Mechanical Behavior of Materials*, McGraw-Hill, New York, 1990.
- [45] D. Hull, D.J. Bacon, *Introduction to Dislocations*, Pergamon Press, Oxford, 2001.

- 
- [46] G. Taylor, *Prog. Mater. Sci.* 36 (1992) 29.
- [47] A.S. Argon, *Strengthening Mechanisms in Crystal Plasticity*, Oxford University Press, Oxford, 2008.
- [48] S. Nemat-Nasser, *Plasticity: A Treatise on Finite Deformation of Heterogeneous Inelastic Materials*, Cambridge University Press, Cambridge, 2004.
- [49] R.J. Asaro, S. Suresh, *Acta Mater.* 53 (2005) 3369.
- [50] P. Rodriguez, R.W. Armstraong, *Bull. Mater. Sci.* 29/7 (2006) 717.
- [51] M. Li, T.S. Byun, L.L. Snead, S.J. Zinkle, *J. Nucl. Mater.* 377 (2008) 409.
- [52] W. Pichl, *phys. stat. sol. (a)* 189/1 (2002) 5.
- [53] A. Seeger, *Mater. Sci. Eng. A* 370/1-2 (2004) 50.
- [54] R.L. Smialek, T.E. Mitchell, *Philos. Mag.* 22/180 (1970) 1105.
- [55] R. Lachenmann, H. Schultz, *Z. Metallkd.* 66/8 (1975) 443.
- [56] F. Ackermann, H. Mughrabi, A. Seeger, *Acta Metall.* 31/9 (1983) 1353.
- [57] M. Werner, *phys. stat. sol. (a)* 104/1 (1987) 63.
- [58] D. Brunner, J. Diehl, *phys. stat. sol. (a)* 104/1 (1987) 145.
- [59] D. Brunner, J. Diehl, *phys. stat. sol. (a)* 124/1 (1991) 155.
- [60] D. Brunner, J. Diehl, *phys. stat. sol. (a)* 125/1 (1991) 203.
- [61] D. Brunner, J. Diehl, *phys. stat. sol. (a)* 124/2 (1991) 455.
- [62] D. Brunner, J. Diehl, *Z. Metallk.* 83/12 (1992) 828.
- [63] L. Hollang, M. Hommel, A. Seeger, *phys. stat. sol. (a)* 160/2 (1997) 329.
- [64] D. Brunner, V. Glebovsky, *Mater. Lett.* 44 (2000) 144.
- [65] D. Brunner, V. Glebovsky, *Mater. Lett.* 42/5 (2000) 290.
- [66] L. Hollang, D. Brunner, A. Seeger, *Mater. Sci. Eng. A* 319 (2000) 233.
- [67] A. Seeger, U. Holzwarth, *Philos. Mag.* 86/25-26 (2006) 3861.
- [68] D. Veselý, *phys. stat. sol. (a)* 29 (1968) 675.
- [69] D. Veselý, *Philos. Mag.* 27/3 (1973) 607.
- [70] F. Louchet, L.P. Kubin, *Acta Metall.* 23/17 (1975) 17.

## References

---

- [71] F. Louchet, L.P. Kubin, *phys. stat. sol. (a)* 56/1 (1979) 169.
- [72] F. Louchet, L.P. Kubin, D. Veselý, *Philos. Mag.* 39/4 (1979) 433.
- [73] A. Luft, *phys. stat. sol.* 42/1 (1970) 429.
- [74] A. Luft, L. Kaun, *phys. stat. sol.* 37/2 (1970) 781.
- [75] M.S. Duesbery, V. Vitek, *Acta Mater.* 46/5 (1998) 1481.
- [76] V. Vitek, M. Mrovec, J.L. Bassani, *Mater. Sci. Eng. A* 365 (2002) 31.
- [77] V. Vitek, A. Mrovec, R. Groger, J.L. Bassani, V. Racherla, L. Yin, *Mater. Sci. Eng. A* 387 (2003) 138.
- [78] V. Vitek, *Philos. Mag.* 84/3-5 (2004) 415.
- [79] W. Cai, V.V. Bulatov, J.P. Chang, J. Li, S. Yip, in: F.R.N. Nabarro, J.P. Hirth (Eds.), *Dislocations in Solids*, North-Holland, 2004, p. 1.
- [80] D. Brunner, *Mater. Trans. JIM* 41/1 (2000) 152.
- [81] D. Brunner, J. Diehl, *phys. stat. sol. (a)* 160 (1997) 355.
- [82] A. Seeger, W. Wasserbäch, *phys. stat. sol. (a)* 189/1 (2002) 27.
- [83] A. Seeger, *Handbuch der Physik*, vol. VII/2, Springer Verlag, Berlin, 1958.
- [84] B. Sestak, *Czech. J. Phys. (b)* B 22/4 (1972) 270.
- [85] J. Diehl, *Z. Metallkd.* 47/5 (1956) 331.
- [86] J. Diehl, *Z. Metallkd.* 47/6 (1956) 411.
- [87] J. Diehl, H. Rebstock, *Z. Naturf.* 11/2 (1956) 169.
- [88] A. Seeger, J. Diehl, S. Mader, H. Rebstock, *Philos. Mag.* 2/15 (1957) 323.
- [89] A. Seeger, *The Mechanism of Glide and Work-Hardening in Face-Centered Cubic and Hexagonal Close Packed Metals*. In: *Dislocations and Mechanical Properties of Crystals*, John Wiley & Sons, New York, 1957.
- [90] B. Sestak, A. Seeger, *phys. stat. sol. (b)* 43/1 (1971) 433.
- [91] J.S. Stölken, A.G. Evans, *Acta Mater.* 46/14 (1998) 5109.
- [92] N.A. Fleck, G.M. Muller, M.F. Ashby, J.W. Hutchinson, *Acta Metall. Mater.* 42/2 (1994) 475.
- [93] N.A. Stelmashenko, M.G. Walls, L.M. Brown, Y.V. Milman, *Acta Metall. Mater.* 41/10 (1993) 2855.

- 
- [94] Q. Ma, D.R. Clarke, *J. Mater. Res.* 10/4 (1995) 853.
- [95] H. Gao, Y. Huang, W.D. Nix, J.W. Hutchinson, *J. Mech. Phys. Solids* 47/6 (1999) 1239.
- [96] Y. Huang, H. Gao, W.D. Nix, J.W. Hutchinson, *J. Mech. Phys. Solids* 48/1 (2000) 99.
- [97] E. Arzt, G. Dehm, P. Gumbsch, O. Kraft, D. Weiss, *Prog. Mater. Sci.* 46/3-4 (2001) 283.
- [98] T.J. Balk, G. Dehm, E. Arzt, *Acta Mater.* 51/15 (2003) 4471.
- [99] G. Dehm, C. Motz, C. Scheu, H. Clemens, P.H. Mayrhofer, C. Mitterer, *Adv. Eng. Mater.* 8/11 (2006) 1033.
- [100] R.M. Keller, S.P. Baker, E. Arzt, *Acta Mater.* 47/2 (1999) 415.
- [101] R. Venkatraman, J.C. Bravman, *J. Mater. Res.* 7/8 (1992) 2040.
- [102] E.O. Hall, *Proc. Phys. Soc. Lond.* 64/381 (1951) 747.
- [103] N.J. Petch, *J. Iron Steel* 174/1 (1953) 25.
- [104] M. Legros, G. Dehm, R.M. Keller-Flaig, E. Arzt, K.J. Hemker, S. Suresh, *Mater. Sci. Eng. A* 309 (2001) 463.
- [105] W.D. Nix, *Scripta Mater.* 39/4-5 (1998) 545.
- [106] P. Pant, K.W. Schwarz, S.P. Baker, *Acta Mater.* 51/11 (2003) 3243.
- [107] L. Nicola, E. Van der Giessen, A. Needleman, *Mater. Sci. Eng. A* 309 (2001) 274.
- [108] L. Nicola, E. Van der Giessen, A. Needleman, *J. Appl. Phys.* 93/10 (2003) 5920.
- [109] L. Nicola, E. Van der Giessen, A. Needleman, *Thin Solid Films* 479/1-2 (2005) 329.
- [110] B. von Blanckenhagen, P. Gumbsch, E. Arzt, *Model. Simul. Mater. Sci. Eng.* 9/3 (2001) 157.
- [111] B. von Blanckenhagen, P. Gumbsch, E. Arzt, *Philos. Mag. Lett.* 83/1 (2003) 1.
- [112] B. von Blanckenhagen, E. Arzt, P. Gumbsch, *Acta Mater.* 52/3 (2004) 773.
- [113] M. Legros, G. Dehm, T.J. Balk, *Mater. Res. Soc. Symp. Proc.* 875 (2005) 1.
- [114] T.F. Page, W.C. Oliver, C.J. McHargue, *J. Mater. Res.* 7/2 (1992) 450.
- [115] S.G. Corcoran, R.J. Colton, E.T. Lilleodden, W.W. Gerberich, *Phys. Rev. B* 55/24 (1997) 16057.
- [116] S.S. Brenner, *J. Appl. Phys.* 27/12 (1956) 1484.

- [117] S.S. Brenner, J. Appl. Phys. 28/9 (1957) 1023.
- [118] S.S. Brenner, Science 128/3324 (1958) 569.
- [119] H. Bei, S. Shim, E.P. George, M.K. Miller, E.G. Herbert, G.M. Pharr, Scripta Mater. 57 (2007) 397.
- [120] H. Bei, S. Shim, G.M. Pharr, E.P. George, Acta Mater. 56/17 (2008) 4762.
- [121] R. Dou, B. Derby, Scripta Mater. 61/5 (2009) 524.
- [122] E.M. Nadgorny, D.M. Dimiduk, M.D. Uchic, J. Mater. Res. 23/11 (2008) 2829.
- [123] M.D. Uchic, P.A. Shade, D.M. Dimiduk, JOM 61/3 (2009) 36.
- [124] D. Kiener, C. Motz, G. Dehm, R. Pippan, Int. J. Mater. Res. 100/8 (2009) 1074.
- [125] Z.W. Shan, R.K. Mishra, S.A.S. Asif, O.L. Warren, A.M. Minor, Nature Mater. 7/2 (2008) 115.
- [126] J.R. Greer, C.R. Weinberger, W. Cai, Mater. Sci. Eng. A 493/1-2 (2008) 21.
- [127] J.R. Greer, W.D. Nix, Phys. Rev. B 73/24 (2006).
- [128] J.R. Greer, Rev. Adv. Mater. Sci. 13/1 (2006) 59.
- [129] H. Tang, K.W. Schwarz, H.D. Espinosa, Acta Mater. 55/5 (2007) 1607.
- [130] V.S. Deshpande, A. Needleman, E. Van der Giessen, J. Mech. Phys. Solids 53/12 (2005) 2661.
- [131] D.S. Balint, V.S. Deshpande, A. Needleman, E. Van der Giessen, Modelling Simul. Mater. Sci. Eng. 14/3 (2006) 409.
- [132] D.M. Norfleet, D.M. Dimiduk, S.J. Polasik, M.D. Uchic, M.J. Mills, Acta Mater. 56/13 (2008) 2988.
- [133] S.I. Rao, D.M. Dimiduk, M. Tang, T.A. Parthasarathy, M.D. Uchic, C. Woodward, Philos. Mag. 87/30 (2007) 4777.
- [134] J.A. El-Awady, S.B. Biner, N.M. Ghoniem, J. Mech. Phys. Solids 56/5 (2008) 2019.
- [135] J.A. El-Awady, M. Wen, N.M. Ghoniem, J. Mech. Phys. Solids 57/1 (2009) 32.
- [136] H. Tang, K.W. Schwarz, H.D. Espinosa, Phys. Rev. Lett. 100/18 (2008).
- [137] T.A. Parthasarathy, S.I. Rao, D.M. Dimiduk, M.D. Uchic, D.R. Trinkle, Scripta Mater. 56/4 (2007) 313.
- [138] D.M. Dimiduk, C. Woodward, R. LeSar, M.D. Uchic, Science 312/5777 (2006) 1188.

- [139] D.M. Dimiduk, M.D. Uchic, S.I. Rao, C. Woodward, T.A. Parthasarathy, *Mod. Simul. Mater. Sci. Eng.* 15/2 (2007) 135.
- [140] K.S. Ng, A.H.W. Ngan, *Philos. Mag. Lett.* 87/12 (2007) 967.
- [141] S.I. Rao, D.M. Dimiduk, T.A. Parthasarathy, M.D. Uchic, M. Tang, C. Woodward, *Acta Mater.* 56/13 (2008) 3245.
- [142] J. Senger, D. Weygand, P. Gumbsch, O. Kraft, *Scripta Mater.* 58/7 (2008) 587.
- [143] S. Brinckmann, J.-Y. Kim, J.R. Greer, *Phy. Rev. Lett.* 100/155502 (2008) 155502.
- [144] C.R. Weinberger, W. Cai, *PNAS* 105/38 (2008) 14304.
- [145] M. Zaiser, J. Schwerdtfeger, A.S. Schneider, C.P. Frick, B.G. Clark, P.A. Gruber, E. Arzt, *Philos. Mag.* 88/30 (2008) 3861.
- [146] J.-Y. Kim, J.R. Greer, *Appl. Phys. Lett.* 93 (2008) 101916.
- [147] I.N. Sneddon, *Int. J. Eng. Sci.* 3 (1965) 47.
- [148] D. Kiener, C. Motz, M. Rester, M. Jenko, G. Dehm, *Mater. Sci. Eng. A* 459/1-2 (2007) 262.
- [149] S. Shim, H. Bei, M.K. Miller, G.M. Pharr, E.P. George, *Acta Mater.* 57/2 (2009) 503.
- [150] H. Zhang, B.E. Schuster, Q. Wei, K.T. Ramesh, *Scripta Mater.* 54/2 (2006) 181.
- [151] G. Richter, K. Hillerich, D.S. Gianola, R. Monig, O. Kraft, C.A. Volkert, *Nano Lett.* 9/8 (2009) 3048.
- [152] T. Suzuki, S. Takeuchi, H. Yoshinaga, *Dislocation Dynamics and Plasticity*, Springer-Verlag, Berlin, 1991.
- [153] M. Černý, J. Pokluda, *Mater. Sci. Eng. A* 483 (2008) 692.
- [154] H.J. Frost, M.F. Ashby, *Deformation-mechanism maps*, Pergamon Press Ltd, Oxford, 1982.
- [155] J.P. Hirth, J. Lothe, *Theory of Dislocations*, Wiley, New York, 1982.
- [156] M.D. Uchic, D.M. Dimiduk, H. Muhgrabi, *Unpublished Research* (2005).
- [157] K.S. Ng, A.H.W. Ngan, *Philos. Mag.* 88/5 (2008) 677.
- [158] R. Gröger, V. Vitek, *Philos. Mag. Lett.* 87/2 (2007) 113.
- [159] H. Matsui, H. Kimura, *Mater. Sci. Eng. A* 24/2 (1976) 247.
- [160] S. Takeuchi, K. Maeda, *Acta Metall.* 25/12 (1977) 1485.

## References

---

- [161] Q. Wei, S. Cheng, K.T. Ramesh, E. Ma, Mater. Sci. Eng. A 381 (2004) 71.
- [162] H. Conrad, High Strength Materials, Wiley, New York, 1965.
- [163] M. Tang, L.P. Kubin, G.R. Canova, Acta Mater. 46 (1998) 3221.
- [164] A.S. Schneider, B.G. Clark, C.P. Frick, P.A. Gruber, E. Arzt, Mater. Sci. Eng. A 508/1-2 (2009) 241.
- [165] D. Kaufmann, R. Mönig, C.A. Volkert, O. Kraft, Int. J. Plasticity (submitted).
- [166] J.Y. Kim, D.C. Jang, J.R. Greer, Scripta Mater. 61/3 (2009) 300.
- [167] W.D. Nix, J.R. Greer, G. Feng, E.T. Lilleodden, Thin Solid Films 515/6 (2007) 3152.
- [168] P.J. Guruprasad, A.A. Benzerga, Philos. Mag. 88/30-32 (2008).
- [169] P.J. Guruprasad, A.A. Benzerga, J. Mech. Phys. Solids 56/1 (2008) 132.
- [170] A.S. Schneider, D. Kaufmann, B.G. Clark, C.P. Frick, P.A. Gruber, R. Monig, O. Kraft, E. Arzt, Phys. Rev. Lett. 103/10 (2009) 105501.
- [171] G.I. Taylor, H. Quinney, Philos. Trans. Roy. Soc. Lond. 230 (1932) 323.
- [172] J.J. Gilman, Micromechanics of Flow in Solids, McGraw-Hill, New York, 1969.
- [173] A.A. Benzerga, N.F. Shaver, Scripta Mater. 54/11 (2006) 1937.
- [174] A.S. Schneider, B.G. Clark, C.P. Frick, P.A. Gruber, E. Arzt, (Unpublished Work).
- [175] G. Petzow, Metallographisches, keramographisches, plastographisches Ätzen, Borntraeger, Stuttgart, 1994.
- [176] R. Maaß, S. Van Petegem, D. Grolimund, H. Van Swygenhoven, D. Kiener, G. Dehm, Appl. Phys. Lett. 92/7 (2008).
- [177] A. Seeger, P. Schiller, Acta Metall. 10/APR (1962) 348.